MARIE-ANNE LAVOIE-PERRIER

SOFT BODY IMPACT MODELING AND DEVELOPMENT OF A SUITABLE MESHLESS APPROACH

Thèse présentée
à la Faculté des études supérieures de l'Université Laval
dans le cadre du programme de doctorat en génie mécanique
pour l'obtention du grade de Philosophiae Doctor (Ph.D.)

DÉPARTEMENT DE GÉNIE MÉCANIQUE
FACULTÉ DES SCIENCES ET DE GÉNIE
UNIVERSITÉ LAVAL
QUÉBEC

JUILLET 2008

Résumé

Cette thèse présente des travaux récents relatifs à la modélisation d'impact de projectiles mous et le développement d'une méthode numérique sans maillage. En premier lieu, la théorie rattachée aux impacts d'oiseaux ainsi que les méthodes numériques et résultats expérimentaux disponibles sont donnés afin d'établir des normes pour les simulations d'impact d'oiseaux.

Les connaissances générales concernant les impacts d'oiseaux sont ensuite améliorées par des tests récents qui utilisent un substitut pour l'oiseau. Une recette pour le substitut est donnée afin de servir de référence dans les procédures de certification pour les impacts d'oiseaux. Les résultats sont également fournis afin de valider les modèles numériques et promouvoir l'utilisation des outils numériques dans le design de structures aéronautiques ainsi que dans le processus de certification. Les détails du montage expérimental sont donnés ainsi qu'une analyse de la précision des résultats obtenus et quelques sources d'erreurs à éviter dans l'éventualité où d'autres tests auraient lieu.

Finalement, la méthode sans maillage *smoothed particles hydrodynamics* (SPH) est modifiée afin qu'un algorithme maison puisse traiter le problème d'impact d'oiseaux. Afin de rencontrer cet objectif, des améliorations sont apportées à la formulation mathématique afin de traiter les problèmes d'instabilités numériques rapportés dans la littérature. Ensuite, des lois de comportement et des équations d'état ont été ajoutées. L'algorithme résultant peut être utilisé pour plusieurs types de problèmes, ce qui rend la méthode SPH très attrayantes pour les simulations numériques avec grandes déformations.

Abstract

This thesis describes recent work with respect to the modeling of soft body impact and the development of a meshless approach. To begin with, the theory of the bird impact, as well as available numerical methods and experimental data are given so that guidelines for bird impact simulations are provided.

The general expertise in bird impact modeling is then improved by recent bird tests using a bird substitute. A recipe is given for the substitute in order to use it as a reference in further bird tests certification procedures. Results from the tests are given so that they can be used to validate numerical models and promote the use of numerical tools in aircraft design and certification process. The details of the experimental set-up are also provided with an analysis of the accuracy of the results obtained and some pitfalls that should be avoided in future bird tests.

Finally, the meshless smoothed particles hydrodynamics (SPH) method is modified so that an in-house algorithm can treat the bird impact problem. In order to achieve this, improvements are brought to the mathematical formulation in order to address different instability problems identified in the literature. Then material models and equations of states were added. The resulting algorithm is applicable to a variety of problems, making the SPH method more appealing for computer simulations with large deformations.

Forewords

First of all, I would like to thank Dr. Gakwaya for his support and guidance throughout the duration of my studies as well as Dr. Nejad Ensan who acted as my co-director. Their help and patience was invaluable and is much appreciated.

I would also like to thank the Consortium for Research and Innovation in Aerospace in Quebec (CRIAQ) for financial support of this project as well as Laval University, the National Research Council of Canada (NRC) and Defence and Research Development Canada (DRDC) for their close collaboration and the industrial partners who provided practical applications to the project. Special thanks are given to the technical team of DRDC and their involvement in the tests.

Finally, the first chapter of the thesis presented is the published article *Validation of Available Approaches for Numerical Bird Strike Modeling Tools*, which appears in the 2007 issues of International Review of Mechanical Engineering, volume 1, pages 380-389.

Table of Contents

List of Tables

List of Figures

General Introduction

The study of bird strike modeling and the development of a suitable meshless approach are part of CRIAQ project 3.1 entitled *Impact Modeling of Composite Aircraft Structures*. The purpose of the project is to improve the passengers' protection when an aircraft structure undergoes soft body impact, such as a bird, or high velocity debris impact while decreasing the time and costs involved in the certification process. This thesis presents the scientific contribution made in relation with task 4.1.2.b B*ird Strike Modeling Effects on Composite Structures for Vertical Take-off and Landing Aircraft*.

Early in the project, it became evident that in order to study the behavior of composite materials under soft body impact, it would be necessary to model that soft body accurately since the response of the target would be meaningless unless the projectile was properly modeled. Thus, the research project focuses on the study, understanding, and development of soft body impact modeling.

Hence, a review of numerical modeling methods used in bird impact simulations has been performed and the results obtained are compared with the available experimental data and theoretical understanding of the phenomenon. This review enables new researchers to compare different numerical methods and to assess the quality of their own numerical bird model. One of the conclusions of the review was that the experimental tests results used to validate the numerical birds were inadequate since the results did not compare well with the theoretical values. Moreover, it is logical that advances in technology observed during the last three decades should lead to more accurate results if similar tests were to be conducted nowadays. Thus, new tests were performed at a velocity of 95 m/s for a 1 kg gelatine bird. This led to the development of a recipe for the gelatine bird which met the physical requirements for a bird substitute. The new results were then used to evaluate the numerical models.

Another aspect which contributes to obtaining good results when simulating bird impact is the numerical approach used. Three numerical methods are typically used. They are the Lagrangian method, the arbitrary Lagrangian-Euler (ALE) method and the smoothed particles hydrodynamics (SPH) methods, which is the most recent one. The second part of

the thesis studies the mathematical formulation of the SPH method. The SPH method is rapidly approaching a mature stage, and some of its characteristics make it highly interesting for situations where large deformations and fragmentation are observed. Improvements are brought to a standard formulation programmed in FORTRAN language to address some of the downfall of the method reported in the literature. The resulting equations are now derived form the energy conservation principle. Moreover, subroutines such as material models and fluid-structure interaction algorithms have been added to increase the versatility of the program. This results in an algorithm that is more complete and stable than the formulation available in commercial finite elements software such as LS-DYNA.

The scientific contribution of the work presented is a thorough understanding of numerical methods and validation procedures used for bird impact modeling up to this day. The new experimental data provide additional insight regarding the mechanics of the bird impact and new avenues and data to validate numerical models. The new gelatine recipe provides a reference so that other research groups can use and improve so that standards can some day be established for the projectiles used in the certification process. Moreover, the progress made for the SPH formulation make it suitable for a wider range of applications, especially in fluid-structure interaction problems.

Thus, the thesis is divided into two parts. First, a review of the existing numerical tools used to represent a bird together with the results of new tests performed to validate the numerical results is given. Second, the improvement of one of those numerical methods, namely the SPH method, was studied. Each topic is discussed thoroughly in Parts A and B of the thesis and the first chapter of each part is a literature review under article format. The subsequent chapters discuss each topic further either through experiments or additional numerical developments.

PART A – Summary of Bird Impact Analysis and Tests

In order to be able to study the impact of a bird on a composite structure in a real life application, it is necessary to assess that a good numerical model is available for the bird. The most efficient way to analyse the bird model itself is to make it impact a simple structure, such as a rigid flat plate. This way of proceeding ensures that the unknown of the simulations relate to the bird only.

The literature provides much information as to how scientists have proceeded in the past to create their numerical bird models. It includes the numerical methods they used, and the theories and experimental results they relied on to validate their work. As better understanding of the phenomenon was gained, it became obvious that there was a lack of general agreement between researchers as to how a bird strike simulation should be set up. Hence, a literature review of the theory and experimental data was performed which led to a performance analysis of different numerical methods. The resulting work was published in an article entitled *Validation of Available Approaches for Numerical Bird Strike Modeling Tools* which appeared in the 2007, volume 1, no 4 issue of the International Review of Mechanical Engineering, pages 380 to 389. The abstract is given below, followed by the French translation.

> This paper investigates the bird strike phenomenon in order to validate available numerical models through experimental tests and simulation tools. It describes how to use the currently available test data while exerting caution as to their reliability. The information is then used to evaluate the performance of the different modeling options currently available. The evaluation is based on six criteria that assess the quality of the bird models and the efficiency of the numerical approaches. Therefore, a general guideline is established as to how to set up the analysis of a bird strike and how to evaluate the obtained numerical results.

> Keywords: Non-linear finite element analysis, impact simulation, bird modeling, ALE method, SPH method, validation, bird strike test.

> *Cet article analyse le phénomène d'impact d'oiseaux de façon à valider les modèles numériques disponibles à l'aide de résultats expérimentaux et d'outils numériques.*

Les résultats expérimentaux disponibles sont décrits, ainsi que quelques mises en garde quant à leur exactitude. L'information recueillie est ensuite utilisée afin d'analyser la performance des différentes méthodes numériques existantes. L'analyse est basée sur six critères qui évaluent la qualité du modèle d'oiseau et l'efficacité des méthodes numériques. Par conséquent, des barèmes sont établis afin de savoir comment créer une analyse d'impact d'oiseaux et comment évaluer les résultats obtenus.

Mots clefs : Analyse par éléments finis non-linéaire, simulation d'impact, modélisation d'oiseaux, méthode ALE, méthode SPH, validation, tests d'impact d'oiseaux

The article made it possible to demonstrate the need for new tests to be conducted. Thus, the partners of the project agreed to approve new bird tests. These were performed at the Defence and Research Development Canada laboratory facilities in Valcartier in the spring of 2007. Since the last available tests results were performed in 1977 [1], it can be expected that new technologies developed during the last three decades will be helpful in getting better results.

Chapter 2 describes how the tests were performed and the scientific contribution they have for bird tests in general. The first challenge encountered was to come up with a gelatine recipe that could serve as a bird substitute. Using gelatine instead of a real bird was necessary so that the geometry would be the same as the numerical model. Additionally, using a bird substitute makes it possible to use uniform projectiles in the certification process. The results from the tests are two fold. The pressure of the bird impacting on the rigid plate is measured, as has been done in the past and a video camera captured the deformation of the bird during the impact, which gives the opportunity to examine the transient deformation of the projectile. The difficulties encountered during the tests are explained and recommendations are made for research teams who would wish to perform similar tests in the future. The chapter also reviews the performances of the numerical birds modeled with the ALE and the SPH approaches by comparing their results against the experimental results.

1 Validation of Available Approaches for Numerical Bird Strike Modeling Tools

1.1 Introduction

Ever since man put airplanes in the air, they have had the most unfortunate tendency to prematurely come down for various reasons, some of them more life threatening than others. The fact that airspace has to be shared with birds is not alien to that. In fact, according to recent data [2], 59,000 bird strike events were reported between 1990 and 2004 representing an estimated 20% of the actual number of bird strikes. Therefore, because of the threat they pose, bird strike takes an important place in all aircraft certification process.

During the certification process, an aircraft must demonstrate its ability to land safely after being struck by a bird anywhere on the structure, at normal operating speeds [3]. Although substantial and costly damage may occur, the performance of the key components, including the wing and engines, must be demonstrated. Impacted components must maintain structural integrity during the large transient loading resulting from bird strike loads.

Past experience has been to demonstrate this compliance through full-scale tests. Because of the costs and time involved, there is a need to improve modeling capabilities and enable verification by numerical methods. This in turn will help to decrease the number of destructive testing required. To accurately predict the response of an aircraft structure under impact loading, it is essential to have an accurate bird model.

Bird strike modeling has remarkably evolved since its first attempts, where a pressure pulse was applied to a finite element model [4]. Nowadays, the bird strike event represents a complex problem that the Lagrangian [5,6,7,8,9,10,11,12], the arbitrary Lagrangian-Euler [7,8,9,13,14,15], and the smooth particle hydrodynamic [4,16,17,18,19,20,21] methods have successively attempted to solve with their own measure of success.

The fact that several approaches are used underlines the difficulties faced when trying to assess the quality of a model since there is few publicly available experimental data. Most authors studying bird strike have to be satisfied with using the results given by Wilbeck [1,22] to validate their numerical bird model [5,6,7,8,14,17,23,24]. On the other hand, when measurements are taken, it is that of a deformed aeronautical structure [8,9,13,17,18,20,21,25,26,27,28,]. The information is then used in reverse engineering to validate one specific simulation. It is difficult to create a numerical bird model suitable for all simulations from such specific data. McCarthy [4,20] does refer to more recent data, but those are not available to the public.

From a numerical point of view, very little has been done up to these days to compare the modeling methods and assess which one would be more suitable. Hörmann [27] and Castellitti [29] agree that the ALE method is better than the Lagrangian approach, but Hörmann does not use experimental data to validate his bird models. Goyal [24] compares the Lagrangian and SPH method in a parametric study of the contact and prefers the SPH method for the frontal impact of birds. None of those authors refer to the theory of the bird strike.

This paper aims at summarizing the steps involved in creating the bird model. It describes the theory of the bird strike and provides a sample of the available experimental data. Then a demonstration is given as to how to evaluate a bird model based on the following criteria including *i)* pressure profile at the center of impact, *ii)* mass loss, *iii)* impulse profile at the center of impact, *iv)* radial pressure distribution, *v)* shape of the sustained deformations, *vi)* and solution time. The three modeling methods mentioned earlier are presented along with a brief parametric study of the factors influencing the fluid-structure interaction. They are compared and evaluated with respect to the theoretical and experimental available information. Moreover, the experimental data which are often used as a reference are evaluated with respect to the theory, demonstrating that although useful, they should be referred to with care.

The rest of the paper is organized as follow: The next section covers the theory related to bird strike. The experimental behaviour of a bird under impact is recalled in Section 1.3 as presented by Wilbeck. The three available numerical bird models and the material

properties used are described in Section 1.4. The results obtained with the available models are presented and discussed according to the evaluation criteria in Section 1.5. The conclusions are drawn in the last section.

1.2 Theory of bird strike

A bird undergoing impact at high velocity behaves as a highly deformable projectile where the yield stress is much lower than the sustained stress. Accordingly, the impact can be qualified as a hydrodynamic impact. That, and the fact that the density of flesh is generally close to the density of water, makes it possible for a bird to be considered as a lump of water hitting a target. This is the main assumption leading to the understanding of the behaviour of a bird.

The bird strike event itself is divided into two stages: the initial shock and the steady flow. The pressure of the initial shock is called Hugoniot pressure and is given by equation (1.1); the pressure of the steady flow (stagnation pressure) is calculated according to Bernoulli and is given by equation (1.2):

$$\text{Hugoniot pressure:} \quad P_{sh} = \rho v_{sh} v_{im} \tag{1.1}$$

$$\text{Stagnation pressure:} \quad P_{stag} = \tfrac{1}{2} \rho v_{im}^2 \tag{1.2}$$

where: P_{sh} shock pressure

P_{stag} stagnation pressure

v_{sh} velocity of sound across the shock wave

v_{im} velocity of the impact

ρ density of the bird

Equation (1.2) gives the stagnation pressure for an incompressible fluid; however, if the fluid is compressible, its value will increase with respect to its porosity, z. Airoldi [10] gives a useful expression to calculate the modified stagnation pressure:

$$P_{stag\ z} = \frac{1}{1-z} P_{stag} \tag{1.3}$$

Analytically, those two pressures are important since the Hugoniot pressure gives the maximum possible value for the impact at its very beginning and the stagnation pressure gives the expected reading when the flow stabilizes. It is also important to realize that the pressure is independent of the size of the projectile since the mass is not a variable in the pressure equations. This implies that the pressure results are the same regardless of the projectile, provided they share the same impact velocity. Of course, the force and energy of a bigger projectile is proportionally larger and will cause more damage.

The values of the variables needed to calculate the stagnation pressure are easily available. On the other hand, the Hugoniot pressure depends on the impact velocity and the shock velocity, which itself also depends on the impact velocity. Moreover, the equation changes whether or not porosity is included, or if the fluid considered is water or a substitute. The equations (1.4) to (1.9), given below, apply to a projectile with an amount of air mixed in, also called porosity, since experience has shown that porosity has a non-negligible effect on the overall results and is closer to the behaviour of a bird upon impact [1].

$$\rho_1 v_{sh} = \rho_2 (v_{sh} - v_{im}) \tag{1.4}$$

$$P_1 - P_2 = \rho_1 v_{sh} v_{im} \tag{1.5}$$

$$\frac{\rho_1}{\rho_2} = (1-z)\left(\frac{P_2}{A}+1\right)^{-1/B} + z(1-q) \tag{1.6}$$

with $$A = \frac{\rho_1 c_o^2}{4k-1} \tag{1.7}$$

$$B = 4k - 1 \tag{1.8}$$

$$\frac{\rho_2}{\rho_1} = \frac{1}{1-q} \tag{1.9}$$

where: k experimental constant

c_o speed of sound in medium, i.e. water

$\rho_{1,2}$ density of the medium before and after the impact

$P_{1,2}$ pressure before and after the impact (P_1 is negligible)

$z(1\text{-}q)$ contribution of the air mixed in, negligible

q is a measure of compressibility

The solution for the shock velocity is found by isolating ρ_1/ρ_2, making (1.6) and (1.4) equal, and using (1.5) for the pressure P_2. Once the shock velocity is known, the Hugoniot pressure can be found from (1.1). Figure 1.1 shows the shock velocity and the shock pressure for impact velocities ranging from 0 to 300 m/s. The shock velocity and shock pressure are plotted for two different porosities in order to illustrate the influence of that parameter.

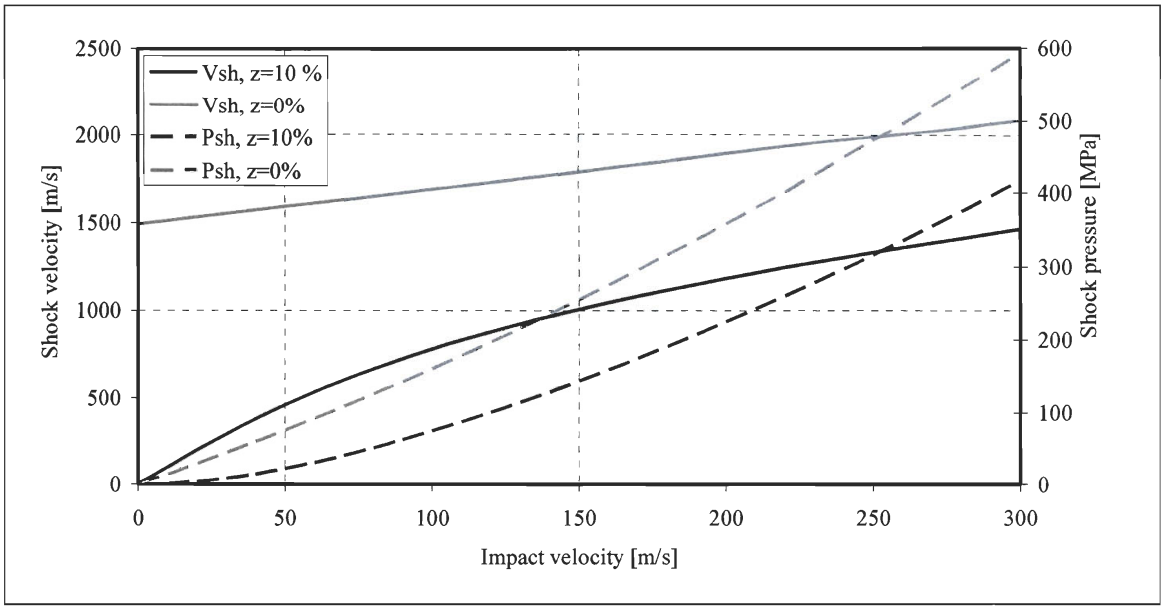

Figure 1.1 Theoretical results for shock velocity and shock pressure with different porosity

An additional useful information resulting from associating the bird to water is the equation of state (EOS) used to describe the pressure-density relationship in the bird medium. A few equations are available, and the one most commonly used for bird strikes is a polynomial of degree 3 [1] defined as follow:

$$P = C_0 + C_1\mu + C_2\mu^2 + C_3\mu^3 \qquad (1.10)$$

where μ is given by $\mu = \rho/\rho_o - 1$ and represents the change in density during the impact. This polynomial equation of state for the bird model corresponds to a hydrodynamic, isotropic, and non-viscous constitutive law.

The coefficients are given by expressions based on the initial density ρ_o, the speed of sound in water and an experimental constant k related to compressibility. The expressions are:

$$C_0 \quad \text{initial equilibrium pressure, negligible}$$

$$C_1 = \rho_o c_o^2$$

$$C_2 = (2k-1)C_1 \qquad (1.11)$$

$$C_3 = (k-1)(3k-1)C_1$$

Finally, when the fluid flow reaches a steady state, it is also possible to calculate the pressure distribution along the radius, where r is the radial position and R is the radius of the projectile.

$$P = P_{stag} \exp\left[-\tfrac{1}{2}\left(\tfrac{r}{R}\right)^2\right] \qquad (1.12)$$

Equation (1.12) is plotted in Figure 1.2 for different porosities and velocities. Note that the stagnation pressure used depends on whether or not the porosity is considered and that if the results were normalized, the pressure distribution would be the same regardless of the impact velocity or porosity (given the appropriate stagnation pressure is used for the cases with and without porosity).

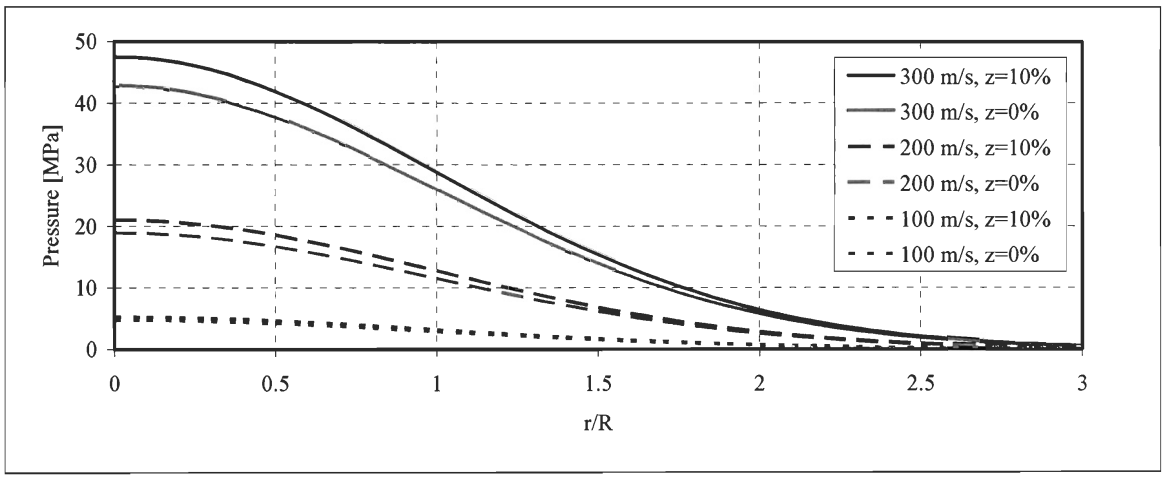

Figure 1.2 Pressure distribution along the radius for different impact velocities

With these tools, it is now possible to evaluate the data provided by Wilbeck.

1.3 Wilbeck's test results

Dr. James Wilbeck [1,22] was one of the first researchers to investigate the experimental behaviour of a bird under impact. His conclusions and results are very important to this day since they provide the shape and characteristics used for numerical bird models and the expected response of an impacted rigid flat plate, hence providing information to validate the model.

Several materials were tested for the search of a proper bird's substitute. The importance of the substitute is that all the projectiles can be uniform, thus making it possible to have a uniform reference frame for tests and certification procedures.

Substitutes such as gelatine, beef, RTV rubber, and neoprene have been tried out and compared against data from a chicken projectile. The validity of the substitute is assessed by comparing the pressure reading at the center of a flat rigid plate between substitutes impacting at the same velocity. Experiments showed that the most suitable substitute material is gelatine in which air is mixed to obtain a final porosity of 10% and an average density of 950 kg/m^3. Under impact, the gelatine adopts the same behaviour as water, and its low strength enables it to keep its shape until the impact, making it easier to handle and launch than actual water. Moreover, the density is slightly lower than water and equal to the average density of a bird if the cavities, bones, feathers, and other anatomical considerations are taken into account. In general, this density is considered adequate and is used as a reference in several numerical simulations for a gelatine material [1, 4, 5, 11, 13, 14, 16, 17, 22, 24, 27, 30, 31].

Tests also showed that the geometry of the projectile is of importance. The most suitable shape for the projectile is a cylinder with hemispherical ends with a length to diameter ratio equal to 2, as illustrated by Figure 1.3.

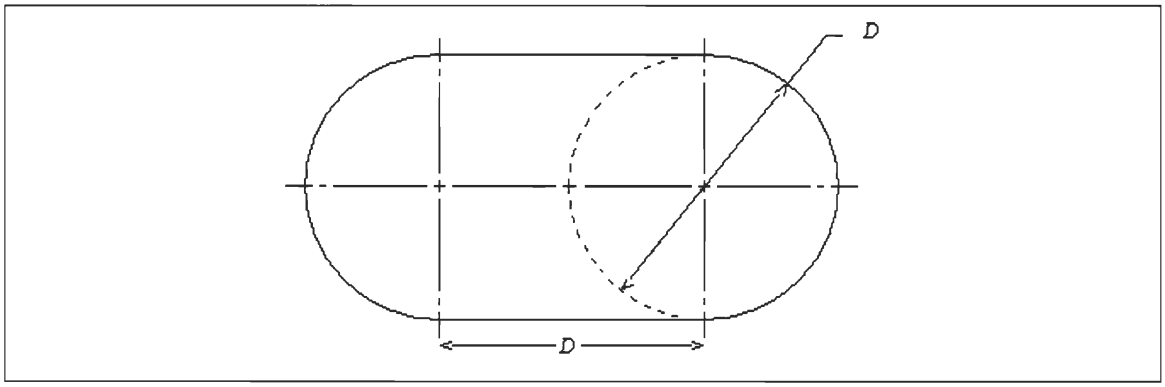

Figure 1.3 Bird model geometry

Budgey [30] and Stoll [12] have compared the finite element results obtained by using different shapes of birds such as a straight-end cylinder or an ellipsoid and have agreed that the geometry of Figure 1.3 is more adequate. McCallum [15] modeled a more detailed geometry that includes neck, wing and body. However, for certification purposes, the dead birds are compacted into a cylinder and launched as such, making the bird shaped as its container. Since the purpose of the simulations is to correlate to the certification, it is more appropriate to use the cylindrical shape.

As for the impact tests that Wilbeck conducted, several birds and substitutes were fired onto a rigid plate on which four piezoelectric quartz transducers were located along the radius with respect to the center of impact. Projectiles were fired at velocities ranging from 100-300 m/s perpendicularly and obliquely at angles of 25° and 45° with respect to the normal of the plate. The results are presented in normalized dimensions of pressure versus time where the pressure is divided by the stagnation pressure and the time by the duration of the impact (namely, the time it takes the bird to travel its length).

The results obtained for a bird projectile fired at three different velocities are presented in Figure 1.4. The results are good in the sense that there is a rise of pressure at the impact and then the pressure stabilizes around its stagnation value at around one third of the impact.

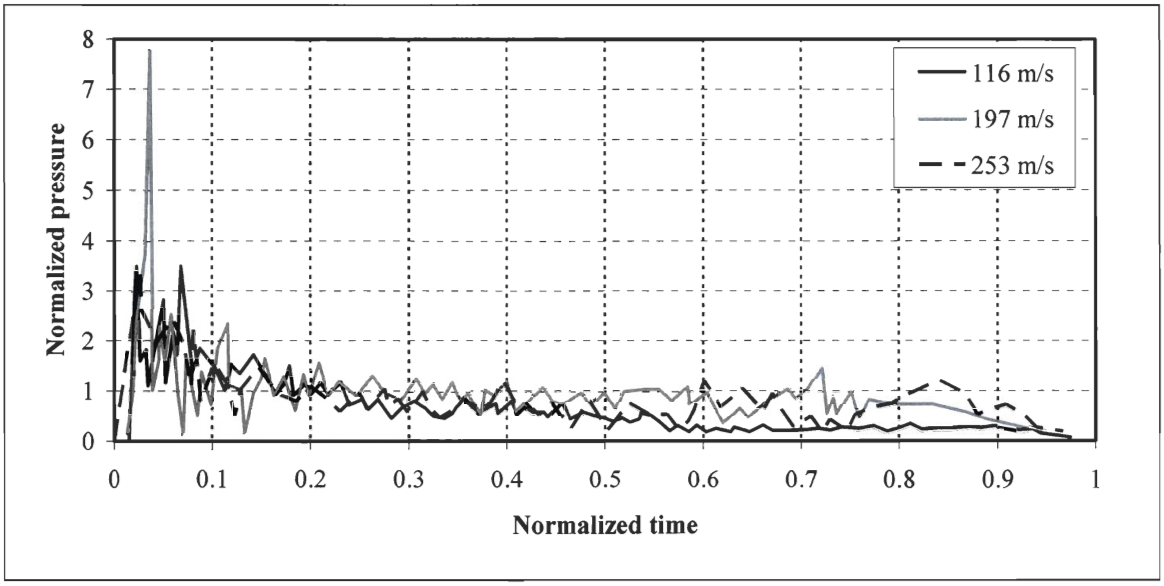

Figure 1.4 Wilbeck's results for the bird projectile

However, the values of the normalized Hugoniot pressure shown in Figure 1.4 are not consistent with the values obtained from the theoretical analysis, as clearly demonstrated in Table 1.1. This would be more acceptable if the experimental values displayed a decreasing trend with increasing velocity, similar to that of the theoretical values, but since this is not the case, one should not rely on the experimental results as far as maximum pressure goes.

Table 1.1 Normalized theoretical and experimental Hugoniot pressure

Velocity	Theoretical value	Experimental value
116 m/s	14.9	3.5
197 m/s	12.0	7.8
253 m/s	10.5	3.4

Part of the explanation of the maximums not being reached resides in the fact that the Hugoniot pressure is punctual and the duration of the impact is very short (in the range of milliseconds). Since the data obtained depend on the response time of the transducers used to measure the pressure, it is possible that the maximums were not properly captured.

In spite of the limitations of the available experimental data, it is still possible to create a respectably valid numerical bird model based on the material properties and shape of a bird

and the general behaviour of the pressure through time. The available modeling methods are described in the next section.

1.4 Numerical bird models

In the early stages of bird strike simulations, the bird was represented by a pressure pulse on the structure. This was based on the assumption that, since a bird is mainly made of water, it could be represented by a jet of fluid. Since then, many progresses have been made. The three main modeling methods that are currently available are: the Lagrangian mesh, the arbitrary Lagrangian-Euler (ALE) mesh, and the smooth particle hydrodynamic (SPH) method. The validity of a bird model is established by comparing the pressure impulse applied to a flat rigid plate to the theoretical and experimental values provided earlier.

In the present paper, a 1 kg bird is impacted on a 0.5×0.5 m square plate. The plate is meshed with 1,200 shell elements and made rigid by either using a rigid material or defining the appropriate boundary conditions. The material properties of the plate do not affect the results, but for the purpose of the simulations, steel has been used. The pressure is measured at an element located at the center of the plate.

As stated previously and demonstrated more recently by Airoldi [10] and others [30,31], the appropriate substitute bird has a density of 950 kg/m^3 and a porosity of 10%. Given the cylinder with hemispherical ends geometry of Figure 1.3, the diameter is of 93 mm and the total length of 186 mm. The simulations with the different bird models have been run in LS-DYNA 971 but can equally be done with most explicit finite element software.

Regardless of the modeling method chosen, the material usually used to model the bird is elastic-plastic-hydrodynamic [4,7,10,12,16,20,25,27] with an equation of state (EOS). It is well suited for bird strike because it behaves as an elastic-plastic material at low pressure, until the impact, and then it is governed by the pressure-volume relationship of the equation of state. This way, a low shear strength value can be given to the bird allowing it to retain its shape until the impact.

During the simulation effort, an elastic-plastic-hydrodynamic material model has been used for the bird with a shear modulus of 2.0 GPa, yield stress of 0.02 MPa and a plastic hardening modulus of 0.001 MPa. Those three parameters are more or less arbitrary and help the analysis to run smoothly which in itself should not affect the results since density is the dominant factor and not the material properties [18]. They are set according to the combined experience of other researchers found in the literature [12,27]. The values of the equation of state parameters are calculated according to equations (1.9) and (1.10).

1.4.1 Lagrangian bird model

The Lagrangian modeling method divides a volume into a large number of small geometries called elements. Because those geometries are simple in shape, it is possible to know the state of the solid through the simulation by using mathematical relations. However, when the deformations are large, it becomes increasingly difficult to calculate the state and stresses in the elements because the time step, based on the aspect ratio, keeps on decreasing. Moreover, the accuracy of the results obtained decreases. Also, since in this method the material moves with the mesh, if the material suffers large deformations, the mesh will also suffer equal deformation and this leads to results inaccuracy and numerical instabilities.

The birds modeled with solid Lagrangian elements are illustrated in Figure 1.5. The mesh size was found to have the most influence on the results; hence, two different mesh sizes were used. The first one, on the left, has an aspect ratio (element size vs. radius) of 5 and a total number of elements of 2,000 solid hexagonal elements, and the second one, on the left, has an aspect ratio of 10, for a total of 16,000 elements.

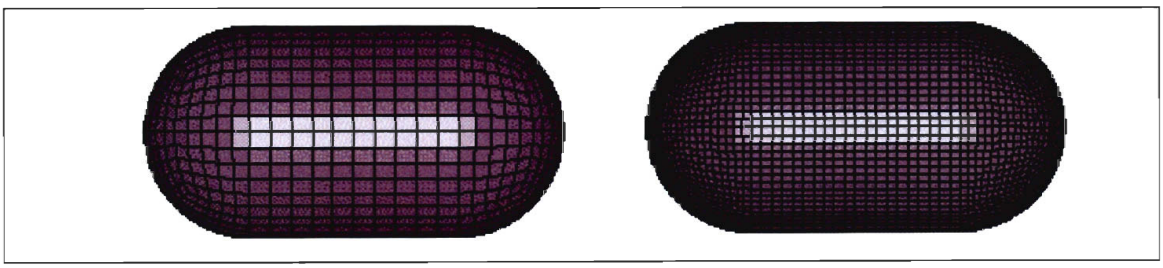

Figure 1.5 Lagrangian bird model with ratio 5 (left) and 10 (right)

The interaction with the target is controlled by a nodes-to-surface contact algorithm between the bird and the target [32] and in order to overcome large distortions, the elements were deleted when they reached a strain of 4.0, for the aspect ratio of 5, and a strain of 2.4, for the aspect ratio of 10.

1.4.2 ALE bird model

The second modeling method is the arbitrary Lagrangian-Euler (ALE) method. In this formulation, the material travels through the mesh. The initial idea of ALE modeling is taken from the Eulerian formulation for fluid flow where a material moves through a fixed mesh. The main difference is that, here, the mesh is allowed to deform and move so as to follow the flow of fluid. This represents a major improvement with respect to the Eulerian mesh because it decreases the size of the required mesh considerably.

At the beginning of the analysis, the denser material is concentrated in one part of the mesh, but as the analysis progresses, the fluid is allowed to flow everywhere. Some finite elements analysis software even makes it possible to only model the fluid [33]. At each time step, the position of the material is evaluated with respect to the nodes. The coupling with a solid structure is done by tracking the relative displacements between the coupled Lagrangian nodes and the bird. However, mesh distortion can become an issue with the ALE method if the elements' volume becomes negative, and it is often difficult to track material interface and history.

In LS-DYNA [32], the ALE bird uses the multi-material characteristic, allowing materials (air and bird) to coexist in an element prior to the start of the simulation. A total of approximately 19,000 solid elements of equal length, width, and depth are used to mesh the bird and its surrounding. Figure 1.6 shows a section the ALE mesh. On the left, the elements are shown, and on the right, only the portion of the elements with the heavier fluid (bird material) is shown.

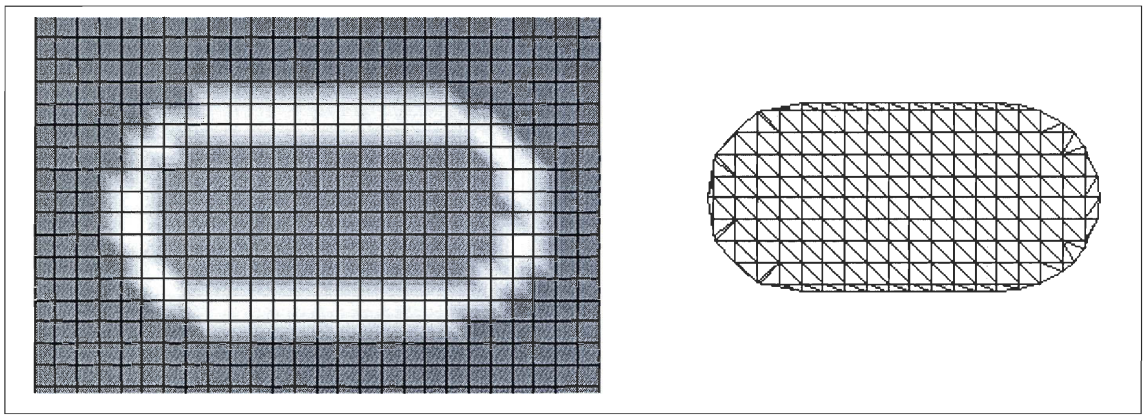

Figure 1.6 ALE bird model, elements (left) and fluid material (right)

The interaction between the bird and the structure is controlled by the *constrained-Lagrange-in-solid card [32]. When using the ALE method, this card is critical to obtain good results. It is important to allow coupling only between the bird and the structure, otherwise the gap of air can interfere. Also, the minimum volume fraction required for an element to be computed should be high enough so that the pressure rise is instantaneous once the bird strikes. Damping should be adjusted so that the pressure remains positive at all times.

Finally, the most important parameter is the penalty factor which governs the interaction between the fluid and the structure [34]. There are two coupling options: one can either adjust the penalty factor to a constant value, or use a load curve which will increase the stiffness linearly according to the penetration. Both options have been considered in the simulations.

1.4.3 SPH bird model

As an alternative, Langrand [7] suggested to look at the smooth particle hydrodynamic method. The SPH was developed by Monaghan [35] in the late 1970's for astrophysics problems with application to hypervelocity impacts (~10 km/s) where the material shatters upon impact. Because of the large deformation of a bird, this theory is also applicable to bird strike analysis in spite of the much lower velocity. Johnson [17] and McCarthy [4,20] have recently used this technique in their bird strike simulation with success, confirming its applicability.

The SPH method uses the Lagrangian formulation for the equations of motion but instead of a grid, it uses interpolation formula, called kernel functions, to calculate an estimation of the field variables at any point. The kernel function is active only over a given neighbourhood for each node, called support domain. Each node has a given mass and constitutes an element in the sense that the state variables are evaluated at each node location. The method is said to be mesh free because there is no predefined grid of nodes restraining which nodes can interact together.

In practice, the SPH method uses fewer elements than the ALE method, avoids the material interface problems associated with it and has a shorter solution time. It also follows the flow of the bird much more accurately than the previous methods, especially in the case of secondary bird strike (if the bird is deflected to another structural component).

Similarly to the Lagrangian mesh, the size of the SPH particles, or the amount of particles used, has an influence on the fluid-structure interaction, and hence the final results. A first model with 1,800 particles, each having a lumped mass 0.56 gram was used and the second model includes 4460 nodes, each having a lumped mass of 0.22 gram. The particles are evenly distributed, which is important because for the time being, the initial dimension of the support domain is the same for all the particles. Figure 1.7 shows the two SPH bird models.

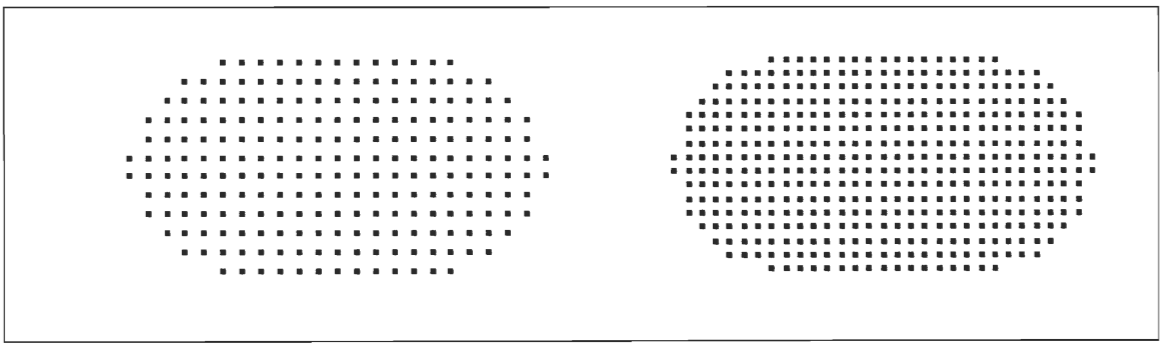

Figure 1.7 SPH bird model with 1,800 particles (left) and 4,500 particles (right)

The interaction with the structure is done through nodes-to-surface contact between the SPH nodes and the rigid wall, which is in agreement with the contact parametric study of Goyal [24].

1.5 Results & Analysis

This section presents the different numerical model used for each modeling method and then makes a selection of the most suitable model for each modeling approach. This selection is based on the pressure curves at the center of impact since the energy transfer between a bird and any target is directly related to the pressure. Afterwards, the three modeling methods are compared together with respect to the performance criteria identified in the introduction.

The results shown are based on an impact velocity of 116 m/s in order to establish a comparison with the results with the sample of experimental data previously presented. Thus, the Hugoniot pressure is expected to have a maximal value of about 93.6 MPa and a stagnation pressure of 7.1 MPa, giving normalized values of 13.2 and 1.0, respectively. Finally, the duration of the impact is of 1.6 ms. Similar results were obtained for the two other velocities for which experimental results are available but they are not shown since they lead to the same conclusions.

1.5.1 Lagrangian bird model

The pressures at the center of impact for the two Lagrangian meshes are plotted against the experimental pressure from Wilbeck in Figure 1.8. The shock pressure reached is of about 6.1, which is much lower than the expected value of 13.0. It is very little affected by the density of the mesh, but the bird represented with an aspect ratio of 10 presents a more stable steady flow pressure, and hence is the model preferred here. Airoldi [10] managed to obtain shock pressure that was much closer to the theoretical shock pressure, but he did so using a cylindrical bird model.

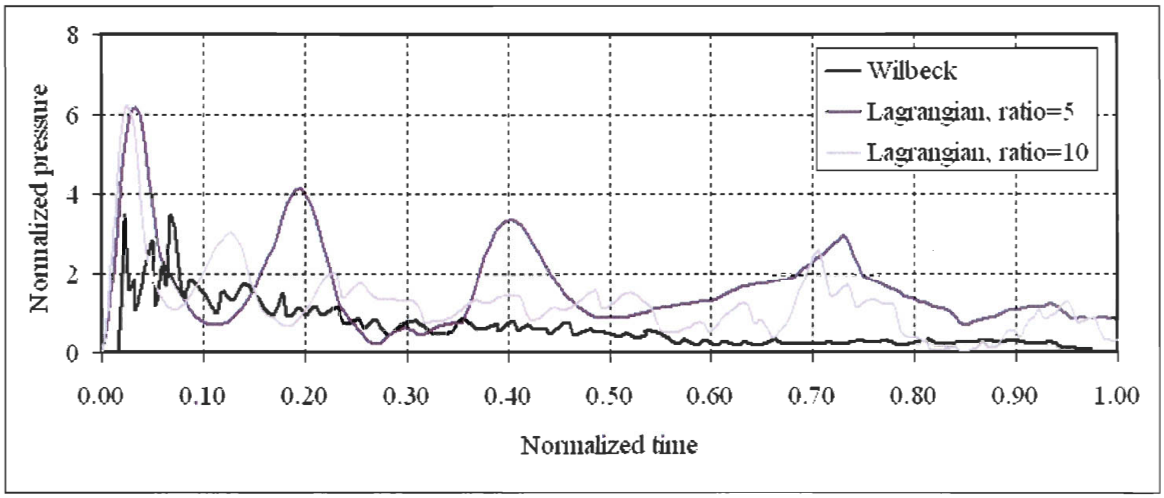

Figure 1.8 Normalized pressure of the Lagrangian models for a velocity of 116 m/s

As explained when describing the contact for the Lagrangian models, elements are deleted as they encounter severe distortions. This is a reality which is generally omitted, but considering Figure 1.9 it is obvious that a large amount of the bird comes to be neglected. By the end of the analysis, the Lagrangian bird with an aspect ratio of 5 has lost 14% of its initial mass, while the bird with an aspect ration 10 has a lost 62%. This tendency goes to show that while increasing the density of the mesh one might be able to increase the quality of the pressure results, more mass would be lost, hence never reaching an acceptable result.

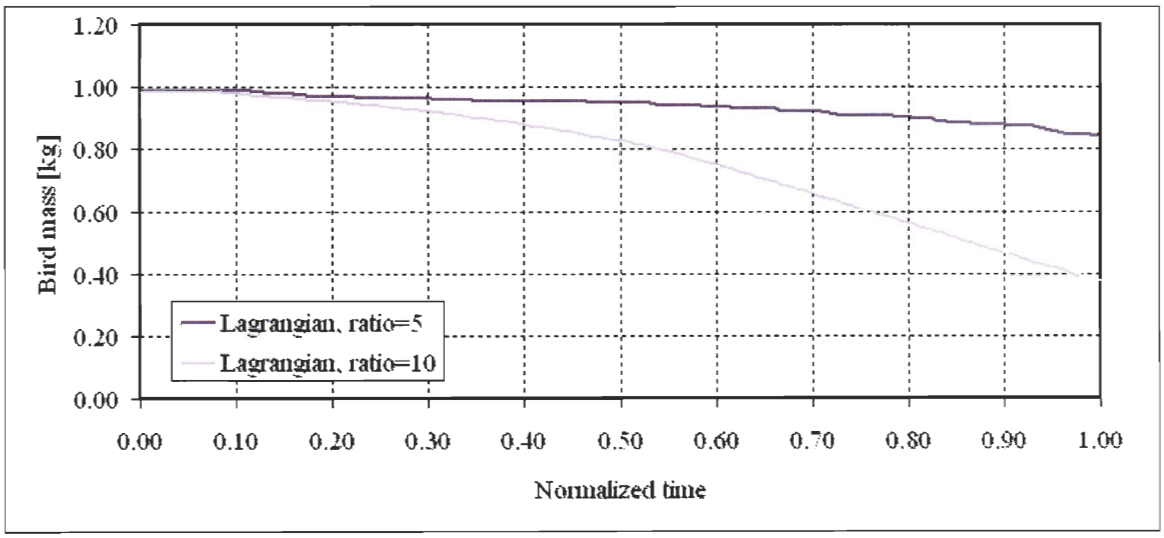

Figure 1.9 Bird mass loss during the impact

1.5.2 ALE bird model

The two coupling options, constant penalty factor and load curve, have been used to model a bird with the ALE method. The pressures at the center of impact are plotted in Figure 1.10. The difference between using a constant penalty factor and a load curve is very small and more noticeable at the beginning of the simulation, for the shock pressure. The load curve yields the exact expected value for the shock pressure, so it will be used in further analyses of the methods, but in reality, both options are equally valid. Note that using the load curve requires more adjustments when setting up the analysis and hence, a better understanding of the physics going on.

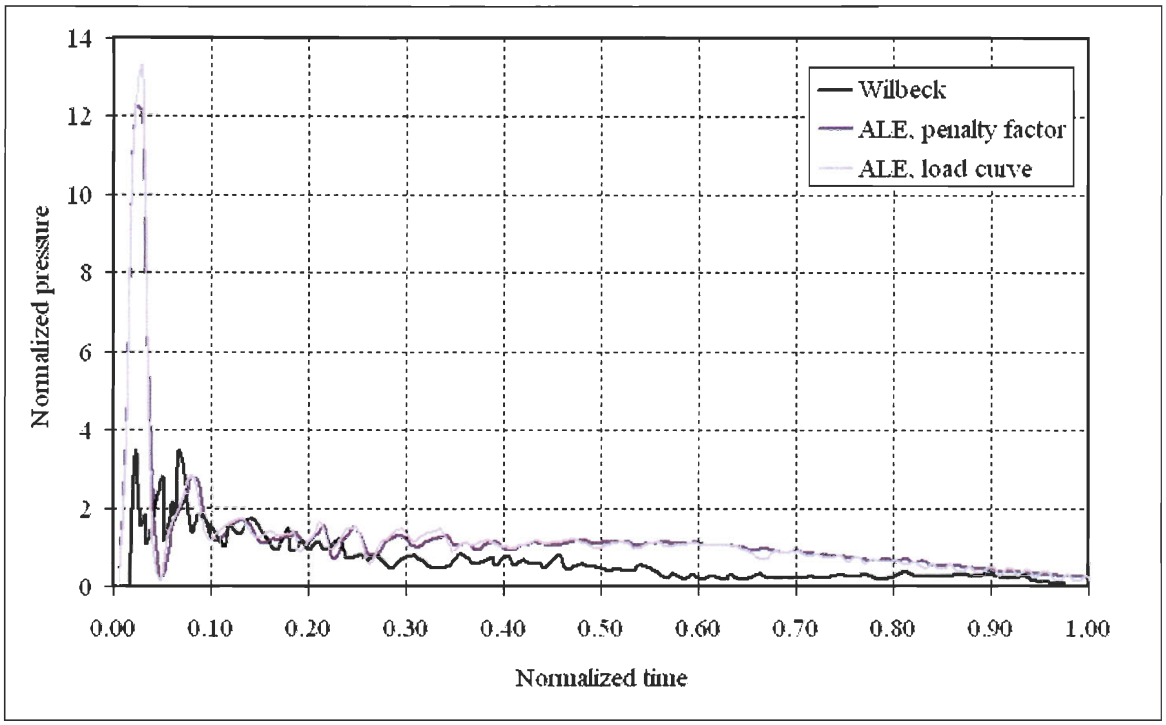

Figure 1.10 Normalized pressure of the ALE models for a velocity of 116 m/s

1.5.3 SPH bird model

The last modeling approach used is the SPH method. Increasing the number of particles clearly has an influence on the pressure results, as shown in Figure 1.11. Using 4,500 particles, which is the preferred solution, increases the peak value reached and the stability of the stagnation pressure. Further increase of the number of particles was not attempted since 4,500 is about four times the mesh density used by McCarthy [20], and twice that

used by Johnson [17] and both of them were successful in their use of the SPH method. Goyal [24] used even greater number of elements, but the size of the birds he worked with is not specified and one cannot ignore the strong correlation between the number of particles and the mass of the bird.

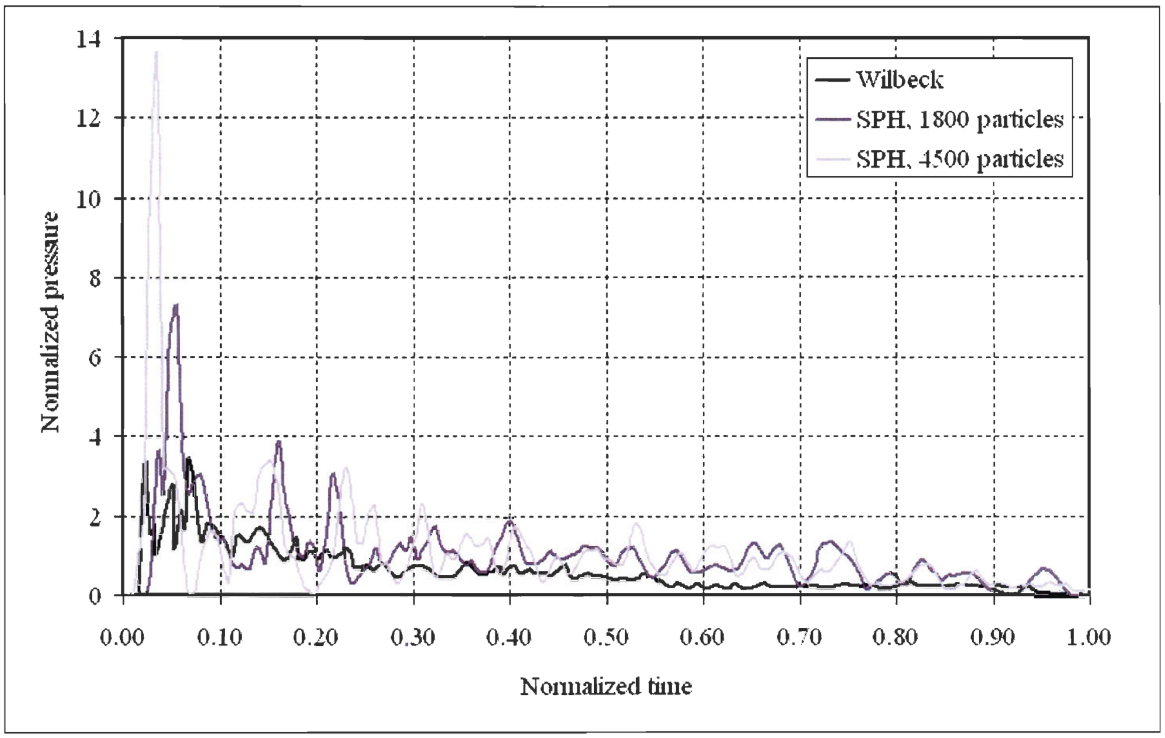

Figure 1.11 Normalized pressure of the SPH models for a velocity of 116 m/s

1.5.4 Pressure profile at the center of impact

Now, the best models of each method are compared together. The pressure curves of the selected solutions are presented in Figure 1.12. The fact that all solutions yield pressures that are greater than the experimental pressure is a reminder that the experimental data is a reference for the general behaviour rather than a tool of evaluation. It is good to notice that the shock pressures are reached simultaneously and that the stagnation pressure is reached at about a third of the simulations. Plotting the different methods together also highlight the fact that the Lagrangian results are much lower than the results of the ALE and SPH methods. They are also spurious, which can be attributed to the continual flow of elements being deleted. As for the ALE and SPH results, they yield a shock pressure which is almost

the same. The SPH pressure is more spurious than the ALE one, which is due to the method itself when each individual particle hits the target.

Finally, the mass loss has not been discussed for the ALE and SPH methods simply because they both preserve the initial mass which is important, especially if secondary impacts are to be studied. Looking at the results of Figure 1.12, it is possible to say that the performance of the SPH method, which is newer and still needs validation, is comparable to the ALE method.

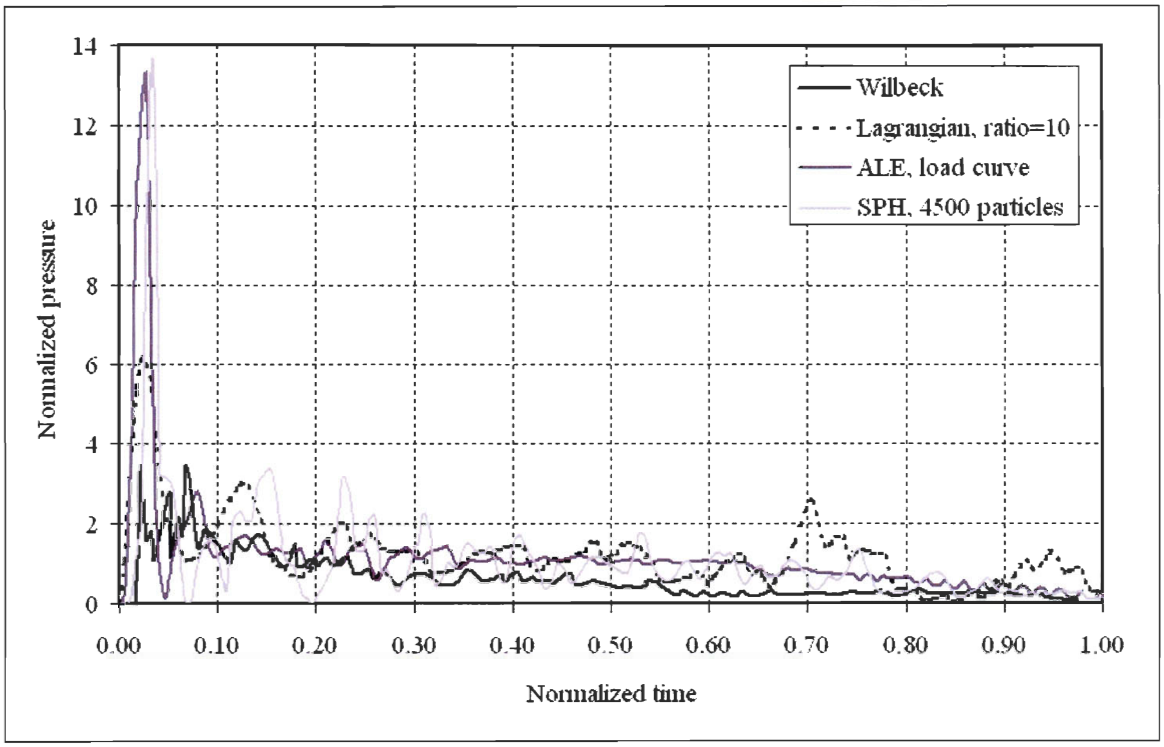

Figure 1.12 Pressure at the center of impact for the best solution of each modeling method

1.5.5 Impulse profile at the center of impact

Knowing the pressure at the center of impact zone and the area of the element, it is possible to calculate the force, and the impulse is obtained by integrating the force over time. Moreover, an approximation of the expected impulse can be calculated by integrating the force exerted on an element over time. In turn, the force is found from the pressure on an element and its area. In theory, the pressure stabilises around the stagnation pressure for

most of the impact. Given an element area of 216 mm^2 and the pressure calculated with equation (3) for an impact velocity of 116 m/s, the approximated value of the impulse is:

$$I = F\Delta t = P_{stag\ z} A\Delta t = 2.462\ \mathrm{N \cdot s} \qquad (1.13)$$

The impulses computed from the pressures of Figure 1.12 are plotted in Figure 1.13. The final values are slightly higher than the approximated one, which is consistent with the fact that the contribution of the initial shock pressure is not taken into consideration for the approximation. The fact that the three methods yield the same impulse value through time shows great consistency between the approaches. However, a word of caution regarding the impulse of the Lagrangian method since a fair amount of impulse is gained through unexpected peaks of pressure towards the end of the simulation. It would be highly interesting to establish a similar comparison with experimental data but the size of the measuring element is unknown at present.

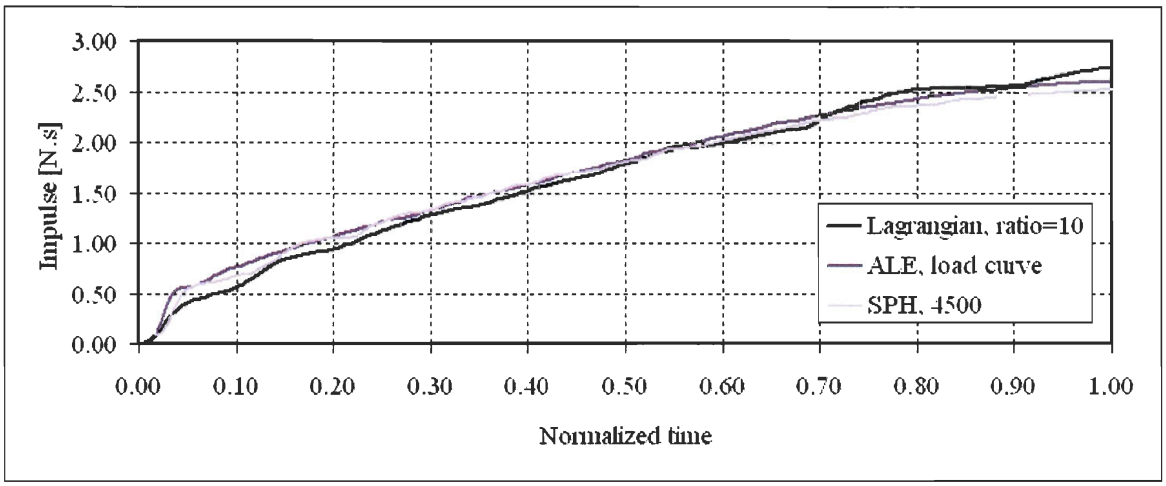

Figure 1.13 Impulse measured at the center of impact

1.5.6 Radial pressure distribution

The radial pressure distribution is plotted in Figure 1.14 according to the distance of the center of each element from the center of the target. Hence it is why the first reading is actually taken at a normalized radial distance of 0.22. The readings are taken when the simulations reach a steady state, at the normalized time 0.50 and the distance is normalized with respect to the radius of the bird. Of the three methods used, the ALE method is best

and displays a regular bell shape. The fact that the SPH method is spurious is obvious by the results and the Lagrangian method, although having a bell shape, has a larger offset from theory than ALE.

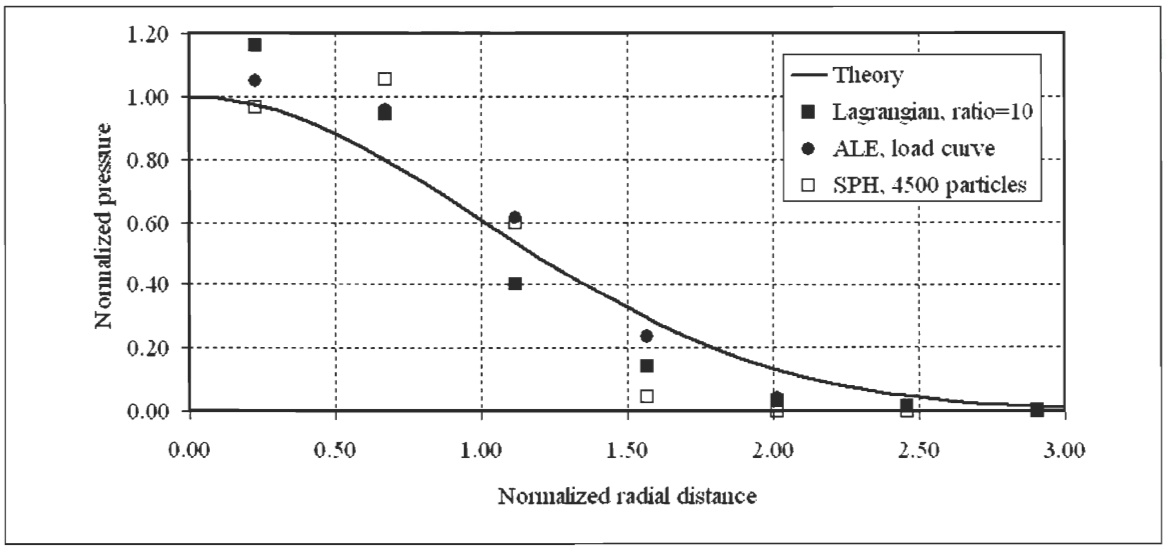

Figure 1.14 Radial distribution of the stagnation pressure

1.5.7 Shape of the deformations

The deformations of the birds through the simulations are shown in Figure 1.15. The ALE and SPH methods show a flow of the matter parallel to the target which is not displayed with the Lagrangian method since the elements are systematically deleted when they sustain too much distortion. In fact, two thirds of the elements are deleted by the end of the Lagrangian simulation. The SPH method seems to display bouncing particles that are not seen with the ALE method. This is in part due to the nature of the SPH method, but also to the fact that such a phenomenon would not be visible with ALE for very small amount of material.

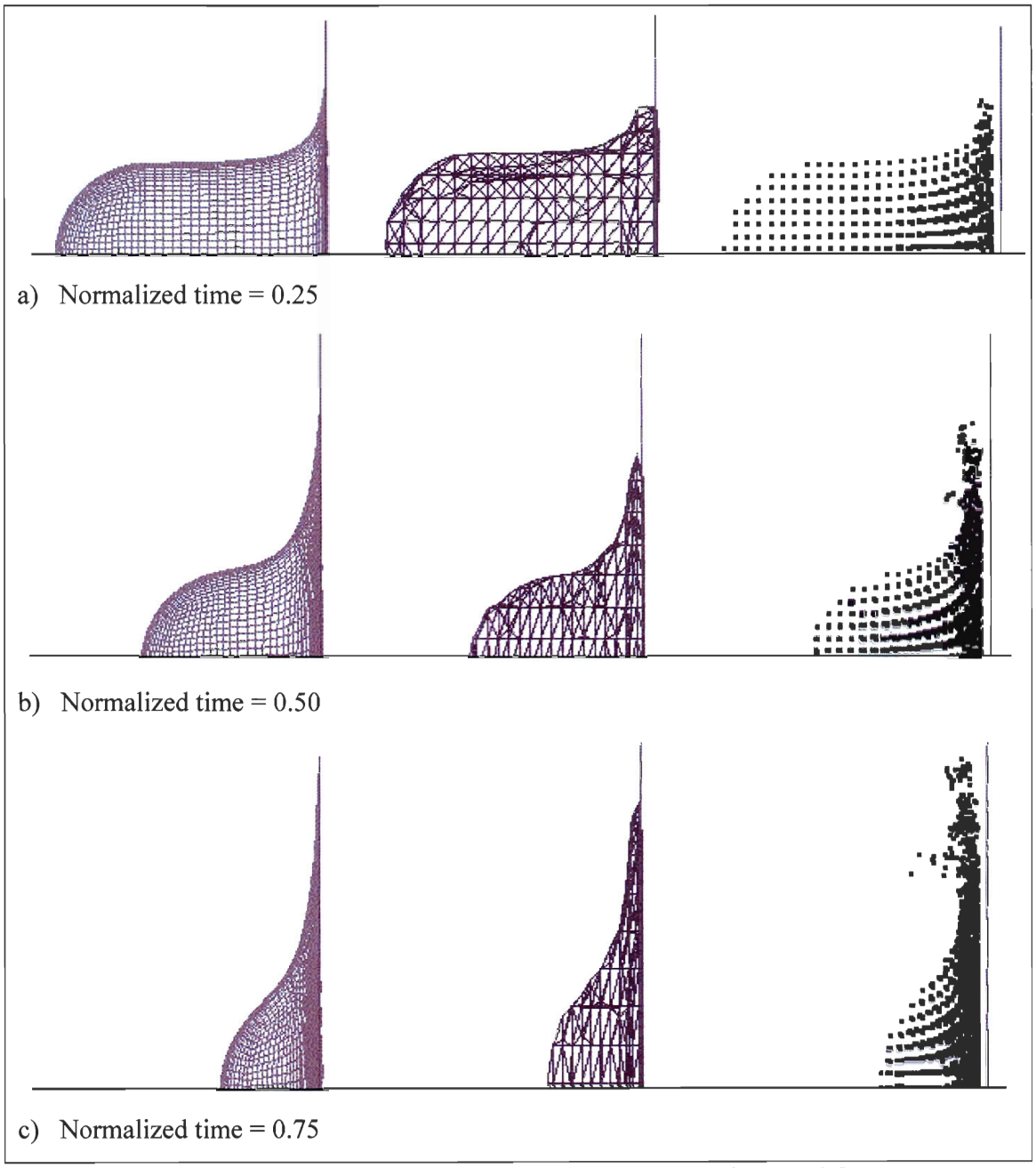

Figure 1.15 Deformations of the (a) Lagrangian, (b) ALE & (c) SPH models

1.5.8 Solution time

Finally, the solution times of the ALE and SPH methods are comparable and short, the SPH solution being slightly faster. However, one can expect the solution time of the ALE method to increase if more elaborate geometries are used. On the other hand, because the Lagrangian method encounters severe distortion, its solution time is thirty times longer than ALE and SPH in spite of having fewer elements than the ALE model. Goyal [24] obtained shorter solution times for the Lagrangian method than the SPH method, but then again, the Lagrangian mesh is not specified. Shorter solution time have been obtained in this project for the Lagrangian method using an aspect ratio of 3, but the pressure and distortion results were not even worth presenting.

1.6 Conclusions

The numerical bird modeling methods have been compared against theoretical and experimental values and compared together. The ALE and SPH models compare well with the theoretical predictions, but the comparison with the experimental data highlights the need for future bird calibration testing where radial pressure distribution and impact measure would be interesting additional measurements to register.

When comparing the bird models together, it becomes obvious that the Lagrangian method is no longer suitable. The pressure, mass loss and radial pressure distribution are inaccurate, to say the least, and when using a refined mesh, the solution time is long.

The ALE method gave very good results with respect to all the evaluation criteria once the proper set of parameters was found. During the course of the research, the SPH method seemed to be easier to implement with less parameters to adjust and yielded results that were comparable to the ALE method in terms of quality. Comparing the two methods gave further validation of the results obtained and showed the suitability of the SPH method to the bird strike problem.

The various criteria used to validate the models and methods are useful since they provide additional understanding of the phenomenon and a more thorough evaluation of the numerical results.

2 Bird's substitute tests results and evaluation of available numerical methods

2.1 Introduction

As stated in Chapter 1, the available test results date from 1977 [1] and do not correspond to the theory. The tremendous improvements observed since then in computer technology strongly suggest that the use of newer equipment would improve the precision of the data and provide a greater insight of the bird impact phenomenon. More recent tests were conducted, but those results are not available to the public [4,20]. Given those considerations, the need to perform new bird calibration tests was identified. The tests were performed at DRDC Valcartier in March of 2007.

This chapter summarizes the results and conclusions drawn from the tests. Its first purpose is to provide a gelatine bird recipe that could be used in bird certification process since each institution seems have an in-house recipe, which means that the tested projectiles vary from one place to another. The second objective is to provide information regarding the behaviour of the bird during the impact so that numerical models can be compared to a sound reference. The results are thus evaluated with respect to four of the six criteria identified in Chapter 1: (*i*) the deformation of the projectile through the impact, (*ii*) the pressure read by the acquisition system, (*iii*) its radial distribution, (*iv*) the level of energy transferred to the target. The mass loss and solution time pertain exclusively to numerical simulations and are thus not discussed here.

Finally, numerical simulations using the arbitrary Lagrangian-Euler (ALE) and smoothed particles hydrodynamics (SPH) methods were performed in order to verify how well those tools really performed. It is believed that numerical tools could be used as part of the bird impact certification process in the future to limit the amount of experimental testing required and the costs involved.

This chapter is organized as follow: Section 2.2 describes the experimental set-up, the experimental results are given in Section 2.3 and are compared with the numerical results in Section 2.4.

2.2 Experimental Set-Up

The tests were conducted at DRDC Valcartier. Figure 2.1 shows a sketch of the experimental set-up where the main components are identified. Basically, the air compressor provides air pressure that accelerates the bird and sabot while they are being pushed out of the cannon. Then, a sabot stripper liberates the gelatine bird before it hits the rigid target. The following subsections give the details of the different components that came into play for the tests.

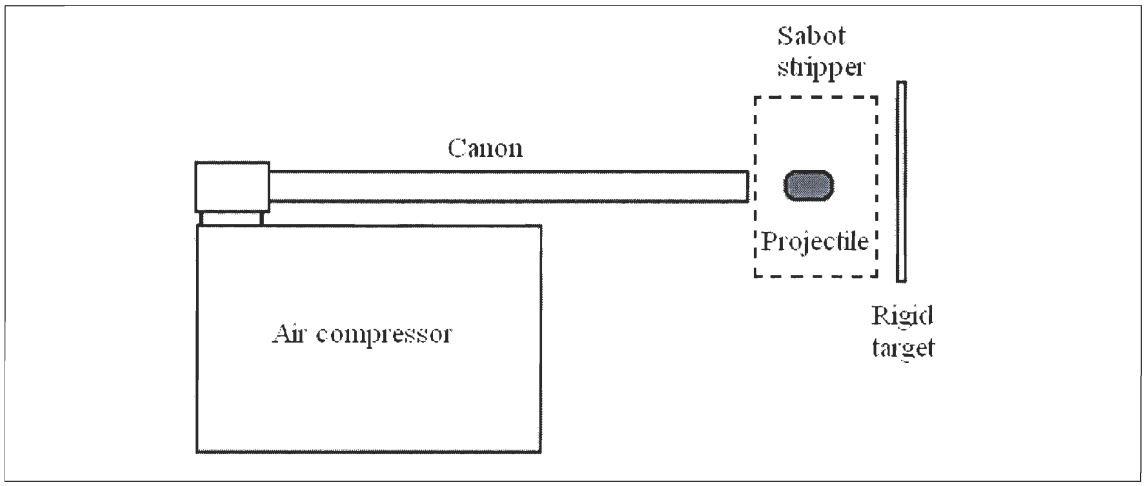

Figure 2.1 Sketch of installations

2.2.1 Installations

Compressed air from the building was available at 690 kPa [100 psi] and pumped into a reservoir. However, the pressure was insufficient to reach high projectile velocity and Helium reservoirs were used in the end. It was possible to reach a pressure of 1240 kPa [180 psi] with the Helium and since its expansion rate is faster than air, it provided a better acceleration. When the desired pressure was reached, a 5.0 cm [2 in] quick release valve was triggered. The projectile was inserted at the muzzle of the cannon by taking apart the link between the quick release valve and the cannon. The cannon is shown on Figure 2.2.

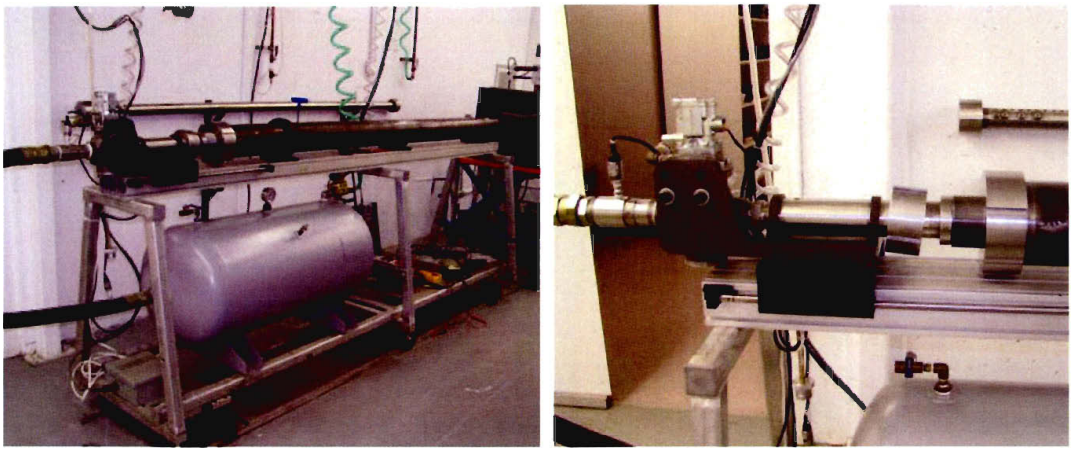

Figure 2.2 Cannon (left) and quick release valve with muzzle of cannon (right)

A series of holes located before the exit of the cannon allows the pressure to drop so that the projectile's velocity becomes constant before exiting the cannon. Two infrared sensors located at the exit of the cannon were used to measure the velocity. Each sensor was triggered when the beam was interrupted by the moving projectile, and the velocity was obtained from the time delay and distance between the two set of sensors, which are 7.6 cm [3 in] apart. The sabot-trap and the cone are located right after the nozzle of the cannon. The purpose of the cone is to separate the bird and the sabot, and the sabot-trap ensures that the sabot does not impact on the target. The bore diameter in the cone is meant to let the bird go through and split open the sabot. The infrared sensors with the series of holes and the inside of the sabot-trap are shown in Figure 2.3.

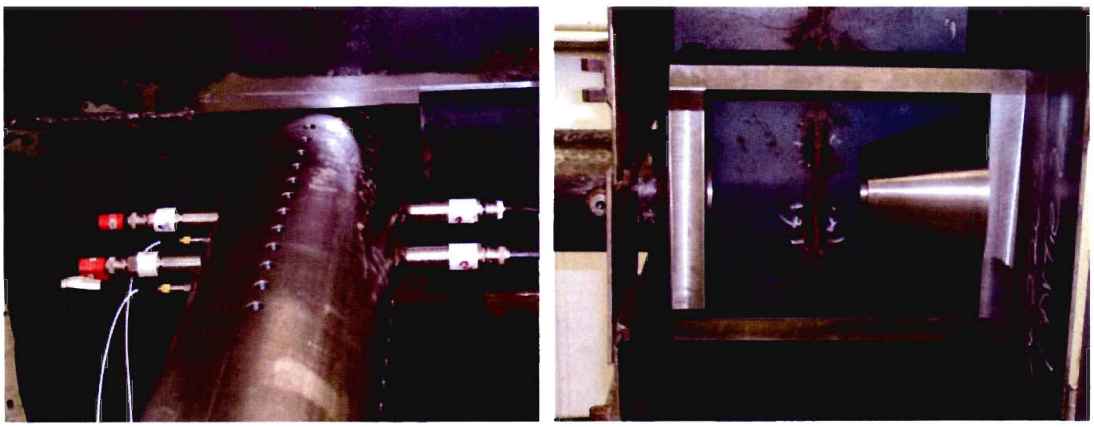

Figure 2.3 Infrared sensors (left) and sabot-trap with cone (right)

Next is described the projectile which is defined as the mass to be accelerated by the canon. In this instance, it is made up of the gelatine bird and the sabot. Both components are described in the two following sections.

2.2.2 Gelatine recipe

The gelatine recipe usually used at DRDC was found to yield birds that were too dense. As recommended in the literature [1,36], phenolic micro-balloons were added to decrease the density but the resulting gelatine bird was not uniform since equipment to keep the bird rotating during the solidification process was not available. Hence, successive mixtures were tried to develop a new recipe which would give a bird with the following characteristics:

- Density of 950 kg/m^3;
- Uniform projectile;
- The mixture must be liquid enough to be poured into the moulds when prepared and yet stiff enough to be launched once solidified.

The proportions of the different ingredients in the recipe did influence its texture, and hence its mechanical properties. However, it is important to recall that the mechanical properties of the projectile, such as the yield and shear stress, are of very little importance in the hydrodynamic range and that density is the crucial parameter [18].

Different gelatine birds are illustrated in Figure 2.4. The first bird illustrated in Figure 2.4 (a) is made of pure gelatine and has a density of 1090 kg/m^3. Then, the phenolic micro-balloons were added, but besides adding color to the initial gelatine mixture as shown in Figure 2.4 (b), they did not influence the density since only a very small amount could be used in order to preserve the homogeneity of the projectile. On the other hand, the procedure given in Table 2.1 gives bird with a density around 970 kg/m^3, which is much closer to the desired value of 950 kg/m^3. The substitute obtained is illustrated in Figure 2.4 (c) and the final mechanical properties are sufficient for the projectile to hold its shape during the acceleration.

Figure 2.4 **From left to right: (a) pure gelatine, (b) micro-balloons, and (c) final bird**

Table 2.1 **Gelatine's preparation procedure**

Ingredient
□ 1000 gr cold water □ 100 gr ballistic gelatine powder □ 25 gr sodium carboxymethylcellulose (CMC) □ 6 gr aluminum acetate basic (AAB) □ 4 drops of cinnamomum zeylanioum (cinnamon)
Procedure
1. Mix the cold water and gelatine, wait 5 minutes 2. Heat up the gelatine mix to 45 deg C 3. Meanwhile, weight the AAB and sodium CCM and mix them together 4. Weight 1050 gr of the gelatine mix and pour into the blender 5. Add 4 drops of cinnamon 6. Start the blenderAAB acetate basic and sodium CMC mixed 7. Close the lid and let spin at the lowest speed for 3-5 seconds 8. Stop the blender, pour into the mould and cool off in the refrigerator for 24 hours

The phenolic micro-balloons are no longer used in the procedure given in Table 2.1 since the CMC agent creates porosity on its own. Moreover, when the mixture is spun in the blender, air is trapped in it, which explains the white color of the projectile. In fact, the cinnamon is added to control the amount of air bubbles. Finally, the AAB is a solidifying agent which works with the gelatine to give a projectile that can be launched.

2.2.3 Sabot

The purpose of the sabot is to protect and guide the bird during the acceleration and prevent it from sticking in the cannon. The sabot is made of HDPE (high density polyethylene) and is designed for a single use since it is destroyed by the sabot trap to free the gelatine projectile. The mass of the sabot is approximately 400 gr. The design of the sabots used is shown in Figure 2.5. It is cut in two and material is removed along the length to minimize the weight and provide more acceleration to the projectile.

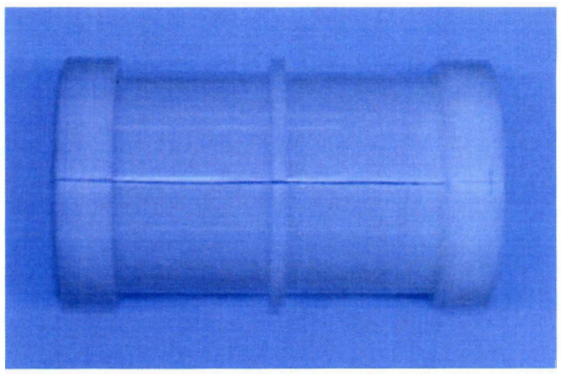

Figure 2.5 Sabot

Additionally, a punch was used to create small indents in along the circumference of the sabot in order to increase the frictional force between the sabot and the interior wall of the cannon to allow for a pressure build-up prior to acceleration. Thus, the projectile sabot permits to accelerate and guide the gelatine bird until it is stopped by the sabot-trap and frees the gelatine bird which impacts on the target. The target is the topic of the next section.

2.2.4 Target

The target illustrated in Figure 2.6 is of 30.5 cm×30.5 cm [12 in×12 in] with a thickness of 1.3 cm [½ in] and is clamped on the support along the edges. It is made of rolled homogeneous armour (RHA) steel and has small slots which allow the legs of the carbon gages, which are used to measure the pressure, to be connected behind the plate so that the connections are protected from the impact. Moreover, a 0.2 cm [$\frac{1}{16}$ in] layer of Lexan protects the carbon gages themselves. The plate was cleaned using a CS-201 solvent, and then a 14-02 type of epoxy was used to bond the Lexan to the plate.

The target is held on the support shown in Figure 2.7 where each wheel is clamped to the rails on the floor to ensure that the support is rigid and does not move. It is possible to verify that the target is well aligned on the axis of the cannon using a laser beam inserted at muzzle of the cannon.

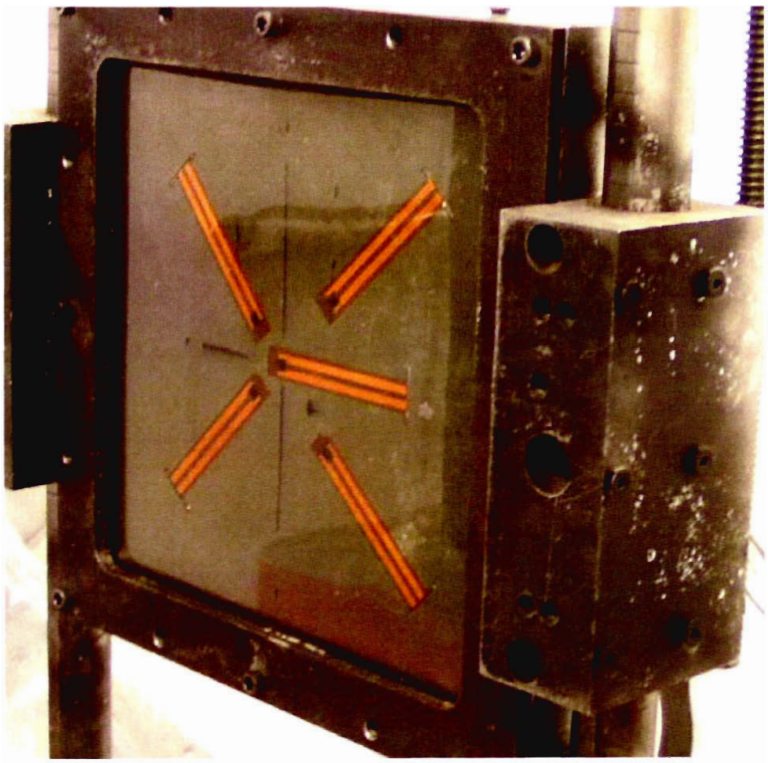

Figure 2.6 Target on its support

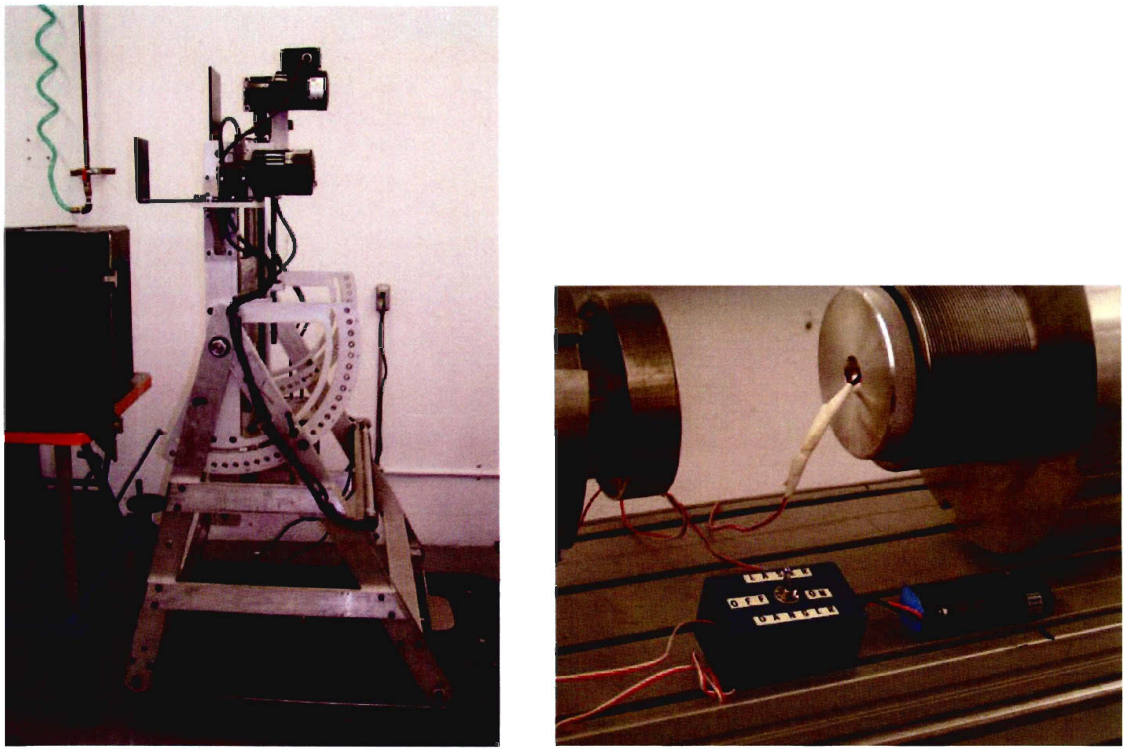

Figure 2.7 Target anchor system (left) and laser for target alignment (right)

2.2.5 Data Acquisition

Two types of data are expected from the tests. First, a video camera, shown in Figure 2.8, records the event. A sampling rate of 3000 frames per second was used for most of the test. In two of the tests, the sampling rate was increased to 20,000 frames per second so that the camera could be used to measure the velocity of the bird. The difference between the reading of the infrared sensor and the camera was less than 2%, thus confirming that the velocity measured by the infrared sensor is correct and that the bird did not decelerate once it is freed from the sabot.

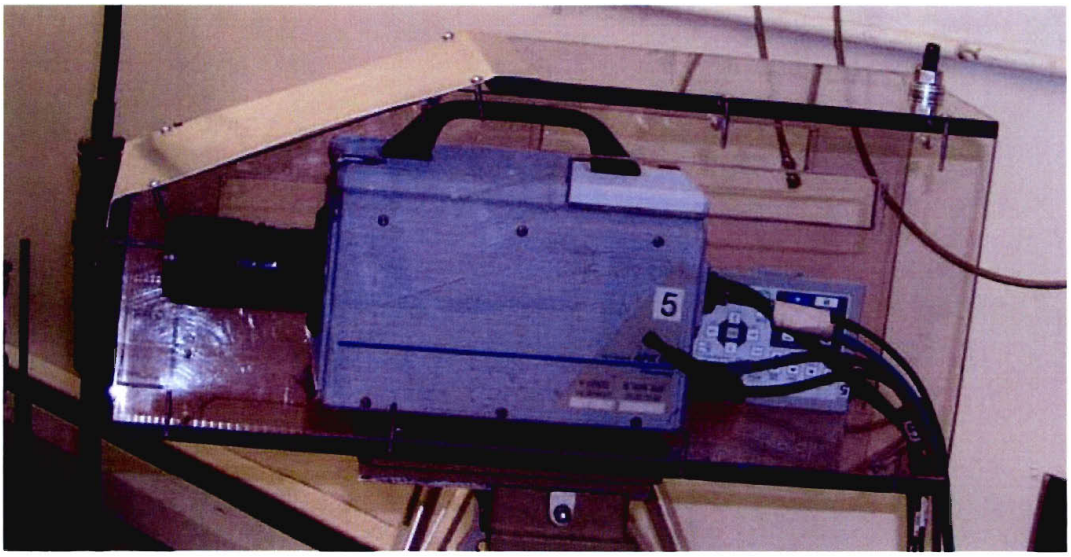

Figure 2.8 High-speed video camera

Second, piezo-electric carbon gages were used to measure the pressure applied by the bird on the rigid target. Carbon gages, model C300-50-EKRTE [38], were used. Their specifications are the following:

S/N	nil
Sensitivity	1000 mV
Antialiasing filter	50 KHz
Gain	500
Excitation	1.5 (V)
Dimensions	0.5 cm× 0.6 cm [0.2 in×0.25 in]

Five carbon gages were glued to the target according to the pattern shown in Figure 2.9. Each carbon gage was mounted as a quarter bridge (similar to Wheatstone bridge) and connected to a Quad Bridge signal Conditioner system, model 28134 from Precision Filters. This system amplifies and filters the input signal. The voltage going in each bridge was of 1.5 Volt DC. Type Bessel 6 poles anti-aliasing filters were used with a cut-off frequency of 50 kHz. The signal from each gage was amplified with a gain of 500 in order to have a reasonable amplitude for the voltage and to minimize noise during the recording of the signals.

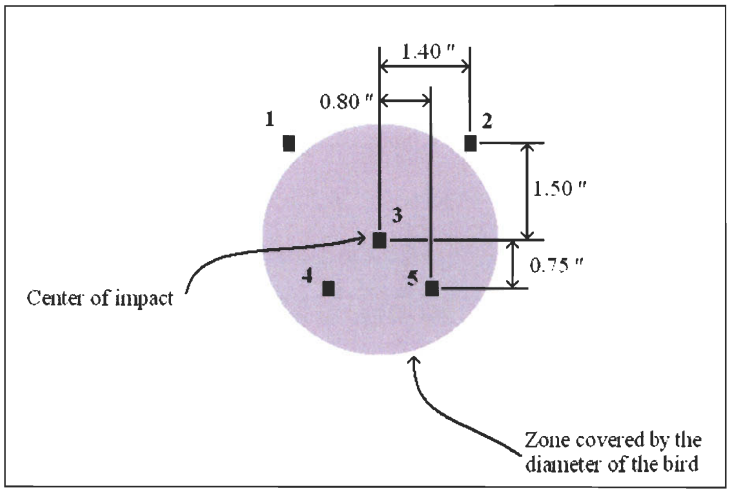

Figure 2.9 Carbon gages position on target (units in inches)

The voltage outputs from the five gages were continuously monitored, displayed in real time and recorded during the tests using LDS GENESIS data acquisition system. The acquisition module was 845-078000 Basic1M ISO. The sampling rate was of 1,000,000 samples/sec and a high pass filter with a frequency of 100 kHz was used. Each acquisition modules had a memory of 128,000,000 readings and a resolution of 16 bits. The control software was called PERCEPTION 3.02, from LDS as well, and the software used to analyze the signals is FLEXPRO 7.0 from WEISANG. The cables used were Belden cables with 3 pairs of wires and individual blinding.

The voltage output is converted to resistance using the equation provided by the manufacturer DYNASEN [38]:

$$\frac{\Delta R}{R} = \left[\frac{86.6}{R_0} \left[\frac{86.6}{86.6 + R_0} - \frac{V_S}{K_R} \right]^{-1} - 1 - \frac{86.6}{R_0} \right] \times 100(\%) \qquad (2.1)$$

Where: $$K_R = \frac{V_C}{\frac{86.6}{R_0 + 86.6} - \frac{86.6}{R_0 + 86.6 + \Delta R_C}}$$

V_S : Signal voltage

ΔV_C : Calibration voltage for a simulated change of resistance $\left(\Delta R_C / R_0 \right)$

ΔR_C : Change of resistance during the calibration procedure

ΔR : Change of gage resistance during the test procedure

$\Delta R_C / R_0$: Relative change of resistance, (%)

A calibration curve provided by Dynasen [38] was then used to determine the stress corresponding to the resistance measured. The calibration curved was approximated by the following equation:

$$\sigma_X = 0.255\left(\Delta R/R_0\right) + 0.00075\left(\Delta R/R_0\right)^{2.2} + 0.0000021\left(\Delta R/R_0\right)^4 \qquad (2.2)$$

During the test, it was found that the acquisition system was sensitive to interference from the electrical system. Thus, it was important to turn off the lights to avoid getting high unphysical peaks in the pressure reading.

2.2.6 Procedure

During the tests, the following experimental procedure was followed:

1. Weigh the sabot
2. Weigh the gelatine bird
3. Verify that the axis of the cannon and the center of the target are aligned using the laser
4. Punch the sabot on its circumference to increase the frictional forces between the sabot and the inside of the cannon
5. Cover the gelatine bird with Crisco oil and insert it in the sabot
6. Insert the sabot with the gelatine bird into the cannon, leaving a gap of about 1 in behind the sabot
7. Close the cannon
8. Turn off the ceiling lights
9. Evacuate people from the test's chamber
10. Proceed with test
11. Increase the pressure near 180 psi
12. Activate the infrared sensor

13. Activate the release valve when the pressure is equal to 180 psi
14. Note the projectile's velocity
15. Wait until it is safe to return in the test's chamber
16. Observe the debris of the bird and sabot outside of the sabot-trap
17. Verify that the target is intact
18. Weigh the sabot's debris found inside the sabot-trap
19. Verify that the sabot-trap is undamaged
20. Clean-up the bird debris
21. Save the data from the video camera and the gages

2.3 Experimental Results

The results are analyzed with respect to the deformation of the bird, the pressure reading, and the energy of the impact. Each of those aspects is discussed in the sub-sections that follow.

2.3.1 Data from the video camera

Snap shots taken by the camera for the impact at 0° with the pure and the gelatine mix and for the impact at 30° with the gelatine mix are shown in Figures 2.10, Figure 2.11 and Figure 2.12 respectively. Note that the ring around the birds is a strip from the sabot; its mass is not significant and it does not impact the target, so it has no influence on the actual results.

The snap shots are taken at time intervals of 0.33 ms, where the start time is when the nose of the projectile touches the target. The three figures demonstrate well that the projectile has a hydrodynamic behaviour during the impact, which is consistent with past experience. This also confirms that the mechanical properties of the projectile are not significant in the energy transfer during the impact and that the density is the primary parameter of concern.

The mixture developed for the projectile proved to be very adequate; it was easy to manufacture, handle and launch. On the other hand, the difference between using pure gelatine and the gelatine mixture is well illustrated by Figure 2.10, where the deformations are quite different from that of the porous mixture, as shown in Figure 2.11. It is therefore

demonstrated that the porosity affects the results, at least as far as the deformations are concerned.

Another approach used to analyze the data from the camera is to measure the velocity of the bird while it is impacting as well as its diameter on the plate. The information is plotted on Figures 2.13 and 2.14 for the impact angles of 0° and 30°, respectively, for three different tests.

Although the time intervals are large, a general trend of the behaviour can be observed. In general, the diameter of the bird on the target increases as the impact progresses and stops when the debris of the projectile reaches the edges of the target. The velocity of the bird is measured by averaging the displacement of the end of the projectile over the time interval between each snap shot. A decrease in the projectile's velocity is observed past halfway of the impact process, when it has lost most of its momentum. The information contained in Figures 2.13 and 2.14 will make it easier to assess the behaviour of the numerical bird.

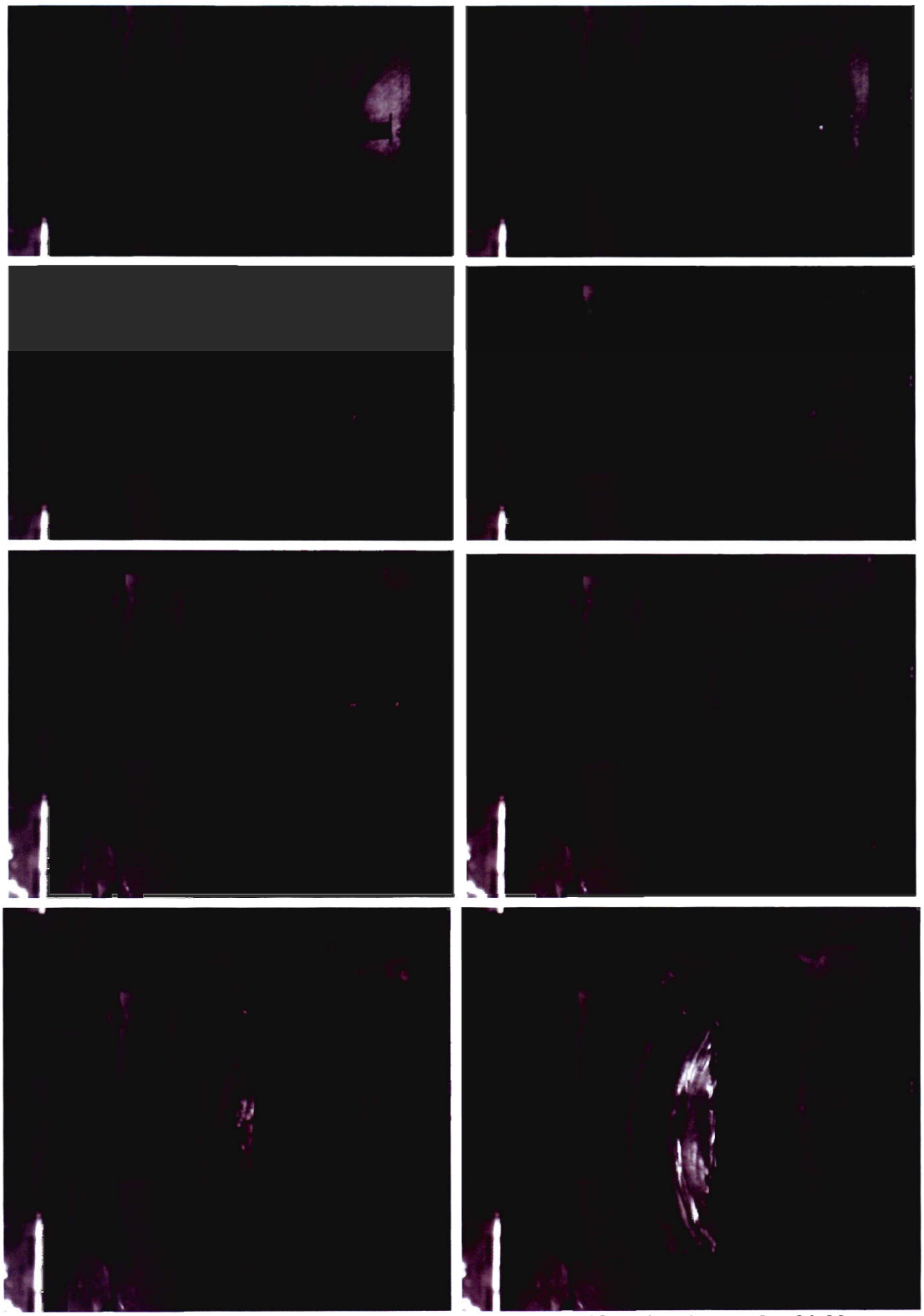

Figure 2.10 Snap-shots of bird with pure gelatine, angle 0° at time intervals of 0.33 ms

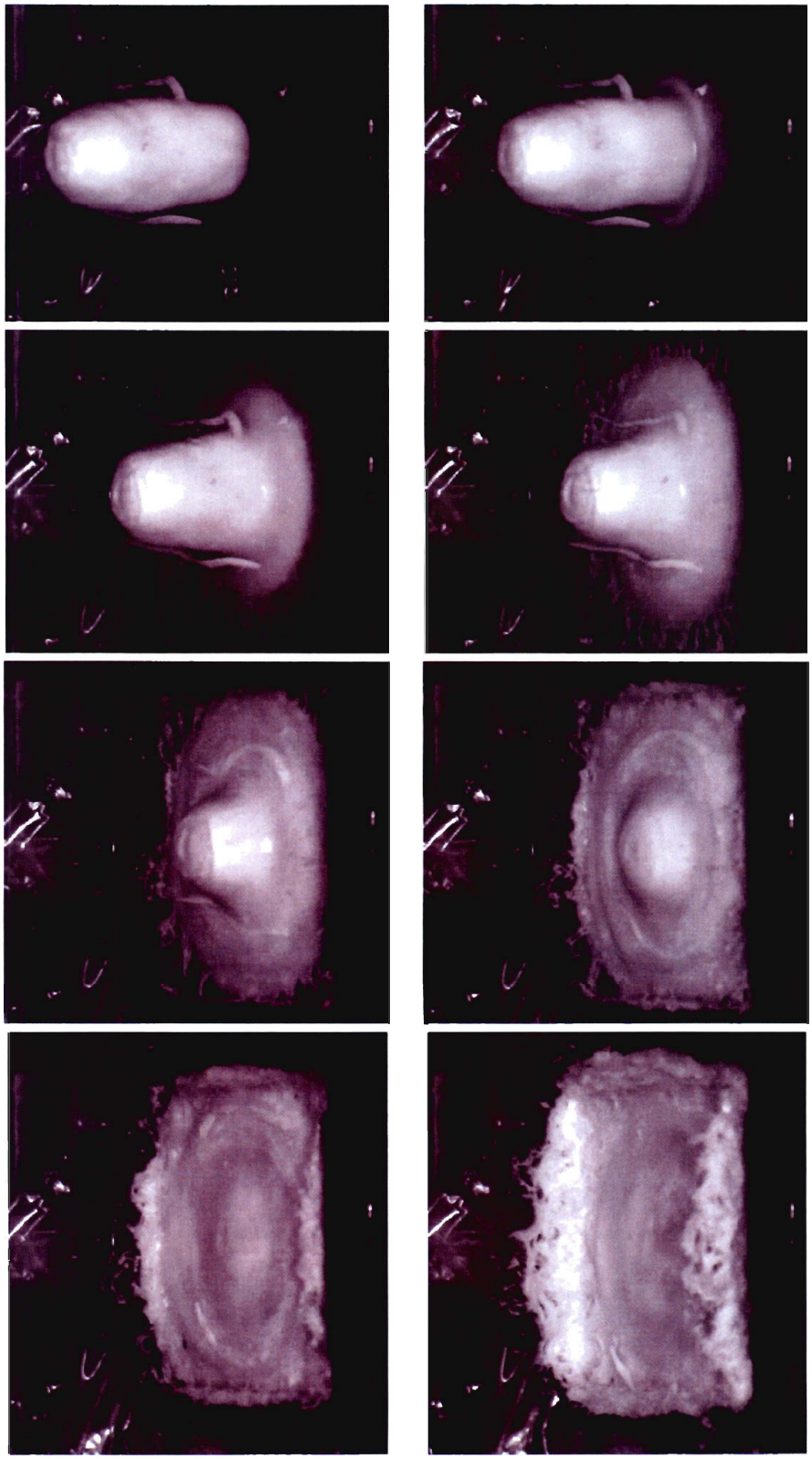

Figure 2.11 **Snap-shots of bird with mix gelatine, angle 0° at time intervals of 0.33 ms**

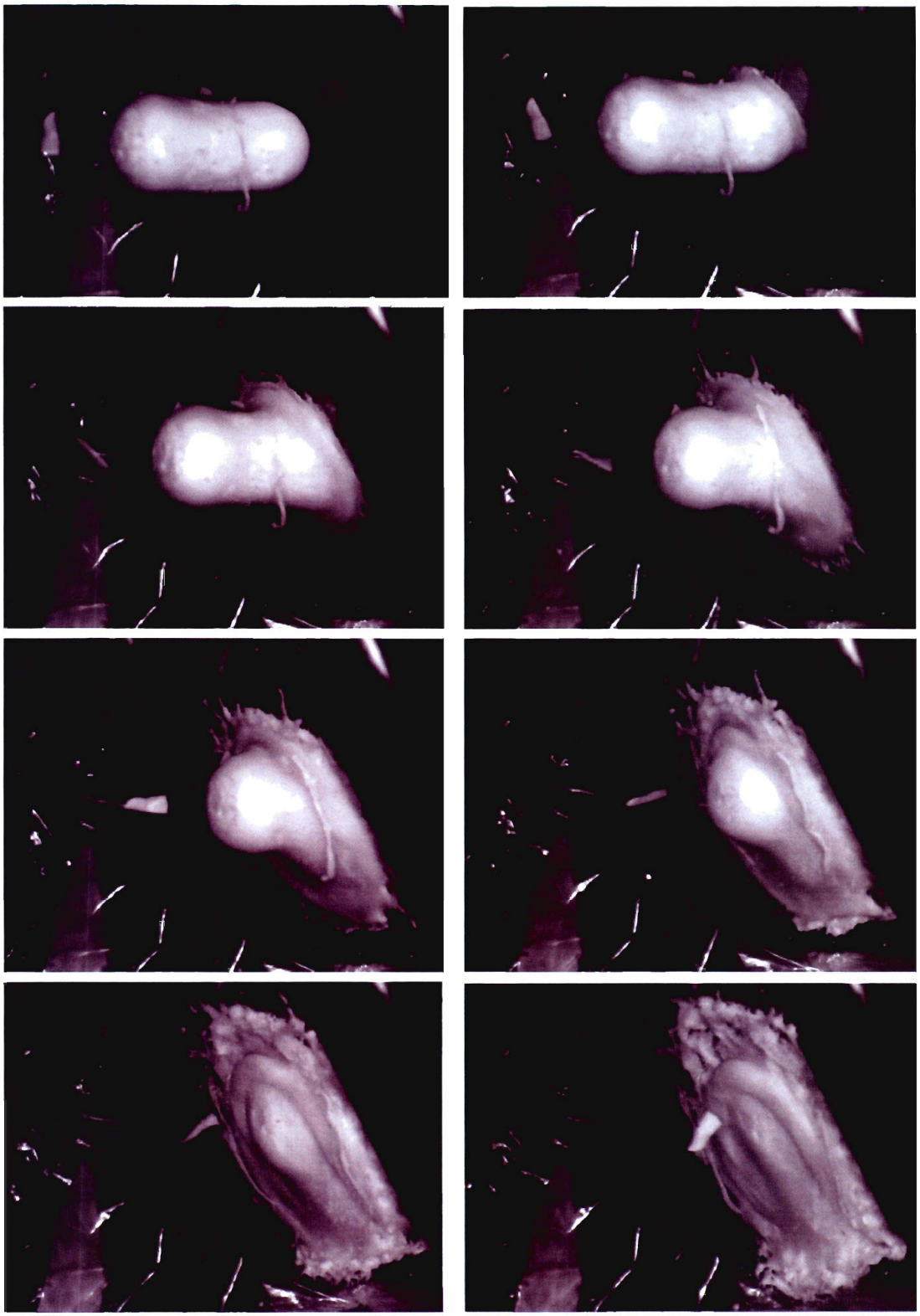

Figure 2.12 Snap-shots of bird with mix gelatine, angle 30° at time intervals of 0.33 ms

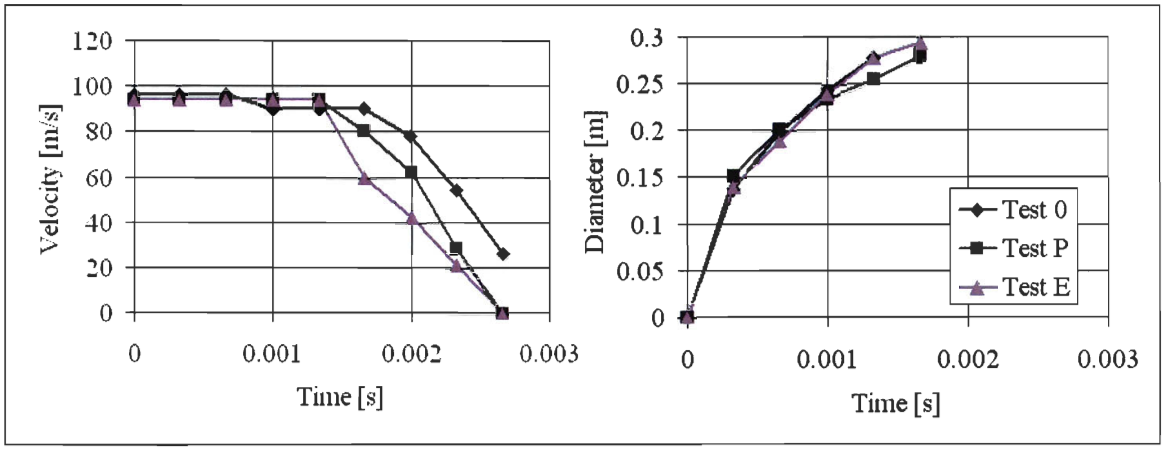

Figure 2.13 Variation of velocity (left) and diameter (right) of the projectile at 0° angle

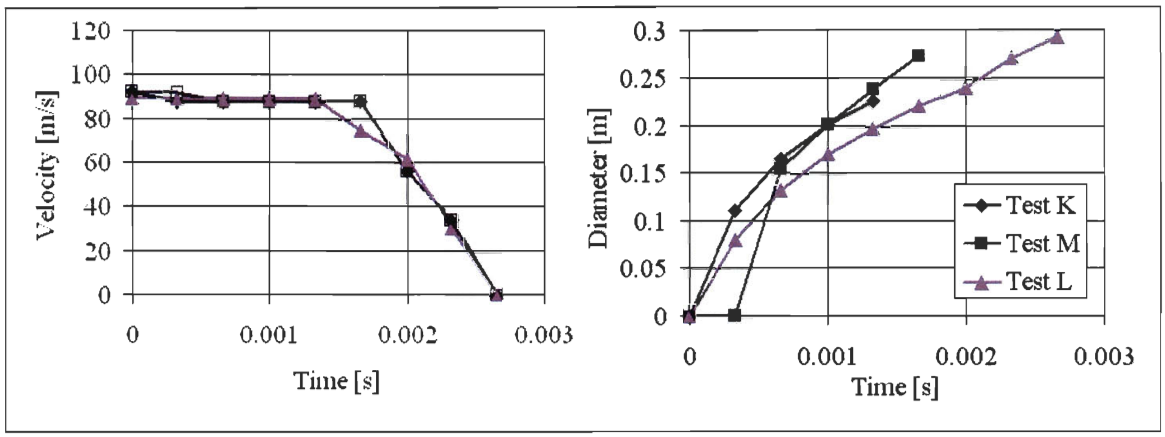

Figure 2.14 Variation of velocity(left) and diameter (right) of the projectile at 30° angle

2.3.2 Pressure

The pressure through the impact is the second criteria used to analyze the behaviour of the bird. The general shape of the curves is in good agreement with the theory where a sharp rise in pressure occurs at the initial impact and then stabilizes to a steady state value half-way through the impact process.

The duration is generally 15-20% longer than that expected. The expected duration is of 0.002 ms and it corresponds to the time it takes for the bird to travel its length. However the video camera showed no increase in the length of the bird. An alternate explanation resides in the fact that the bird slows down during the impact which could explain the longer duration.

In the perpendicular impact, given on the left of Figure 2.15, gage #3 is impacted first since it is in the middle of the target and the bird has a round tip. Gages #1 & #2 and #4 & #5 agree very well together, proving the impact was orthogonal and axisymmetric.

As for the impact at 30°, the pressures are shown in the right of Figure 2.15. The target is inclined in such a way that gages #4 and #5, which are at 1 in from the center, are forward with respect to the other gages, which is why their pressure is almost simultaneous and slightly higher than gage #3. It is possible to observe that once again the steady state pressure is quite higher than the nominal value for this velocity.

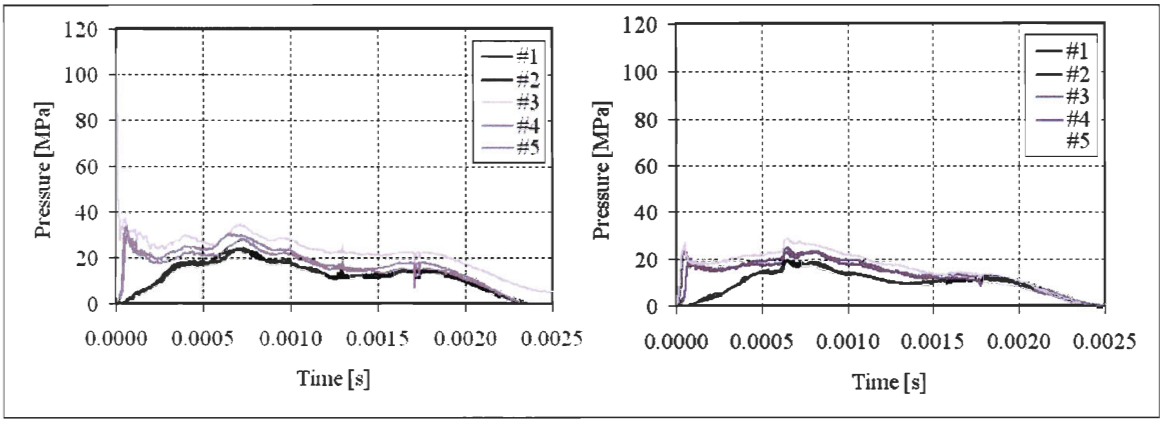

Figure 2.15 Pressure reading for the tests, test at 0° (left) and 30° (right)

The main concern with the results presented in Figure 2.15 is the amplitude of the signal. Theoretically, the maximum peak pressure for gage #3 should be of 70 MPa and the steady state pressure for the same gage should be of 4.7 MPa. The theoretical values are calculated for water with a porosity of 10% [37]. In practice, gelatine with a 10% porosity was used. The porosity of the medium is approximated by comparing its known density and the density obtained after mixing air into it. The density for the porous water or gelatine is the same, and allowance could be made for a relatively small difference. However, the peak pressure and the steady state pressure are much higher than the theoretical values.

Another way to look at the pressure data is to analyze the steady state pressures since they represent the bulk of the impact and energy transferred to the target. A theoretical approach found in Wilbeck [1] is used to calculate the radial steady state pressure distribution for the perpendicular impact. The normalized theoretical values are both plotted in Figure 2.16.

The pressure is first normalized with respect to the theoretical steady state pressure. As stated previously, the amplitude of the signal seems to be inaccurate. Hence, the tests' values were corrected by normalizing with respect to the center gage's steady state pressure instead of the theoretical steady state pressure, which yields ratio much closer to the predicted values. Therefore, even if the magnitude of the pressure is very large, the radial distribution of the steady state pressure agrees with the theory found in [37].

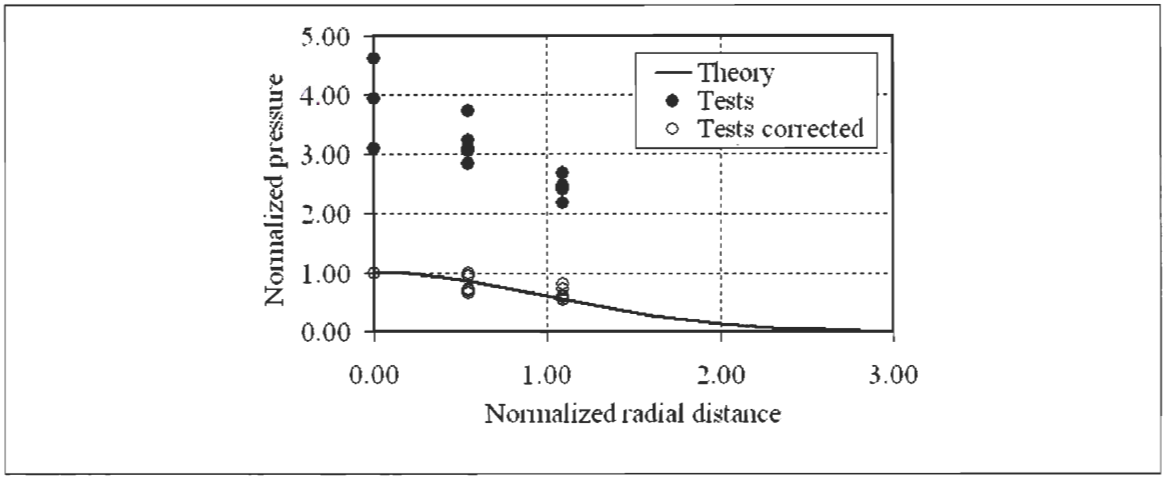

Figure 2.16 Normalized steady state pressures

It is possible to quantify an amplification factor from Figure 2.16. In general, the values are 3 to 4.5 times larger than expected. Many efforts have been put into identifying the cause of this amplification factor but with limited success.

Now, the question remains to know whether the data or the acquisition method is not accurate enough. A tentative to answer this question is addressed by calculating an approximation of the energy transferred to the target.

2.3.3 Energy level

It is possible to show that the pressure is too high in an unphysical manner by calculating the energy involved. Before the impact, all the energy in the system is contained in the kinetic energy of the bird, which is equal to $\frac{1}{2}mv^2$. Hence, the maximum amount of energy that can be absorbed by the plate is 4500 J.

The energy absorbed by the plate can be coarsely approximated by the pressure readings. The first assumption is that the pressure is distributed linearly and decrease from its maximum value at the center to zero at the bird radius. A second assumption is that the velocity creating the force, or pressure, is the same as the velocity of the end of the bird, which is given in Section 2.3.1. Therefore, the energy can be approximated as follow:

$$E = \int F\,v\,dt = \int PAv\,dt = \int\left[\int\int P(r)rdrd\theta\right]v\,dt = \int\left(\int_0^{2\pi}\int_0^{R} P_{gage\#3}\left(1-\frac{r}{R}\right)rdrd\theta\right)v\,dt$$
$$= \int\frac{\pi}{3}R^2 P_{gage\#3}\,v\,dt \approx \frac{\pi}{3}R^2\sum\left(\frac{P_{gage\#3,n}+P_{gage\#3,n-1}}{2}\right)\left(\frac{v_n+v_{n-1}}{2}\right)\left(t_n-t_{n-1}\right) \quad (2.3)$$

The approximation is applied to the perpendicular impact to calculate the energy for those tests. As showed by Table 2.2, the approximation is much higher than the physically possible value.

Table 2.2 Energy absorbed by the target

Test	Theory	Test 1	Test 2	Test 3
Energy [J]	4500	8500	12000	11000

If the pressure recorded was correct, one would expect that the energy transferred to the target to be less than the initial kinetic energy of the projectile. However, the values given in Table 2.2 are much higher than the initial energy, which is physically impossible. Hence, it is proven that the pressure reading is incorrect. However, because the shape and duration of the pressure curves agree with the theory, the problem appears to be a general amplification of the signal rather than an incorrect understanding of the theory of the bird impact.

2.3.4 Discussion

The main outcome of the data analysis is that the behaviour of the carbon gage is not as well understood as first believed. In the past, the gages have been successfully used in tests at DRDC where a rubber projectile impacted on the gage. However, this type of impact is very punctual in time and the projectile is not destroyed by the impact. In the case at hand, the event has a much longer duration where a steady flow condition is developed.

Moreover, the intended purpose of a carbon gage is to measure the stress normal to the direction of shock wave propagation. However, piezoresistive materials like carbon are also sensitive to straining effects. Hence, if perpendicular strain conditions are not maintained during the measurement, the sensor responds to both *stress* and *strain* along the gage plane, thus introducing errors in the reading.

The choice of the carbon gages was made according to the recommendations of the manufacturer [38]. After considering the results obtained, it becomes obvious that those recommendations were not accurate. Additionally, the manufacturer also admitted that in spite of recommending the use of a protective layer of Lexan (or other material), the overall effect was unknown with respect to the calibration curve provided. Because the amount of unknown, it might be necessary to conduct new tests where the applied load is known so that new calibration curves could be plotted.

Another explanation is a mechanical amplification of the signal at low frequency. It can lead to many interpretations, but one observation to which it can be related is that during the tests, the support bended backward. This however was not measured and is very difficult to assess. A general appreciation of the event is given in Figure 2.17 where the white vertical line shows the edge of the target, hence underlining the movement of the target and its support. In view of the bending of the support, it is easy to understand why other research projects have used much bigger support for their targets [4,16]. The difference in size and bulkiness with respect to the support used for the tests discussed is significant.

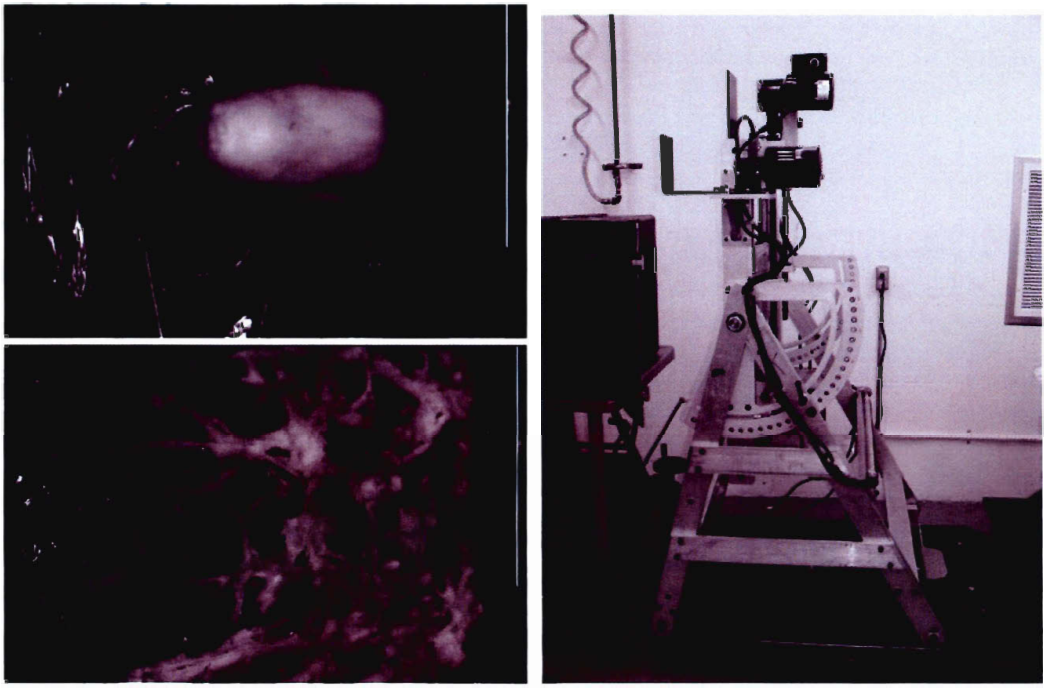

Figure 2.17 Movement of the target's support (left) & support (right)

Moreover, given that the acquisition system was sensitive to the lights in the room which were on a different electrical circuit, it is possible, although difficult to assess, that the movement of the target influenced the pressure readings.

All this is to say that the sources of error are numerous and the work involved in identifying and eliminating them is extensive. In future work, it might be wise to investigate a different approach to measure the pressure.

2.4 Comparison with numerical models

The numerical simulations were conducted using the ALE (arbitrary Lagrangian-Euler) and SPH (smoothed particles hydrodynamics) methods to represent the 1 kg bird. Both methods are used in order to show the strengths and weaknesses of each. Theory for both methods is provided in LS-DYNA Theory manual [32], but additional information can be found in Souli [39] for the ALE methods, and in Liu [42] for the SPH method. The initial parameters of the elastic-plastic hydrodynamic material model used are the same as those given in Section 1.4. The parameters for the interaction with ALE have been adjusted as to have a positive pressure at all time and still respect the theoretical peak and stagnation pressure.

As for the equation of state, a polynomial equation has been used. It is an equation frequently used in the literature [13,17,27] and comparison with the numerical results obtained using a Mie-Gruneisen equation showed very little differences.

The target is 1.3 cm [½ in] thick and 30.5 cm×30.5 cm [12 in×12 in] side dimension. An edge 1.3 cm [½ in] wide and 0.6 cm [¼ in] thick is also modelled in order to represent the frame of the support which maintains the target in place. An elasto-plastic material model with the properties of RHA steel is used to represent the target. In order to represent the experimental set-up properly, the edge of the plate is fixed and the mesh size in the zone of impact is the same as the size of each individual carbon gage (0.5 cm×0.6 cm [0.20 in× 0.25in]). Both numerical models are shown in Figures 2.18 and 2.19 for the perpendicular and inclined target, respectively.

The velocity of the bird has been set to an average value of 95 m/s and the simulations run for 0.005 s in order to capture the dispersion of the bird debris.

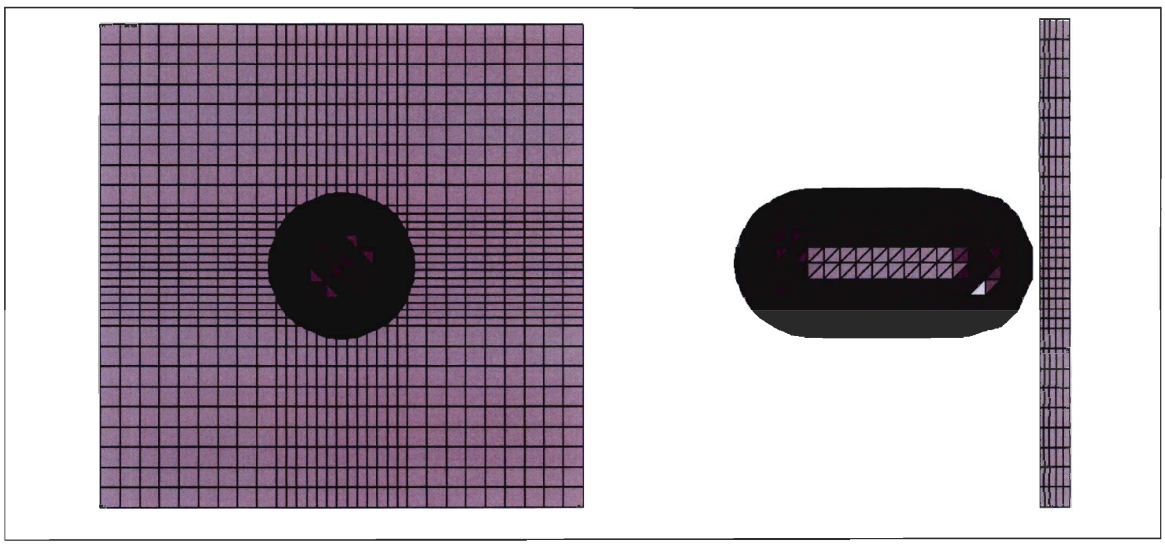

Figure 2.18 Front and side view of the ALE numerical model for the 0° impact

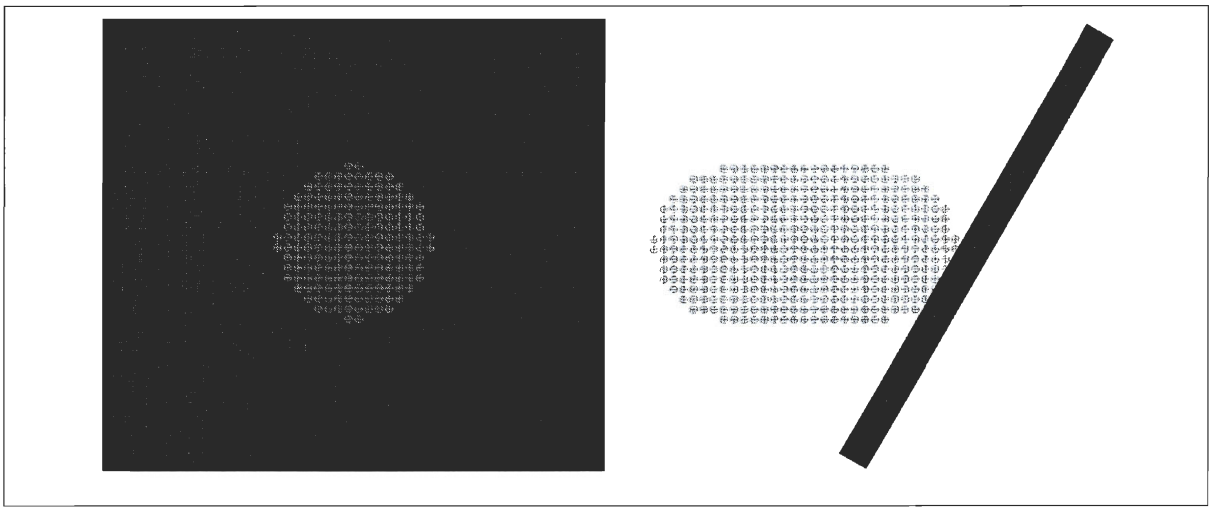

Figure 2.19 Front and side view of the SPH numerical model for the 30° impact

2.4.1 Bird's deformations

The deformations of the bird are first analyzed. The shape change of the bird during the impact at 0° is shown in Figure 2.20 and the same for the impact at 30° is shown in Figure 2.21. The snap shots are taken at time intervals of about 0.66 ms and with the purpose of showing the shape change through the impact.

There is a good agreement between the experimental test and simulations results at this level. The behaviour of the gelatine bird is well represented by the numerical models. The duration of the experimental event is consistent with what was observed numerically. Visually, the ALE method seemed to have more difficulties following the deformations properly towards the end of the impact. This is particularly obvious with the impact at 30° where the bird loses 25% of its mass. The mass loss is due to the minimal fraction of dense matter required within an element for it to be included in the numerical calculation. So far, it represents a minor inconvenient, but for more complex geometries, it could represent a significant shortcoming of the ALE method. On the other hand, the SPH method has no difficulty preserving the mass of the projectile throughout the simulations since the mass is carried at each of the particles. It was also noted that for both numerical methods, it was important to include the edge of the clamping device in numerical model to accurately represent the dispersion of the debris.

The behaviour of the projectile during the impact event can also be evaluated by measuring the velocity of the end of the bird and its diameter on the plate. The results for the 0° impact are shown in Figure 2.22 and the results for the 30° impact are shown in Figure 2.23. Note that the precision of the experimental data is very coarse. Nevertheless, it is sufficient to observe that the evolution of the diameter is within the range given by the experimental data. As for the velocity, the deceleration and the time at which it begins during the impact are consistent between the experimental data and the numerical simulations.

The good correlation between the experimental data and the simulations also confirms that the properties used for the bird in the numerical simulations are appropriate.

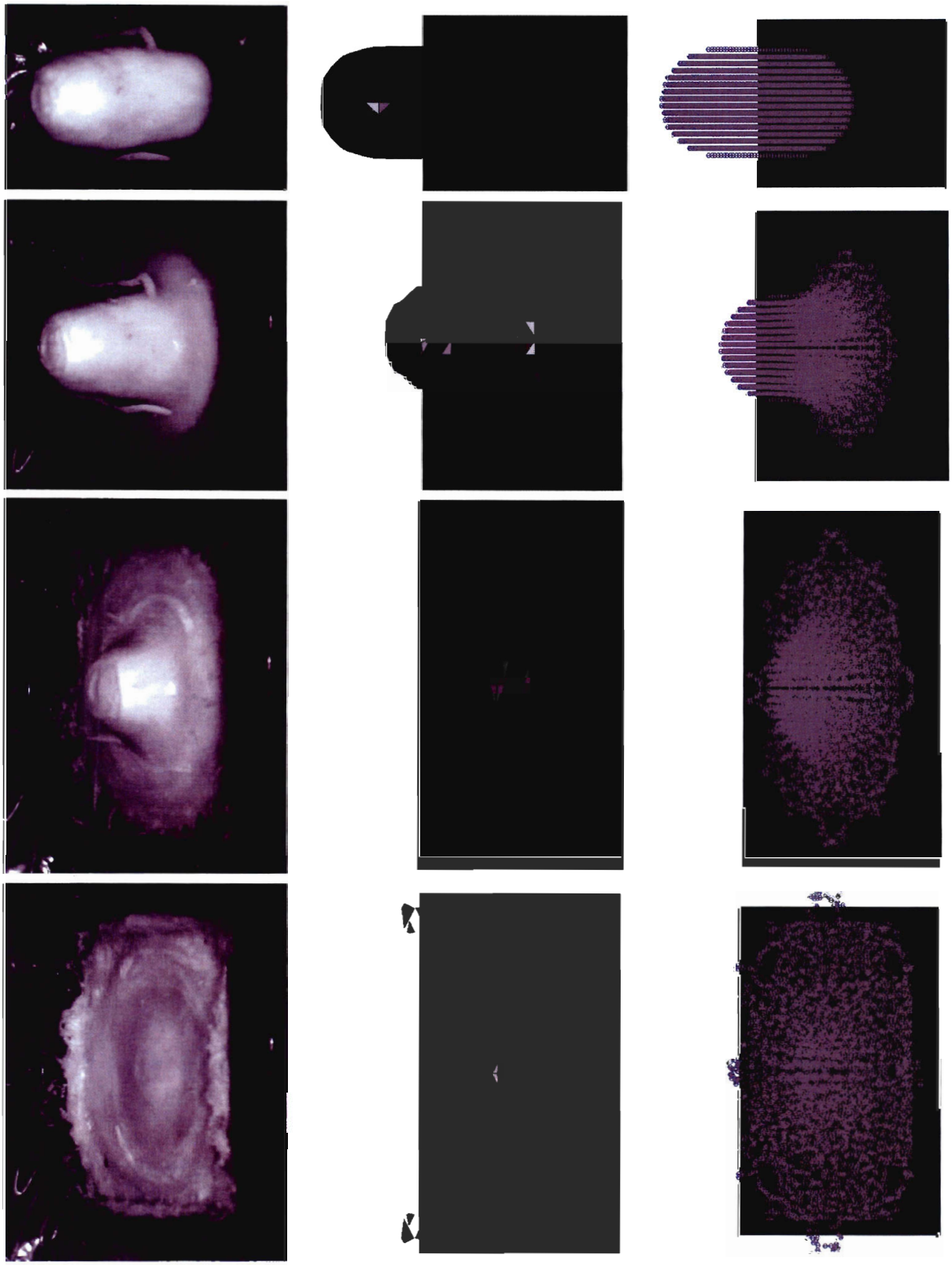

Figure 2.20 Impact at 0° after 0.66 ms, (a) video, (b) ALE method, and (c) SPH method

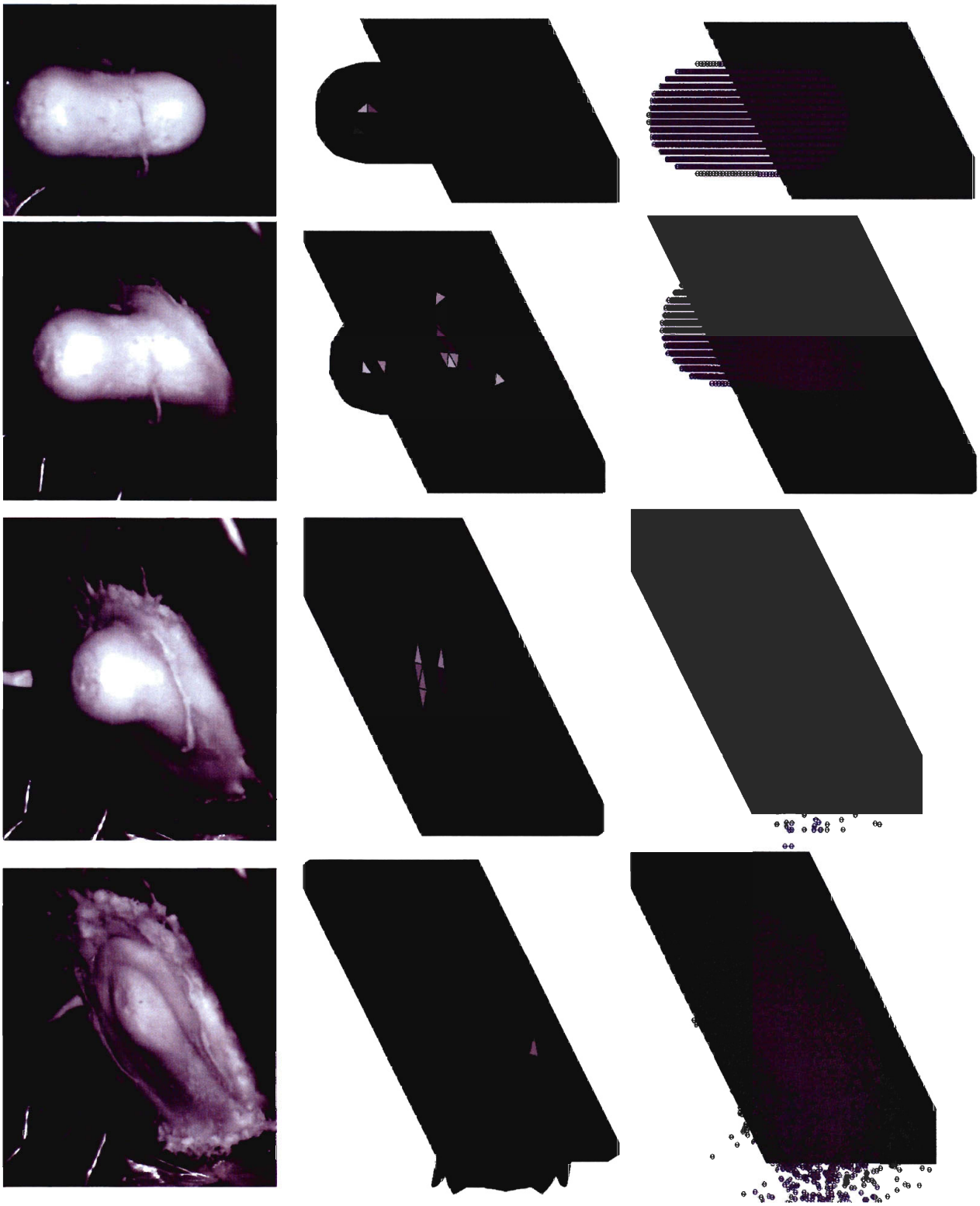

Figure 2.21 **Impact at 30° after 0.66 ms, (a) video, (b) ALE method, and (c) SPH method**

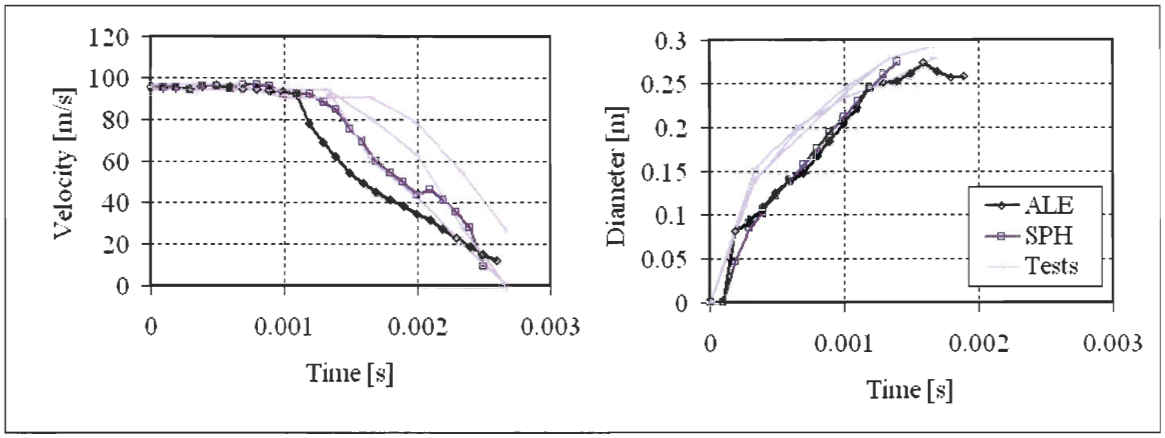

Figure 2.22 Variation of velocity (left) and diameter (right) of the projectile at 0° angle

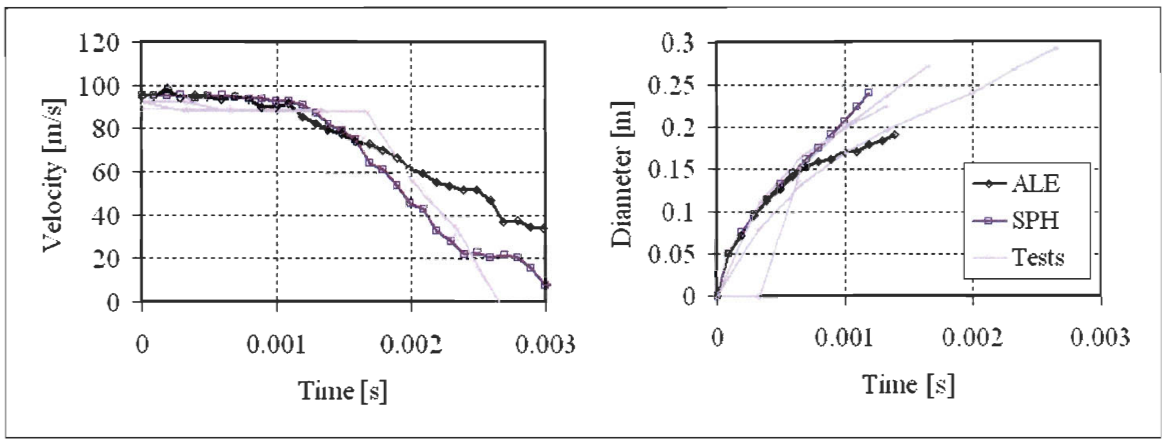

Figure 2.23 Variation of velocity (left) and diameter (right) of the projectile at 30° angle

2.4.2 Pressure reading

The pressure displays the same trends as the experimental results, but now on a scale which agrees with the theory. The pressures from the ALE simulations are shown in Figure 2.24 and for the SPH simulations, the pressures are shown in Figure 2.25. The SPH remains spurious in nature, which is a typical downfall of this approach. The results at 30° are also consistent with what was expected. The duration of the impact is slightly longer than the expected duration, given by the length/velocity ratio, which can be related to the fact that the projectile slows down during the impact. This supports the fact that the durations for the experimental data are longer than predicted by the theory.

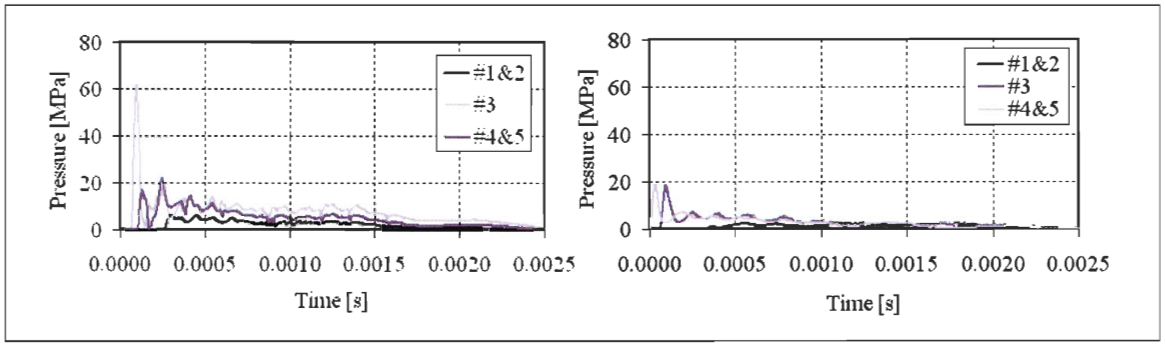

Figure 2.24 Pressure readings for ALE model, angle 0°(left) & 30°(right)

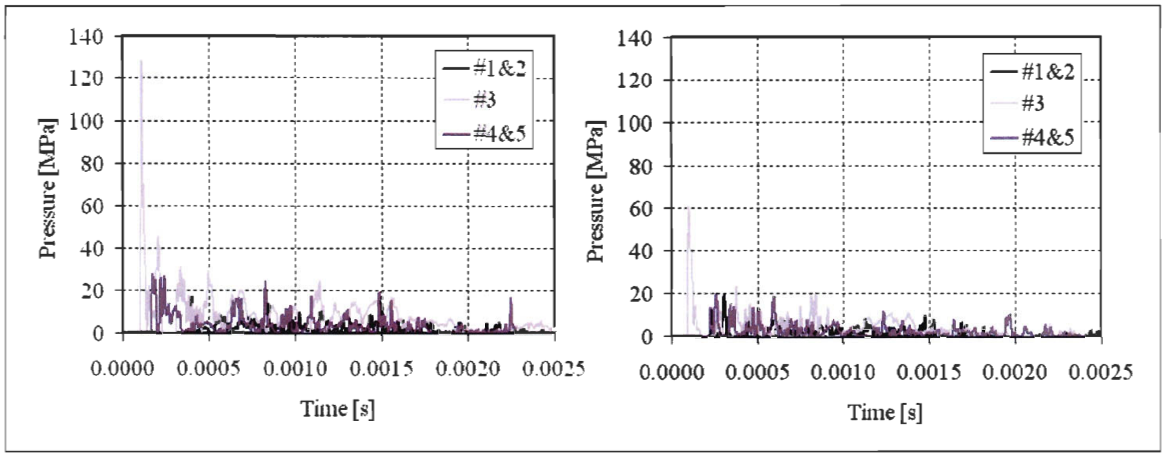

Figure 2.25 Pressure readings for SPH model, angle 0°(left) & 30°(right)

Now, the radial steady state pressure distribution for the numerical simulations is plotted in Figure 2.26 together with the corrected tests values. A general good agreement can be observed between the theory, the numerical results and the corrected experimental results.

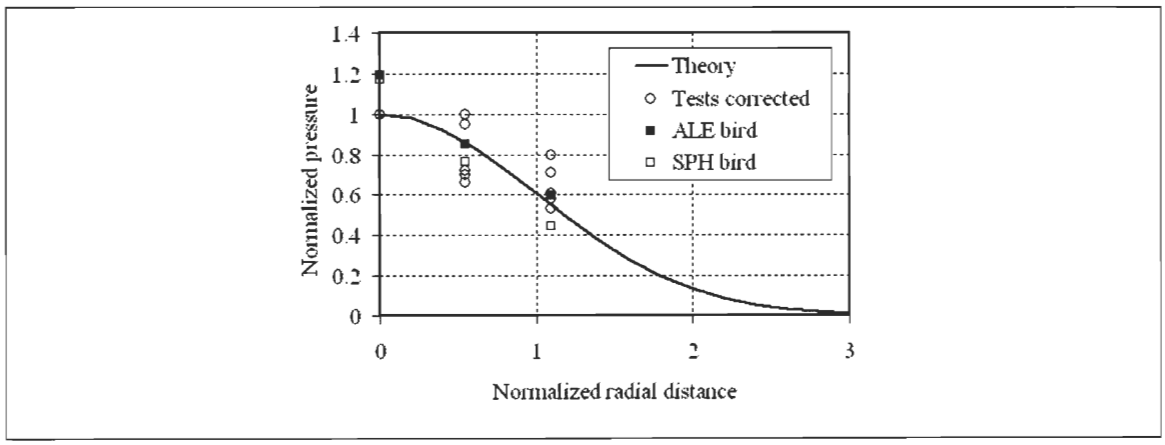

Figure 2.26 Radial distribution of pressure

2.4.3 Energy level

The energy absorbed by the target was calculated in the same manner as for the experimental data, using the center gage. The results are compiled in Table 2.3 and show that for the numerical simulations, the total energy in the system is lower than the initial kinetic energy, which is physically acceptable. Interestingly enough, the energy for the SPH method is very close to the energy for the ALE method. Therefore, although ALE displays a more stable reading for the pressure, the energy transfer between the bird and the target is similar.

Table 2.3 Calculated amount of energy absorbed by the plate for numerical simulations

Test	Theory	Average for tests	ALE	SPH
Energy [J]	4500	10500	3400	3700

2.4.4 Comments

The deformations of the numerical birds compare well with the experimental results. On the other hand, the pressure, radial pressure and energy agree with theory better than tests themselves. Overall, the SPH approach seems to model the deformations slightly better than ALE, but on the other hand ALE models the pressure better. As for the energy, the results from ALE and SPH are comparable. Hence, both numerical models are quite acceptable. The suitability of each one may depend more on the application itself.

2.5 Conclusions

So far, it has been possible to develop a recipe for the gelatine bird, which works well and can be made in small quantities using simple equipment. This should be useful in assessing standards for bird test certification procedure.

The deformations of the bird's substitute during the impact was well captured by the video camera and it was shown that it does behave as a fluid and that using a gelatine mixture with lower density rather than pure gelatine affects the deformations. Moreover, the numerical tools offered good correlations to the experimental data in this area.

It was also proven that the trends displayed by the pressure agree well with the theory and that the corrected normalized radial pressure distribution is good. The pressure values themselves are not reliable since the energy transferred is much greater than the initial energy. On the other hand, the pressures obtain from the numerical models agree well with the theory and yield an acceptable energy level. Hence, even if it is not possible to validate the numerical models using the experimental data, the reliability of the numerical models is demonstrated.

If carbon gages were to be used in future work, a calibration of the gages once they are bonded to a steel plate and a protective layer of Lexan might be necessary in order to have more accurate equations to convert the voltage into pressure. A thorough analysis of the target's support and its natural frequency would also be necessary to make sure that vibration within the target are not picked-up by the gages. Moreover, although the support didn't move with respect to its anchorage point, it was flexible and bended during the impact. It might thus be necessary to design an entirely new support for the target.

Therefore, although it hasn't been possible to directly validate the pressure generated by a bird impacting on a rigid target, it is fair to say that the numerical bird models available today generate good results based on the deformations of the bird during the impact and a better agreement between the numerical approach and the theory than the experimental data and the theory.

Future work should involve an investigation of alternate ways of measuring the pressure with less error, such as pressure transducers or load cells, the use of a new target's support, and different velocities and sizes for the projectile.

PART B – Summary of the Improved SPH Method

The improvement of the SPH method is threefold: first the formulation needed to be reviewed and improved so that it would be more robust. This is done by developing the equations based on the energy conservation principle. Second, four additional material models are given so that the SPH method can treat a wider range of problems. Finally, a few approaches to the fluid structure interaction, or contact, are given to widen the scope of application of the method.

The first aspect is thoroughly presented in Chapter 3 which has been submitted for publication as an article entitled *Variable-h and Energy Based SPH Formulation with Corrections* to the journal Computational Mechanics in January 2008. It gives the state-of-the-art of the SPH method and the details of the equations used for the energy conservative SPH formulation with the corrections applied. The authors of the paper are Marie-Anne Lavoie and Augustin Gakwaya, from Université Laval, and Manouchehr Nejad Ensan, from the National Research Council. The abstract and keywords of the paper are given below in English and French.

This paper presents an improvement of an existing SPH algorithm. The new formulation was developed based on the energy conservation equation. Moreover, since the smoothing length is variable, it was treated as such in the approximation. A boundary correction function was applied to address the boundary inconsistency issue. The obtained results were compared with normalization of the kernel function and its gradient. The resulting formulation was applied to the shear cavity and dam collapse problems with success.

Keywords: SPH formulation, variable smoothing length, energy conservation, three-dimensional boundary correction function, normalization

Cet article présente des améliorations apportées à un algorithme SPH existant. La formulation présentée est développée à partir des équations de conservation d'énergie. De plus, étant donné que la taille du domaine d'approximation est variable, ce paramètre est traité comme tel dans l'approximation. Une fonction de

correction de la frontière est appliquée afin de traiter le problème d'inconsistance à la frontière. Les résultats obtenus sont comparés à la normalisation de la fonction de pondération et son gradient. La formulation qui en résulte est appliquée aux exemples de cavité sous cisaillement et d'effondrement de barrage avec succès.

Mots clefs : formulation SPH, taille du domaine d'approximation variable, conservation d'énergie, fonction de correction de la frontière tridimensionnelle, normalisation

The second aspect is studied in Chapter 4 and includes four additional material models, namely the elastic, elastic-plastic, Johnson-Cook, and elastic-plastic-hydrodynamic material models. Sample problems are given to demonstrate the level of accuracy that can be expected and demonstrate that the SPH algorithm works well for materials other than fluids. Finally, two additional interaction algorithms: the contact potential and the node to node contact are given in Chapter 5 and some examples previously given are revisited to show the gain in accuracy and advantages of the additional boundary interaction method presented.

3 Variable-*h* and Energy Based SPH Formulation with Corrections

3.1 Introduction

The smooth particle hydrodynamics (SPH) method is one of several meshless approaches. It was developed in the late 70's and early 80's by Lucy and Monaghan [40,41] and was initially applied to hypervelocity impacts occurring in outer space. *Smooth* represents the approximation nature of the weighted average over the neighbouring *particles* and *hydrodynamics* refers to the scope of problems to which it is applied. It is the oldest meshless method and is approaching its mature stage. Hence, it is the meshless method that is generally implemented in commercial finite element software [42].

In addition to its original application to hypervelocity impact in outer space, SPH has been applied to a variety of problems such as fluid flows [43,44], underwater explosions [45], metal forming [46], impact on metallic targets [47,48], concrete fragmentation [49], debris flow and avalanches [50]. Different applications encounter different initial and boundary conditions and different numerical difficulties. For instance, boundary conditions can be neglected with little consequence for free surface flow but are important when a target is modelled with SPH particles. Moreover, while artificial viscosity improves the results of hypervelocity impact, it is a necessity to obtain credible results for metal forming and other similar situations. In general, those difficulties are classified into four categories.

The first shortcoming is a tensile instability which can lead to numerical fracture. This is caused by a non-physical value in the tensile stress state caused by the interaction between the constitutive model and the kernel function [51,52]. It results in an unstable clustering of the particles which is not representative of the physics of the event. It is usually prevented by adding an artificial viscosity term to the pressure for which several formulations have been developed [41,42,53,54]. Another alternative is to use a Lagrangian kernel where the kernel is a function of the material coordinates [55,56] instead of the usual Eulerian kernel. On the other hand, using a Lagrangian kernel does not solve the tensile instability due to rank deficiency observed with the Eulerian kernel. This instability requires the use of two

different set of points (standard SPH material points for motion evolution and stress points where stress and strain are calculated) in order to be eliminated [55,56,57,58,59,75]. It is important to note that both the use of Lagrangian kernels or stress points lead to meshless methods that are not the standard SPH method.

The second issue is a lack of interpolation consistency or completeness. It is due to the fact that SPH is an interpolation among moving particles and not a partition of unity, which means that SPH interpolants cannot represent rigid body motion correctly [52,60]. This result in instability that is very similar to tensile instability and often, the two are treated together. Liu *et al* [61] were the first to notice the problem and set forth the concepts of 'correction function'. The basic idea of corrective SPH is to construct a corrective kernel as a product of the correction function with the original kernel. The new interpolant is often named the reproducing kernel particle method (RKPM) [61]. Different levels of consistency are achieved by applying the Taylor expansion for continuous functions, and the consistency, or completeness, of the SPH interpolation can thus be enforced. However, using a RKPM or a moving-least-square (MLS) interpolation [62,63] to construct the kernel may not be cost-effective since additional CPU is required to search, update the connectivity array, and calculate the modified kernel function. The several compromises proposed throughout the years can be summarized as follows (*i*) the Monaghan's symmetrisation on derivative approximation [64,72] and used in Liu [42]; (*ii*) the normalized smoothing method proposed by Johnson and Beissel [65] to obtain linear consistency; (*iii*) the Randles-Libersky correction which uses a normalization with stress points [75]; (*iv*)the Krongauz-Belytschko correction [66] which is an improvement of the element-free Galerkin (EFG) method using a MLS approach; (*v*) the Chen-Beraun SPH correction [67,68,69] which uses a kernel corrected with the Taylor series expansion; (*vi*) and the Bonet-Kulasegaram [46,50,70,86] corrected SPH formulation with kernel correction based on RKPM [61].

Another avenue to address the interpolation consistency is to use a time-variable smoothing length [47,51,56,59,60,70,71]. However, a varying smoothing length means that it can be different for each particle and it is possible that a particle *a* influences a particle *b* while the opposite may not be true. This is a direct violation of Newton's third principle where there

should be a reaction to every action. Hence, an average smoothing length between a and b is generally used in order to preserve the symmetry of the particles' interaction.

The third main short coming is the presence of zero-energy modes. The reason that SPH suffers zero-energy mode deficiency is due to the fact that the derivatives of kinematical variables are evaluated at particle points by analytical differentiation rather than by differentiation of interpolants. In many cases, the kernel function reaches a maximum at its nodal position, and its spatial derivatives become zero. In the literature, two types of solutions are used: the dissipation of spurious modes or an alternative discretization that does not evaluate the variables and their derivatives at the same points. Dissipation can be done by applying a symmetrisation [72] or a normalization to the kernel, its gradient, or both [46,73,75]. The other solution is to use an alternative discretization such as the EFG method [56,74], the collocation approach [57], or the stress point approach [48,75] where different sets of particles are used to interpolate different fields variables. Here, because the alternative discretization is meant for high distortion cases rather than fragmentation or fluid flow and to optimize the computational efficiency, only particles are used to carry the information.

Finally, the boundary conditions are generally ignored. In many cases, this does not affect the results significantly. However, the appropriate treatment of boundary conditions becomes more important when dealing with impacts or interactions with meshed structures. One possible treatment of boundary conditions, which is particularly efficient in the case of free surface flow, is to fix the particles that are on the boundary or to use mirror particles outside the boundary which are updated at every time step [59,75,76,77]. Another option is to use mirror particles, especially in the case of symmetrical problems. Overall, using virtual boundary particles works well, but it requires that the entire problem is modelled with SPH particles. To extend the application of SPH, Müller [78] suggested using ghost particles that are created every step and attached to the finite mesh and interact with the SPH particles to model the boundary where an impact would take place. An aspect which is generally overlooked is the fact that the integration domain at the boundary is incomplete when approaching a boundary. Bonet and Kulasegaram [60, 79] have developed and implemented a boundary correction function for two-dimensional problems with rigid

boundaries. However, it is desirable to extend the boundary correction function to three dimensional cases with deformable boundaries. The equations used to simulate the boundary forces are also of importance, especially for SPH simulation of impact and fragmentation. The contact equations are revisited by Campbell *et al* [80,81] and Seo and Min [94] and adapted to the SPH formulation.

This paper is motivated by the fact that for SPH to realize its full potential as a computational method for continuum solid dynamics, it must be put on sound footing with respect to some severe problems revealed by a closer examination. Major difficulties have been identified and some are still open research issues: the tensile instability threatens the usefulness of SPH to do the kinds of problems for which it seems best suited, i.e., fracture and fragmentation; however recent works based on updated Lagrangian formulation indicate that such issue is being brought under control, the gradient estimate that is less accurate than other techniques for non-uniform or random particle arrangements has been addressed using different corrected SPH formulations but computationally efficient algorithms are still needed; the lack of generalized boundary conditions and the interface problem which produces spurious oscillations at material boundaries with disparate densities are however not yet satisfactory addressed. More is still to be done before achieving such long term objectives, and the aims of the current research are to contribute to the improvement of existing SPH algorithms, especially those developed by G. R. Liu [42]. The algorithm is initially improved so as to address the tensile instability issue by developing the new SPH formulation from the variational principles, or energy methods. It does not eliminate the tensile instability for a full range of application, but it makes the formulation more stable. Moreover, in order to address the lack of completeness and interpolation consistency, corrected kernel have been implemented and the smoothing length h, which is a variable, is treated as such in the calculation of the gradient of the kernel function. In addition, the fluid-structure interaction of the SPH method is improved by restoring consistency at the boundary according to recent work of Bonet [60] and Kulasegaram [79]. This method was applied to three-dimensional problems with flexible boundaries. The results obtained from the application of boundary correction function are compared to the results obtained with normalization since both corrections have a similar approach.

This paper is organized as follow: the fundamentals of smooth particle hydrodynamics approximation for a general field variable are reviewed in Section 3.2. Section 3.3 gives a detailed description of the gradient of the kernel function and the effect of considering smoothing length h as a variable. The equations for the mass and momentum conservation are developed in Section 3.4. Section 3.5 summarizes some general additional concepts used to run the program. In section 6 the developed algorithm has been applied to study the shear cavity and dam collapse problems which demonstrates the strengths of the new SPH formulation presented in this research work.

3.2 Fundamentals of SPH Function Approximation

Meshless methods convert the continuous model of a physical system, which are usually represented with partial differential equations, into discretized forms in order to solve the problem numerically. This procedure, referred to as discretization, often have significant effects on computational efficiency and accuracy. However, unlike traditional finite element methods where the construction of the basis functions relies on the mesh structure, the basis functions for the majority of meshless methods are independent of the meshes. Because of this, the meshless methods are able to overcome the limitations due to the mesh.

Two fundamental concepts govern the formalism of smoothed particle hydrodynamics SPH. The first basic idea is that any observable or measurable field variable is smoothed over the spatial domain by using appropriate smoothing kernels. The second assumption is that a continuum can be assimilated to an identifiable set of discrete interacting entities named particles. Hence, before applying the SPH approximation to the conservation equations of continuum mechanics, it is important to understand how the approximation is developed. A function f can be approximated over a domain Ω using the Dirac delta function δ as follow:

$$f(\vec{x}_i) = \int_{\Omega} f(\vec{x}_j)\delta(\vec{x}_i - \vec{x}_j)d\vec{x}_j \qquad (3.1)$$

where x_i is the position of a particle and x_j the position of its neighbour. Its approximation with a kernel function, also called a reproducing kernel [45,46], $W(\vec{x}_i - \vec{x}_j, h_i)$ can be defined as:

$$\langle f(\vec{x}_i)\rangle = \int_{\Omega} f(x_j) W(\vec{x}_i - \vec{x}_j, h_i) d\vec{x}_j \qquad (3.2)$$

The kernel is positive and compact and will provide an approximation of the function at a given point based on the contribution of surrounding particles. The kernel approximation of the reproduced function $\langle f(\vec{x}_i)\rangle$ will converge to the exact function as $W(\vec{x}_i - \vec{x}_j, h_i)$ approaches the Dirac delta function. The smoothing length, h_j, defines the size of the influence domain and W depends on the relative distance between two particles written as $\vec{x}_i - \vec{x}_j$ and of the parameter h_i. Only the particles near the evaluation point contribute to the kernel. In general, the kernel function has to satisfy as number of conditions. First, the kernel must be equal or greater than zero over the domain:

$$W(\vec{x}_i - \vec{x}_j, h_i) \geq 0 \qquad (3.3)$$

The kernel must also be able to exactly approximate constant functions:

$$\int_{\Omega} 1 \cdot (\vec{x}_i - \vec{x}_j, h_i) d\vec{x}_j = 1 \qquad (3.4)$$

and is said to be of zero order consistency if it satisfies:

$$\int_{\Omega} 1 \cdot \nabla W(\vec{x}_i - \vec{x}_j, h_i) d\vec{x}_j = 0 \qquad (3.5)$$

Moreover, since the kernel only approximates the delta function, then in general $\langle f(\vec{x}_i)\rangle \neq f(\vec{x}_i)$ and hence $\langle f(x)\rangle = f(x) + E(f, x)$ where $E(f, \vec{x}_i)$ is the approximation error of f at point $\vec{x}_i$. Hence, to ensure that $\langle f(\vec{x}_i)\rangle \to f(\vec{x}_i)$ as $h_i \to 0$ the kernel function should satisfy:

$$W(\vec{x}_i - \vec{x}_j, h_i) \to \delta(\vec{x}_i - \vec{x}_j) \text{ as } h_i \to 0 \qquad (3.6)$$

The last property comes from the requirement that the smoothing kernel must be differentiable at least once

$$W\left(\vec{x}_i - \vec{x}_j, h_i\right) \in C^m(\Omega) \text{ for } m \geq 1 \tag{3.7}$$

This is because the derivative of the kernel function should be continuous to prevent a large fluctuation in the force felt by the particle. The kernel function W can thus be easily designed so that the approximation $\langle f(\vec{x}_i)\rangle$ is exact for polynomials up to order m, that is $\langle f(\vec{x}_i)\rangle = f(\vec{x}_i)$ for any polynomial of degree less or equal to m. In that case, the approximation is said to have a reproducibility of order m. Equivalently, some authors refer to this property as consistency or completeness condition of order m.

A very common kernel function, which satisfies the aforementioned conditions, is the cubic spline defined as [45]:

$$W\left(R_{ij}, h_i\right) = \alpha_{dm} \times \begin{cases} \frac{2}{3} - R_{ij}^2 + \frac{1}{2} R_{ij}^3 & 0 \leq R_{ij} < 1 \\ \frac{1}{6}\left(2 - R_{ij}\right)^3 & 1 \leq R_{ij} < 2, \text{ where } R_{ij} = \dfrac{r_{ij}}{h_i} \\ 0 & R_{ij} \geq 2 \end{cases} \tag{3.8}$$

where α is equal to $1/h, 15/17\pi h^2, 3/2\pi h^3$, in one, two, and three dimensions respectively; it represents a scaling function which depends on the dimensions of the problem and that will ensure that the zero order consistency conditions are satisfied inside the domain. A plot of the cubic kernel function is given in Figure 3.1 where R_{ij} is the ratio of distance between the evaluation point and the surrounding particle and the smoothing length.

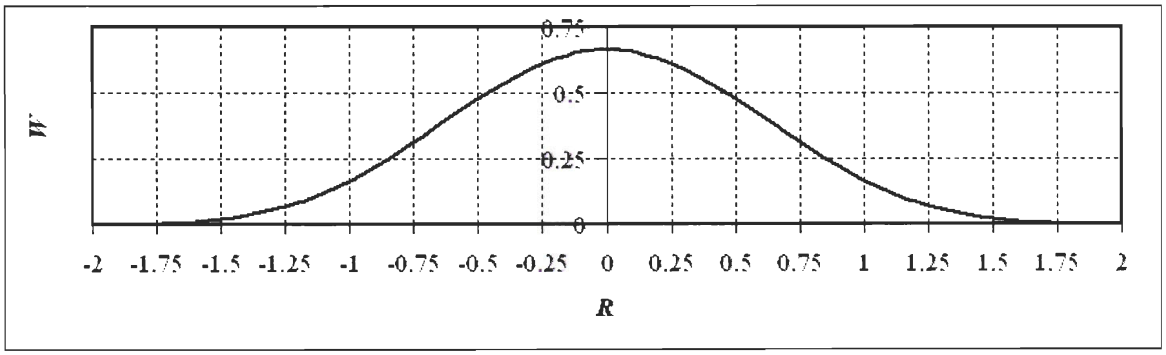

Figure 3.1 Cubic kernel function W

Given a domain Ω made of a set of points, usually called particles, the evaluation of the integration in equation (3.2) in a discrete manner lead to the following SPH approximation:

$$\begin{aligned} \langle f(\vec{x}_i)\rangle &= \int_{\Omega} f(\vec{x}_j) W(\vec{x}_i - \vec{x}_j, h_i) dx' \\ &\cong \sum_{j}^{N} f(\vec{x}_j) W(\vec{x}_i - \vec{x}_j, h_i) \Delta V_j \end{aligned} \tag{3.9}$$

Where the subscript *i* refers to the particle at which the function is evaluated, the subscript *j* refers to the *N* particles in the support domain, and ΔV_j is the volume associated to the particle *j*. The above equation (3.9) can be re-written in terms of standard shape functions as finite element method to give:

$$f(\vec{x}_i) = \sum N_j(\vec{x}_i) f(\vec{x}_j), \quad N_j = W(\vec{x}_i - \vec{x}_j, h_{ij}) V_j \tag{3.10}$$

where, unlike standard finite element approximations, the shape functions do not satisfy the condition of being 1 or 0 over the interpolation points. That is, $N_j(x_i) \neq \delta_{ij}$, and consequently $\langle f(x_i)\rangle \neq f(x_i)$. This inaccuracy leads to difficulties in enforcing essential boundary conditions.

Using $\Delta V_j = \frac{m_j}{\rho_j}$, the ratio of the mass and the density, the final form of the SPH particle approximation of *f* can be written as:

$$\langle f(\vec{x}_i)\rangle \cong \sum_{j}^{N} \frac{m_j}{\rho_j} f(\vec{x}_j) W(\vec{x}_i - \vec{x}_j, h_i) \tag{3.11}$$

It is now possible to proceed to the evaluation of the spatial derivative $\nabla f(\vec{x}_i)$, or the divergence of a field, by writing the kernel gradient as follows:

$$\langle \nabla f(\vec{x}_i)\rangle = -\int_{\Omega} f(\vec{x}_j) \cdot \nabla W(\vec{x}_i - \vec{x}_j, h_i) d\vec{x}_j \tag{3.12}$$

Now, applying the particle approximation of $f(\vec{x}_i)$ given by equation (3.11) above, the spatial derivative approximation becomes:

$$\langle \nabla f(\vec{x}_i) \rangle = -\sum_j^N \frac{m_j}{\rho_j} f(\vec{x}_j) \cdot \nabla_j W(\vec{x}_i - \vec{x}_j, h_i) \tag{3.13}$$

Moreover, since:

$$\nabla_j W(\vec{x}_i - \vec{x}_j, h_i) = -\nabla_i W(\vec{x}_i - \vec{x}_j, h_i) \tag{3.14}$$

Then:

$$\langle \nabla f(\vec{x}_i) \rangle = \sum_j \frac{m_j}{\rho_j} f(\vec{x}_j) \cdot \nabla_i W(\vec{x}_i - \vec{x}_j, h_i) \tag{3.15}$$

Note that in general the equivalent symmetrized forms of equation (3.15) are used to ensure that the computed gradient of a constant field f is zero, i.e. the zero order consistency condition is satisfied. These take the form:

$$\langle \nabla . f(\vec{x}_i) \rangle = \frac{1}{\rho_i} \sum_j m_j (f_i - f_j) \cdot \nabla_i W(\vec{x}_i - \vec{x}_j, h_i)$$

or (3.16)

$$\langle \nabla . f(\vec{x}_i) \rangle = \rho_i \sum_j m_j \left(\frac{f_i}{\rho_i^2} - \frac{f_j}{\rho_j^2} \right) \cdot \nabla_i W(\vec{x}_i - \vec{x}_j, h_i)$$

However the first order consistency, i.e. the exact evaluation of the gradient of a linear field, is not satisfied as one can show that on the boundary the kernel and its gradient do not respect equation (3.4) and (3.5). A boundary correction function γ is defined based on the following inequality:

$$\int_\Omega W(\vec{x}_i - \vec{x}_j, h_i) d\vec{x}_j = \gamma(\vec{x}_i - \vec{x}_j, h_i) \neq 1 \tag{3.17}$$

Since the integration domain is not complete near a boundary, the boundary correction function is defined. It depends on the distance from the boundary and the size of the influence domain, To evaluate it, the following identity is used:

$$\int_\Omega W(\vec{x}_i - \vec{x}_j, h_i) d\vec{x}_j \cong \sum_j W(\vec{x}_i - \vec{x}_j, h_i) V_i \tag{3.18}$$

Basically, the domain is divided in a number of equally spaced particles, each having a weight of V_i, corresponding to the dimension of the problem (i.e. length, area, or volume). The summation is computed for different distances from the boundary, that distance corresponding to y in equation (3.19). The boundary correction function found for all three dimensions is essentially the same, and a polynomial equation of degree 5 is fitted to the curve and is a function of the distance from the boundary and the smoothing length. The resulting suggested equation which is used in the work presented is:

$$\gamma(\varepsilon) = -0.0527\varepsilon^5 + 0.3026\varepsilon^4 - 0.5336\varepsilon^3 + 0.0558\varepsilon^2 + 0.6944\varepsilon + 0.5 \qquad (3.19)$$

where $\varepsilon = {}^{y}/_{h}$

Alternatively, Kulasegaram *et al* [79] used the following equation:

$$\gamma = 1 + (0.0625 - 0.0531\varepsilon)(\varepsilon - 2)^3 \qquad (3.20)$$

Figure 3.2 below shows the evolution of the boundary condition function. It would appear that Kulasegaram used a kernel function different from the cubic spline. Both equations are valid provided that at $\varepsilon = 0$, $\gamma = 0.5$ and at $\varepsilon \geq 2$, $\gamma = 1.0$.

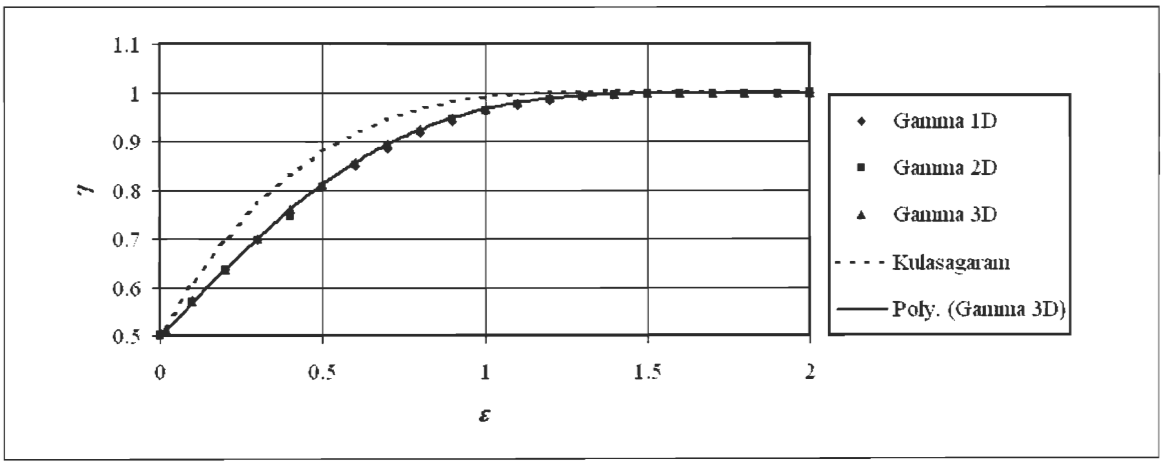

Figure 3.2 Gamma as a function of ε

Therefore, the boundary correction function restores the zero order consistency at the boundary of a contact interface. It is included in the mathematical developments for the conservation equations so that it can be applied if desired. Another approach to restore the

consistency is to apply the normalization to the kernel and/or its gradient which are used in the approximation [46, 75]. The normalization technique will be further discussed in the next section with the development of the kernel gradient.

3.3 Evaluation of DW

When the smoothing length is taken into account in the evaluation of the kernel gradient, it is necessary to develop a consistent total derivative of the kernel function, DW, in terms of x and h. Given that all kernel functions are dependent on r and h, the gradient is given by:

$$DW = \frac{\partial W}{\partial r} Dr + \frac{\partial W}{\partial h} Dh \tag{3.21}$$

The gradient of W can be expanded and given in terms of $\frac{\partial W}{\partial r}$. With r, the scalar distance between two particles written as:

$$r_{ij} = \sqrt{(\vec{x}_i - \vec{x}_j)\cdot(\vec{x}_i - \vec{x}_j)} \tag{3.22}$$

Its derivative with respect to the position of particle i is:

$$\begin{aligned} Dr_{ij} &= \frac{Dr_{ij}}{D\vec{x}_i} = \frac{1}{2}\frac{1}{\sqrt{(\vec{x}_i - \vec{x}_j)\cdot(\vec{x}_i - \vec{x}_j)}}\left(2(\vec{x}_i - \vec{x}_j)\right) \\ &= \frac{1}{r_{ij}}(\vec{x}_i - \vec{x}_j) \end{aligned} \tag{3.23}$$

To calculate the partial derivative of W with respect to the smoothing length, it is useful to express W in terms of $W(R,h) = \alpha(h) f(R)$ where R is also a function of r and h (see equation (3.8)). The derivative of W with respect to h is:

$$\frac{\partial W}{\partial h} = \frac{\partial \alpha}{\partial h} f(R) + \alpha(h) \frac{\partial f}{\partial R} \frac{\partial R}{\partial h}$$
$$= -d_m \frac{\text{cte}}{h^{dm+1}} f(R) + \alpha(h) \frac{\partial f}{\partial R}\left(-\frac{r}{h^2}\right) = -\frac{d_m}{h} \underbrace{\frac{\text{cte}}{h^{dm}} f(R)}_{W} - \frac{r}{h} \underbrace{\alpha(h) \frac{\partial f}{\partial R}\left(\frac{1}{h}\right)}_{\frac{\partial W}{\partial r}} \quad (3.24)$$
$$= -\frac{1}{h}\left(d_m W + r \frac{\partial W}{\partial r}\right)$$

Finally, *Dh* can be found based on the assumption that the number of particles within the domain is constant, which causes *h* to vary through time in function of the density change.

$$\rho_0 h_0^{dm} = \rho h^{dm} = \text{cte}$$
$$D\rho h^{dm} + \rho d_m h^{dm-1} Dh = \text{cte} = 0 \quad (3.25)$$
$$Dh = -D\rho \frac{h}{d_m \rho}$$

The results of equations (3.23), (3.24), and (3.25) can be used to write the gradient again:

$$DW = \frac{\partial W}{\partial r_{ij}} \frac{1}{r_{ij}} (\vec{x}_i - \vec{x}_j) + \frac{1}{d_m \rho}\left(d_m W + r_{ij} \frac{\partial W}{\partial r_{ij}}\right) D\rho \quad (3.26)$$

As to allow the smoothing length to evolve with time, different approaches have been used. Liu [42] used the following two options in his program:

$$h = 2\left(\frac{m}{\rho}\right)^{1/dm} \quad (3.27)$$

$$Dh = -D\rho \frac{h}{d_m \rho} \quad (3.28)$$

He also suggested another approach that keeps the number of particles constant in the domain, which has been used by Bonet [60]:

$$h = h_0\left(\frac{\rho_0}{\rho}\right)^{1/dm} \quad (3.29)$$

Note that both equations (3.28) and (3.29) are taken from the development in equation (3.25).

3.3.1 Results of treating *h* as a variable

To illustrate the impact of considering h variable, the cubic kernel function can be analyzed. The cubic kernel function given in equation (3.3) is used. In the work of Liu [42], h is considered constant when calculating the derivative. Therefore the gradient is simply given by:

$$DW = \frac{\partial W}{\partial r}\frac{1}{r}\left(\vec{x}_i - \vec{x}_j\right) \tag{3.30}$$

Applying equation (3.30) to the cubic kernel yields:

$$DW = \frac{\partial W}{\partial R}\frac{1}{h} = \frac{\alpha_{dm}}{h} \times \begin{cases} -2R + \frac{3}{2}R^2 & 0 \le R < 1 \\ \frac{1}{2}(2-R)^2 & 1 \le R < 2 \\ 0 & R \ge 2 \end{cases} \tag{3.31}$$

On the other hand, applying equation (3.26) to the cubic kernel yields three set of gradients since the dimension of the problem is a variable in the solution. Therefore, in one dimension, the gradient is:

$$\nabla W(R,h) = \frac{\alpha_{dm}}{6h} \times \begin{cases} -\left(4 + 12R - 27R^2 + 12R^3\right) & 0 \le R < 1 \\ (2-R)^2(4R-5) & 1 \le R < 2 \\ 0 & R \ge 2 \end{cases} \tag{3.32}$$

In two dimensions:

$$\nabla W(R,h) = \frac{\alpha_{dm}}{6h} \times \begin{cases} -\left(8 + 12R - 33R^2 + 15R^3\right) & 0 \le R < 1 \\ (2-R)^2(5R-7) & 1 \le R < 2 \\ 0 & R \ge 2 \end{cases} \tag{3.33}$$

And in three dimensions:

$$\nabla W(R,h) = \frac{\alpha_{dm}}{6h} \times \begin{cases} -\left(4 + 4R - 13R^2 + 6R^3\right) & 0 \le R < 1 \\ (2-R)^2(2R-3) & 1 \le R < 2 \\ 0 & R \ge 2 \end{cases} \qquad (3.34)$$

Equations (3.3) and (3.31) to (3.34) are plotted in Figure 3.3. The gradient computed considering a variable h is different from that computed with a constant h, as shown by these equations. One may notice that the derivative of the kernel function when considering h is not equal to zero, but this is not a requirement for the kernel function to be acceptable. Moreover, not all kernel functions' gradients are equal to zero when R is zero, such as the quadratic and super-Gaussian kernels [42]. In Section 3.6, some sample problems are used to demonstrate the improvement resulting from equation (3.26) and the use of the energy conservation equations.

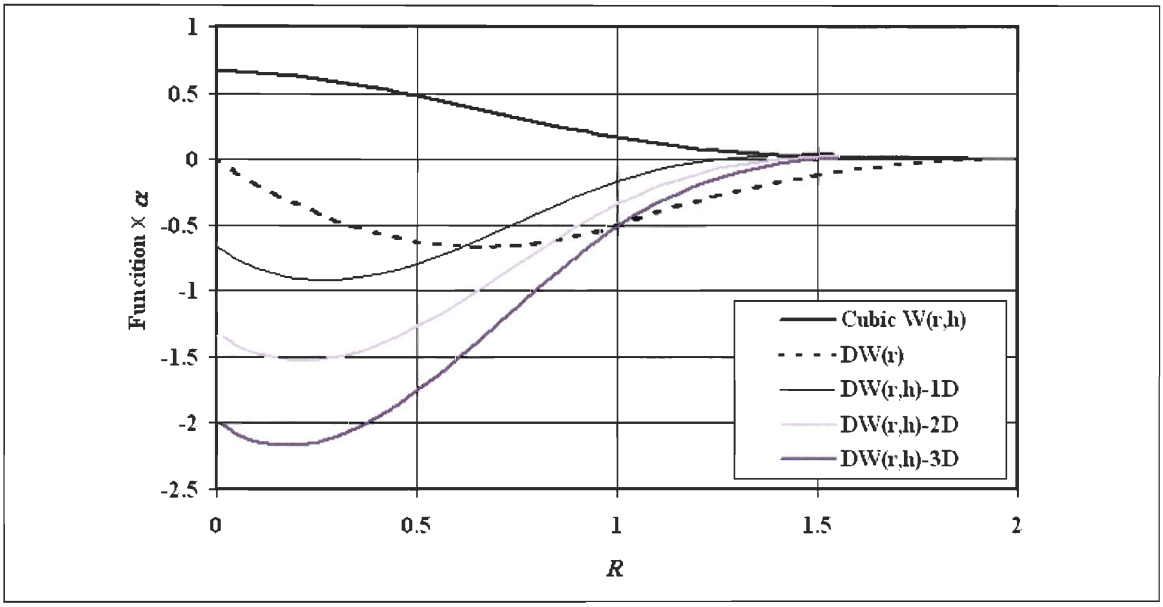

Figure 3.3 Cubic kernel and its derivatives

3.3.2 Normalization

All the assumptions regarding the SPH approach are based on a complete approximation domain. However, it is generally inaccurate for the particles near a boundary. In most cases, this is of small consequence, but when dealing with solids, it can induce tensile instability. The boundary correction suggested by Bonet address the incomplete domain when the solid/projectile approaches a boundary. However, this does not treat free edges. Hence, a

correction applied to the whole domain is preferable. Because the sum of the kernel approximation over the domain of a particle is theoretically equal to unity, the correction applied to enforce that hypothesis is called normalization. In theory, the approximation of equations (3.4) and (3.5) over the support of a particle *i* is given by:

$$1 = \int_{\Omega} 1 \cdot W\left(\vec{x}_i - \vec{x}_j, h_i\right) d\vec{x}_j = \sum_{j=1}^{n} \frac{m_j}{\rho_j} W_{ij} = 1 \qquad (3.35)$$

$$\nabla 1 = \int_{\Omega} 1 \cdot \nabla W\left(\vec{x}_i - \vec{x}_j, h_i\right) d\vec{x}_j = \sum_{j=1}^{n} \frac{m_j}{\rho_j} \nabla W_{ij} = 0 \qquad (3.36)$$

Note that for the sake of brevity, $W\left(R_{ij}, h_i\right)$ is written W_{ij} and that it is a scalar where as the gradient of the kernel function, ∇W_{ij}, is a vector.

If the domain is incomplete, the constant fields are not reproduced correctly and this results in spurious gradients and others numerical errors. Since the convergence properties of the method strongly depend on its capability of reproducing given function, several corrective actions have been considered. In the literature, different approaches using kernel interpolation techniques capable of reproducing exactly constant functions and gradient of linear and higher order polynomial functions have been analyzed. Here the normalized smoothing method proposed in Bonet [46,86] and Randles [75] for obtaining linear consistency in the interpolation of the function and in the interpolation of the gradient have been considered.

A first type of correction is often performed on the kernel itself to provide an improved interpolation near the boundaries and free edges. The consistency conditions are enforced by using a function C_h so that:

$$\sum_{j=1}^{n} \frac{m_j}{\rho_j} C_h W_j = \sum_{j=1}^{n} \frac{m_j}{\rho_j} \widetilde{W}_j = 1 \qquad (3.37)$$

with $C_h = a(x)[1 + b(x) \cdot (\vec{x}_i - \vec{x}_j)]$ and $\widetilde{W}_j = C_h W_j$ is the corrected kernel. Since exact evaluation of coefficient a and b is memory and computationally expensive, b is taken as zero and an approximate value of a is taken as:

$$\widetilde{W}_{ij} = a(x)W_{ij} = \frac{1}{\sum_{j=1}^{n} \frac{m_j}{\rho_j} W_{ij}} W_{ij} \tag{3.38}$$

Note that previously, the kernel could be calculated for the interaction between two particles and be used symmetrically, i.e. $W_{ij} = W_{ji}$, but this is no longer true when the normalization is applied and $\widetilde{W}_{ij} \neq \widetilde{W}_{ji}$.

Now, according to Bonet [86], the development of the gradient correction is based on the following identity, which holds if the velocity distribution is correctly evaluated:

$$\sum_{j=1}^{N} \frac{m_j}{\rho_j} (\vec{x}_j - \vec{x}_i) \times \nabla W_{ij} = \vec{I} \tag{3.39}$$

If the support domain is incomplete, the above equation is not equal to the identity matrix and a 3×3 correction matrix $\vec{L}_{cor\,i}$ is needed and computed for the particle *i*. The correction matrix is defined as the inverse of equation (3.39) and given by:

$$\vec{L}_{cor\,i} = \left(\sum_{j=1}^{N} \frac{m_j}{\rho_j} \nabla W_{ij} \times (\vec{x}_j - \vec{x}_i) \right)^{-1} \tag{3.40}$$

Which, using the tensor notation gives where the superscripts α, β denote the coordinate directions:

$$L^{\alpha\beta}_{cor\,i} = \left(\sum_{j=1}^{N} \frac{m_j}{\rho_j} \nabla W^{\alpha}_{ij} (x^{\beta}_j - x^{\beta}_i) \right)^{-1} \tag{3.41}$$

The quantity in parenthesis is first evaluated for all the particles, and then the correction matrix is computed for each particle by calculating the inverse matrix. The resulting corrected gradient is:

$$\widetilde{\nabla} W^{\alpha}_{ij} = L^{\alpha\beta}_{cor\,i} \nabla W^{\alpha}_{ij} \tag{3.42}$$

Thus, the evaluation of the gradient of a function using the corrected gradient is:

$$\langle \nabla f(x_i) \rangle = \sum_j \frac{m_j}{\rho_j} f(x_j) \cdot \tilde{\nabla}_i W_{ij}^{\alpha} = \left[\sum_j \frac{m_j}{\rho_j} f(x_j) \cdot \nabla W_{ij}^{\alpha} \right] L_{cor\,i}^{\alpha\beta} \tag{3.43}$$

which ensures that the gradient of a general constant or linear function is correctly evaluated.

Finally, a mixed kernel and gradient correction can be used by combining equations (3.38) and (3.42) to yield:

$$\tilde{\nabla} \tilde{W}_{ij}^{\alpha} = L_{cor\,i}^{\alpha\beta} \nabla \tilde{W}_{ij}^{\alpha} \tag{3.44}$$

Where

$$\nabla \tilde{W}_{ij}^{\alpha} = \frac{\nabla W_{ij}^{\alpha} - \frac{\sum_{j=1}^{n} \frac{m_j}{\rho_j} \nabla W_{ij}^{\alpha}}{\sum_{j=1}^{n} \frac{m_j}{\rho_j} W_{ij}^{\alpha}}}{\sum_{j=1}^{n} \frac{m_j}{\rho_j} W_{ij}^{\alpha}} \tag{3.45}$$

It is important to recall that the calculated correction will be different if the summation is calculated for the particle *i* or the particle *j*. The corrected kernel can then be used instead of the previously calculated one in the conservation equations developed in section 3.4.

3.4 Conservation equations

In this section, the equations for the mass and momentum conservation are developed for a variable *h* scenario and include the boundary correction function. The equations for only the variable *h* case can easily be found by setting the boundary correction function and its derivative to 1 and 0 respectively. The developments will not be given, but the resulting equations are provided. When using the normalization correction, the equations for the variable *h* case should be used without the boundary correction function since the boundary correction is a type of local normalization in the sense that it contributes to restore the consistency on the boundary.

3.4.1 Mass Conservation

Typically, the mass conservation equation for the SPH method is developed from the Eulerian continuity equation given by:

$$\frac{D\rho_i}{Dt} = -\rho_i \frac{\partial v_i^\beta}{\partial x_i^\beta} \tag{3.46}$$

The SPH approximation of the continuity equation is then:

$$\frac{D\rho_i}{Dt} = -\rho_i \sum_{j=1}^{N} \frac{m_j}{\rho_j} v_j^\beta \frac{\partial W_{ij}}{\partial x_i^\beta} \tag{3.47}$$

Generally, equation (3.47) is written using the velocity difference between particles i and j (v_{ij}^β) instead of v_j^β which is accomplished by adding the approximation of equation (3.15) in the approximation of equation (3.47) for the gradient of a function. This is valid only if equation (3.15) is equal to zero, which only happens inside the domain and it results in the following SPH approximation of the continuity equation:

$$\frac{D\rho_i}{Dt} = \rho_i \sum_{j=1}^{N} \frac{m_j}{\rho_j} v_{ij}^\beta \frac{\partial W_{ij}}{\partial x_i^\beta} \tag{3.48}$$

This form is preferred because it uses the relative velocity of the particles pairs which helps to reduce errors due to the particle inconsistency problem [42,82]. However, equations (3.4) and (3.5) are inaccurate near boundaries and in order to take the boundaries into consideration, it is easier to begin the development from the summation density equation:

$$\rho_i \gamma_i = \sum_{j=1}^{N} m_j W\left(\vec{x}_i - \vec{x}_j, h_i\right) \tag{3.49}$$

where γ_i is the normalization factor. Then, following a velocity variation $\delta\vec{v}$, a directional derivative is applied to give:

$$D\rho_i\gamma_i[\delta\vec{v}] + \rho_i D\gamma_i[\delta\vec{v}] = \sum_{j=1}^{N} m_j DW\left(\vec{x}_i - \vec{x}_j, h_i\right)[\delta\vec{v}] \tag{3.50}$$

The gradient of h is already given in equation (3.26), so given that $D\rho$ is the term to define, $D\gamma$ is the only term that needs to be developed. Note that γ depends on ε, itself a function of y/h:

$$\begin{aligned} D\gamma_i[\delta\vec{v}] &= \left(\frac{\partial\gamma_i}{\partial\varepsilon}\frac{\partial\varepsilon}{\partial h}+\frac{\partial\gamma_i}{\partial\varepsilon}\frac{\partial\varepsilon}{\partial y}\right)[\delta\vec{v}] \\ &= \frac{\gamma_i' y_i}{h_i\rho_i d_m} D\rho_i[\delta\vec{v}]+\frac{\gamma_i'}{h_i}[\vec{n}\cdot\delta\vec{v}] \end{aligned} \tag{3.51}$$

where γ' is the derivative of the boundary correction function with respect to ε.

Combining equations (3.26), (3.50) and (3.51), the continuity equation becomes:

$$\begin{aligned} &D\rho_i\gamma_i[\delta\vec{v}]+\rho_i\left(\frac{\gamma_i' y_i}{h_i\rho_i d_m} D\rho_i[\delta\vec{v}]+\frac{\gamma_i'[\vec{n}\cdot\delta\vec{v}]}{h_i}\right) \\ &= \sum_{j=1}^{N} m_j\left(\frac{\partial W_{ij}}{\partial r_{ij}}\frac{1}{r_{ij}}(\vec{x}_i-\vec{x}_j)+\frac{1}{d_m\rho_j}\left(d_m W_{ij}+r_{ij}\frac{\partial W_{ij}}{\partial r_{ij}}\right)D\rho_i\right)[\delta\vec{v}] \end{aligned} \tag{3.52}$$

Note that in agreement with equation (3.35):

$$\sum_{j=1}^{N} m_j\frac{1}{d_m\rho_j} d_m W D\rho_i[\delta\vec{v}] = \underbrace{\sum_{j=1}^{N}\frac{m_j}{\rho_j} W}_{\gamma_i} D\rho_i[\delta\vec{v}] = \gamma_i D\rho_i[\delta\vec{v}] \tag{3.53}$$

So finally the continuity equation, upon replacing $\frac{\partial W_{ij}}{\partial r_{ij}}\frac{1}{r_{ij}}(\vec{x}_i-\vec{x}_j)$ with the gradient ∇W_{ij}, is:

$$D\rho_i[\delta\vec{v}] = \left[\frac{\gamma_i' y_i}{h_i d_m}-\frac{1}{d_m\rho_i}\sum_{j=1}^{N} m_j r_{ij}\frac{\partial W_{ij}}{\partial r_{ij}}\right]^{-1}\left[\sum_{j=1}^{N} m_j\nabla W_{ij}[\delta\vec{v}]-\frac{\gamma_i'[\vec{n}\cdot\delta\vec{v}]\rho_i}{h_i}\right] \tag{3.54}$$

It is possible to simplify equation (3.54) by defining a parameter β such that:

$$\beta_i = \left[\frac{\gamma_i' y_i}{h_i d_m}-\frac{1}{d_m\rho_i}\sum_{j=1}^{N} m_j r_{ij}\frac{\partial W_{ij}}{\partial r_{ij}}\right]^{-1} \tag{3.55}$$

And δv is approximated by v so that the density rate implemented is:

$$\dot{\rho}_i = \beta_i \left[\sum_{j=1}^{N} m_j \nabla W_{ij} \cdot \left(\vec{v}_i - \vec{v}_j \right) - \frac{\gamma_i' \left[\vec{n} \cdot \vec{v}_i \right] \rho_i}{h_i} \right] \tag{3.56}$$

Now, if the boundary correction function is not in use, $\gamma = 1$, $\gamma' = 0$, equation (3.54) becomes:

$$\dot{\rho}_i = \beta_i' \left[\sum_{j=1}^{N} m_j \nabla W_{ij} \cdot \left(\vec{v}_i - \vec{v}_j \right) \right] \tag{3.57}$$

With β_i' as:

$$\beta_i' = \left[-\frac{1}{d_m \rho_i} \sum_{j=1}^{N} m_j r_{ij} \frac{\partial W_{ij}}{\partial r_{ij}} \right]^{-1} \tag{3.58}$$

This covers the mass conservation calculation for the SPH formulation.

3.4.2 Momentum Conservation

The momentum equation can be developed from the energy conservation principle. If there are no dissipative effects, the energy equilibrium for a system can be written out as:

$$\frac{d}{dt} \frac{\partial L}{\partial \vec{v}_i} - \frac{\partial L}{\partial \vec{x}_i} = -\frac{\partial \Pi_{dis}}{\partial v_i} \tag{3.59}$$

where L is the Lagrangian of the system and Π_{dis} is the dissipative energy. Moreover, given that the Lagrangian L is made of the kinetic, potential and internal energy, $L = K - \Pi_g - \Pi_{int}$, then (3.59) becomes:

$$\frac{d}{dt} \frac{\partial K}{\partial \vec{v}_i} - \frac{\partial K}{\partial \vec{x}_i} = \frac{\partial \Pi_g}{\partial \vec{x}_i} - \frac{\partial \Pi_{int}}{\partial \vec{x}_i} - \frac{\partial \Pi_{dis}}{\partial v_i} \tag{3.60}$$

which can be expressed as the Newton's second law as:

$$m_i a_i = \underbrace{F_i}_{\text{gravity}} - \underbrace{T_i^{int}}_{\text{internal}} - \underbrace{T_i^{dis}}_{\text{dissipative}} \tag{3.61}$$

The subsequent work will develop the momentum conservation with:

$$\frac{d\vec{v}_i}{dt} = a_i = a_i^g + a_i^{int} + a_i^{dis} = a_i^g + a_i^{vol} + a_i^{dev} + a_i^{dis} \tag{3.62}$$

where the acceleration due to the internal potential energy is made of a volumetric and deviatoric part. In the case of gravity, the acceleration can be easily computed as:

$$a_i^g = \frac{F_i}{m_i} = -\frac{1}{m_i}\frac{\partial \Pi_g}{\partial x_i} = -\frac{1}{m_i}\left(-m_i \vec{g}\right) = \vec{g} \tag{3.63}$$

The volumetric term of the acceleration can be calculated using the pressure internal potential energy [60, 86]:

$$\begin{aligned} D\Pi_{vol}^{p}\left[\delta\vec{v}\right] &= \sum_{i=1}^{Ntot} T_i \cdot \delta\vec{v}_i \\ &= -\sum_{i=1}^{Ntot} m_i \frac{p_i}{\rho_i^2} D\rho_i\left[\delta\vec{v}\right] \end{aligned} \tag{3.64}$$

where *Ntot* is the summation over the whole discretized system. Replacing $D\rho_i\left[\delta\vec{v}\right]$ by equation (3.56) yields:

$$D\Pi_{vol}\left[\delta\vec{v}\right] = \sum_{i=1}^{Ntot} m_i \frac{p_i}{\rho_i^2}\beta_i\left[\sum_{j=1}^{N} m_j \nabla W_{ij} \cdot \left(\delta\vec{v}_j - \delta\vec{v}_i\right) - \frac{\rho_i \gamma'_i}{h_i}\left[\vec{n} \cdot \delta\vec{v}_i\right]\right] \tag{3.65}$$

and the acceleration due to the volumetric part of the internal energy is:

$$\vec{a}_i^{vol} = \sum_{j=1}^{N} m_j \left(\frac{\beta_j p_j}{\rho_j^2} + \frac{\beta_i p_i}{\rho_i^2}\right)\nabla W_{ij} - \frac{\beta_i p_i \gamma_i'}{h_i \rho_i}\vec{n} \tag{3.66}$$

If the boundary correction function is not used, then (3.66) becomes:

$$\vec{a}_i^{vol} = \sum_{j=1}^{N} m_j \left(\frac{\beta'_j p_j}{\rho_j^2} + \frac{\beta'_i p_i}{\rho_i^2}\right)\nabla W_{ij} \tag{3.67}$$

where β' is defined in equation (3.58).

In case of elasticity, the internal energy will also include a deviatoric part due to shear such that:

$$\sigma^{\alpha\beta} = -p\delta^{\alpha\beta} + \tau^{\alpha\beta} \tag{3.68}$$

Hence the associated internal energy is:

$$\Pi_{dev} = \sum_{i=1}^{Ntot} m_i \left(\frac{\tau_i^{\alpha\beta}}{\rho_i} \right) \tag{3.69}$$

and the associated internal force:

$$T_i^{dev} = m_i \frac{\partial}{\partial \vec{v}_i} \left(\frac{\tau_i^{\alpha\beta}}{\rho_i} \right) \tag{3.70}$$

Since the equations developed so far have been put in symmetrical form for greater stability to the method, it is convenient to write:

$$\begin{aligned} \frac{\partial}{\partial \vec{v}} \left(\frac{\tau^{\alpha\beta}}{\rho} \right) &= \frac{1}{\rho} \frac{\partial}{\partial \vec{v}} \left(\tau^{\alpha\beta} \right) - \frac{\tau^{\alpha\beta}}{\rho^2} \frac{\partial \rho}{\partial \vec{v}} \\ \frac{1}{\rho_i} \frac{\partial}{\partial \vec{v}} \left(\tau_i^{\alpha\beta} \right) &= \frac{\tau^{\alpha\beta}}{\rho^2} \frac{\partial \rho}{\partial \vec{v}} + \frac{\partial}{\partial \vec{v}} \left(\frac{\tau^{\alpha\beta}}{\rho} \right) \\ &= \left(\sum_j \frac{m_j}{\rho_j} \frac{\tau_j^{\alpha\beta}}{\rho_j} \nabla W_{ij} + \frac{\tau_i^{\alpha\beta}}{\rho_i^2} \sum_j \frac{m_j}{\rho_j} \rho_j \nabla W_{ij} \right) \\ &= \sum_j m_j \left(\frac{\tau_i^{\alpha\beta}}{\rho_i^2} + \frac{\tau_j^{\alpha\beta}}{\rho_j^2} \right) \nabla W_{ij} \end{aligned} \tag{3.71}$$

So that the acceleration provided by the deviatoric internal energy becomes:

$$a_i^{dev} = \sum_j m_j \left(\frac{\tau_i^{\alpha\beta}}{\rho_i^2} + \frac{\tau_j^{\alpha\beta}}{\rho_j^2} \right) \nabla W_{ij} \tag{3.72}$$

In case of incompressible viscous fluid media, the shear stresses are associated with the viscous term hence with a dissipative potential. Hence the dissipative potential, caused by

the shear in the fluid material, depends on the constitutive law of the deviatoric viscous stress and is written as:

$$\Pi_{dis} = \sum_{i=1}^{Ntot} m_i \left(\frac{\tau_i^{\alpha\beta}}{\rho_i} \right) \tag{3.73}$$

As one can see, equation (3.73) is essentially the same as (3.69) and the developments to get to the acceleration term are the exact same. Thus, the dissipative acceleration is:

$$\vec{a}_i^{dis} = \sum_j m_j \left(\frac{\tau_i^{\alpha\beta}}{\rho_i^2} + \frac{\tau_j^{\alpha\beta}}{\rho_j^2} \right) \nabla W_{ij} \tag{3.74}$$

Finally, $\tau_i^{\alpha\beta}$ itself needs to be computed. In the case of a Newtonian fluid, the constitutive law is:

$$\tau_i^{\alpha\beta} = \mu_i \varepsilon_i^{\alpha\beta} = \mu_i \left(\frac{\partial \vec{v}^{\,\alpha}}{\partial \vec{x}^{\,\beta}} + \frac{\partial \vec{v}^{\,\beta}}{\partial \vec{x}^{\,\alpha}} - \frac{2}{3} (\nabla \cdot \vec{v}) \delta^{\alpha\beta} \right) \tag{3.75}$$

where μ is the dynamic viscosity and ε is the strain rate. Once again, a few mathematical manipulations are performed to obtain a symmetrical equation.

$$\begin{aligned} \frac{1}{\rho} \frac{\partial}{\partial \vec{x}} (\rho \vec{v}) &= \frac{1}{\rho} \rho \frac{\partial \vec{v}}{\partial \vec{x}} + \frac{1}{\rho} \vec{v} \frac{\partial \rho}{\partial \vec{x}} \\ \vec{x} &= \frac{1}{\rho} \frac{\partial}{\partial \vec{x}} (\rho \vec{v}) - \frac{1}{\rho} \vec{v} \frac{\partial \rho}{\partial \vec{x}} \end{aligned} \tag{3.76}$$

Which is approximated by:

$$\begin{aligned} \frac{\partial \vec{v}_i^{\,\alpha}}{\partial \vec{x}^{\,\beta}} &= \frac{1}{\rho_i \gamma_i} \sum_j \frac{m_j}{\rho_j} \rho_j \vec{v}_j^{\,\alpha} \frac{\partial W_{ij}}{\partial \vec{x}^{\,\beta}} - \frac{1}{\rho_i \gamma_i} \vec{v}_i^{\,\alpha} \sum_j \frac{m_j}{\rho_j} \rho_j \frac{\partial W_{ij}}{\partial \vec{x}^{\,\beta}} \\ &= \frac{1}{\rho_i \gamma_i} \sum_j m_j \vec{v}_{ji}^{\,\alpha} \frac{\partial W_{ij}}{\partial \vec{x}^{\,\beta}} \end{aligned} \tag{3.77}$$

Equations similar to (3.77) can be developed for the terms $\frac{\partial \vec{v}^{\,\beta}}{\partial \vec{x}^{\,\alpha}}$ and $(\nabla \cdot \vec{v})$, where $\vec{v}_{ji} = \vec{v}_j - \vec{v}_i$, so that the final expression for the shear in the Navier-Stokes formulation is:

$$\tau_i^{\alpha\beta} = \frac{\mu_i}{\rho_i \gamma_i}\left(\sum_j m_j \vec{v}_{ji}^{\,\alpha} \frac{\partial W_{ij}}{\partial \vec{x}^{\,\beta}} + \sum_j m_j \vec{v}_{ji}^{\,\beta} \frac{\partial W_{ij}}{\partial \vec{x}^{\,\alpha}} - \frac{2}{3}\sum_j m_j \vec{v}_{ji} \cdot \nabla_i W_{ij} \delta^{\alpha\beta}\right) \quad (3.78)$$

Note that the expression associated with the potential and the dissipative energy are not affected by the variable *h*.

3.5 Other considerations

Here are listed a few additional considerations useful to solve the SPH problem. It includes artificial viscosity, external forces, and boundary identification and the computation of the normal. A leapfrog algorithm is used to update the variables according to the general scheme:

$$\begin{aligned} A\left(t_0 + \Delta t/2\right) &= A\left(t_0\right) + \Delta t/2\, DA\left(t_0\right) \\ A\left(t\right) &= A\left(t - \Delta t/2\right) + \Delta t/2\, DA\left(t - \Delta t\right) \\ A\left(t + \Delta t/2\right) &= A\left(t - \Delta t/2\right) + \Delta t DA\left(t\right) \end{aligned} \quad (3.79)$$

3.5.1 Artificial viscosity

Artificial viscosity is introduced to control unphysical oscillations in the numerical results and is especially meant for shockwaves. It allows for a dissipation of the energy and the most used artificial viscosity was developed and is given as:

$$\Pi_{ij} = \begin{cases} \dfrac{-\alpha_\Pi \bar{c}_{ij} \phi_{ij} + \beta_\Pi \phi_{ij}^2}{\bar{\rho}_{ij}} & \text{if } \vec{v}_{ij} \cdot \vec{x}_{ij} < 0 \\ 0 & \text{if } \vec{v}_{ij} \cdot \vec{x}_{ij} > 0 \end{cases} \quad (3.80)$$

Where:

$$\phi_{ij} = \frac{h_{ij} \vec{v}_{ij} \cdot \vec{x}_{ij}}{\left|x_{ij}\right|^2 + \varphi^2} \quad (3.81)$$

$$\bar{c}_{ij} = \tfrac{1}{2}\left(c_i + c_j\right) \quad (3.82)$$

$$\bar{\rho}_{ij} = \tfrac{1}{2}\left(\rho_i + \rho_j\right) \quad (3.83)$$

$$h_{ij} = \tfrac{1}{2}\left(h_i + h_j\right) \quad (3.84)$$

$$\vec{v}_{ij} = \vec{v}_i - \vec{v}_j \ , \quad \vec{x}_{ij} = \vec{x}_i - \vec{x}_j \tag{3.85}$$

α_Π and β_Π are constants that are typically set around 1.0, the factor $\varphi = 0.1h_{ij}$ is used to prevent divergence and c is the speed of sound.

The artificial viscosity is simply added to the pressure term so that:

$$\left(\frac{p_i}{\rho_i^2} + \frac{p_j}{\rho_j^2}\right) \Rightarrow \left(\frac{p_i}{\rho_i^2} + \frac{p_j}{\rho_j^2} + \Pi_{ij}\right) \tag{3.86}$$

Note that the artificial viscosity is described here because it is a popular feature of the SPH formulation, but it was not used in the examples developed in this chapter because the material considered were not solids.

3.5.2 External forces

The external forces are computed with an equation which creates repulsion from the boundary interface. The force is not a physical value, i.e. it is not related to the magnitude or direction of the velocity of the particles, but it can prevent penetration through a boundary. The equation used is similar to the Lenard-Jones molecular force [42] and is given by:

$$B_i = \begin{cases} D\left[\left(\dfrac{r_0}{r_{ij}}\right)^{n1} - \left(\dfrac{r_0}{r_{ij}}\right)^{n2}\right]\dfrac{1}{r_{ij}^2} & \left(\dfrac{r_0}{r_{ij}}\right) \le 1 \\ 0 & \left(\dfrac{r_0}{r_{ij}}\right) > 1 \end{cases} \tag{3.87}$$

where D, r_0, $n1$, $n2$ are arbitrary parameters determined through experience, B_i is the boundary force, and r_{ij} is the distance between particle i and the boundary j. The resulting acceleration to be applied to a particle is thus given by:

$$\frac{dv_{extfi}^{\alpha}}{dt} = \sum_{j}^{bn} B_j x_{ij}^{\alpha} \tag{3.88}$$

Liu [42] gives some values that can be used for the arbitrary parameters.

3.5.3 Boundary Conditions

So far, Bonet [60] has looked at the boundary correction function for one rigid plane, and Kulasegaram [79] has looked for multiples rigid planes. However, in executing the contact with a flexible structure, the SPH particles are subject to interactions with an irregular plane which changes in time. The value of the boundary correction function is computed using the distance between a real particle and the boundary and in the case where the boundary is not planar, an average normal can be computed in order to keep the computation simple so that the boundary correction function is only a function of the average distance to the boundary and the smoothing length.

Boundaries are identified by calculating the value of the kernel at each particle. If the kernel calculated for a given particle has a value less than 0.85-0.90 of the original value, then the particle is flagged as being on the boundary:

$$\sum_{j=1}^{N} \frac{m_j}{\rho_j} W_{ij} \leq 0.85 \tag{3.89}$$

The normal of each particle is calculated according to Seo *et al* [83] using the gradient of the kernel:

$$\vec{n}_i = \frac{\sum_{j=1}^{N} \frac{m_j}{\rho_j} \nabla W_{ij}}{\left| \sum_{j=1}^{N} \frac{m_j}{\rho_j} \nabla W_{ij} \right|} \tag{3.90}$$

This way of identifying the boundary is efficient and simple enough that it can be used in the case of flexible boundaries and for three dimensional problems.

3.6 Examples of Application

The following case studies demonstrate the validity of the equations presented, as well as an improvement with respect to Liu's original formulation [42] which is the formulation implemented in most commercial software [32,33]. The first example is the shear driven cavity and shows the difference between the different formulations. Because the boundaries

are used to apply a velocity field to the SPH particles, the example is ill-defined to apply the normalization and boundary correction function. Hence, those two corrections will only be applied to the dam collapse example.

3.6.1 Shear Driven Cavity

The shear driven cavity problem is a two-dimensional example where three walls are fixed and a fourth one moves at constant velocity. The four walls form a square cavity filled with fluid, typically water. The shear between the moving wall and the fluid creates motion in the whole cavity and after a period of time, the analysis reaches a steady state for which the velocity of the fluid can be compared with results from the finite difference method (FDM).

In the example used, 1600 particles are evenly distributed in a square cross-section of 0.001 m. The results presented are normalized. Hence, the dimensions are divided by the cross-section length, 0.001 m, and the velocities are divided by the velocity of the moving boundary, which is of 0.001 m/s. The initial particle distribution is illustrated in Figure 3.4 where there are 320 boundary particles.

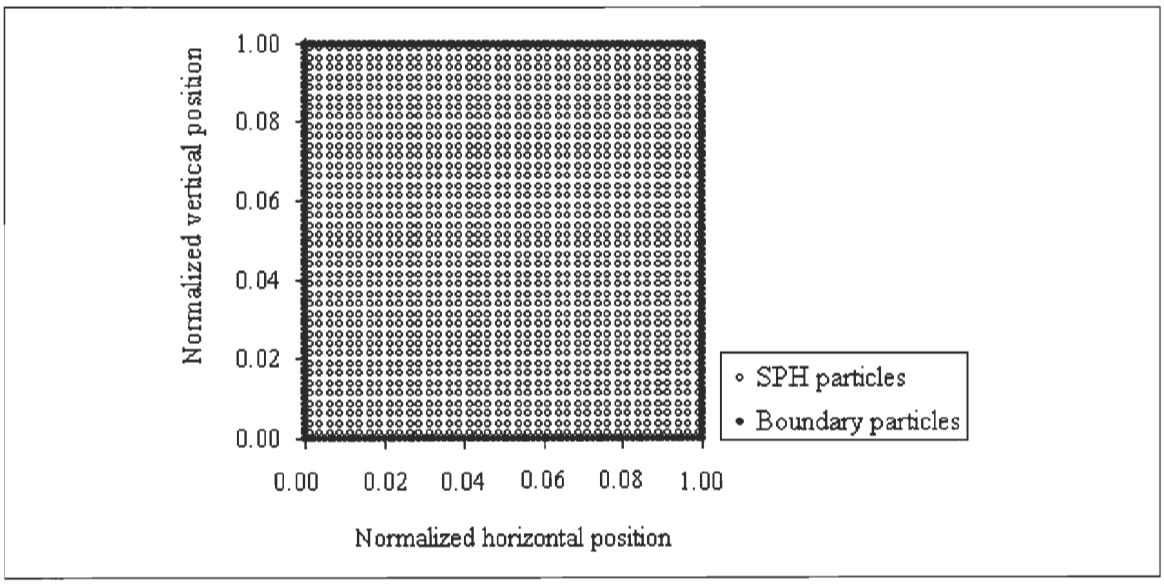

Figure 3.4 Initial particle distribution

Liu [42] provides a solution which compares well with the finite difference method results. The time step is fixed to a value of 5.0e-5 s and the steady state is reached at 0.15 s with the summation density equation, and at 0.25 s for the other methods. However, the results

given are based on using the summation density equation where the mass conservation principle is not respected. So Liu's results are compared against the results obtained with the standard continuity equation, and the variable-h energy conservative formulation presented in this paper.

The first set of results is a plot of the vertical velocity along the horizontal centerline, which is shown in Figure 3.5. The results using the variable-h formulation are in better agreement with the finite difference method (FDM) than those using the standard continuity equations. So although the values obtained from FDM are not perfectly matched, the variable-h approach yields the best solution since it respects the mass conservation principle. Next, the horizontal velocity along the vertical centerline is plotted in Figure 3.6. In this instance, the results are also good.

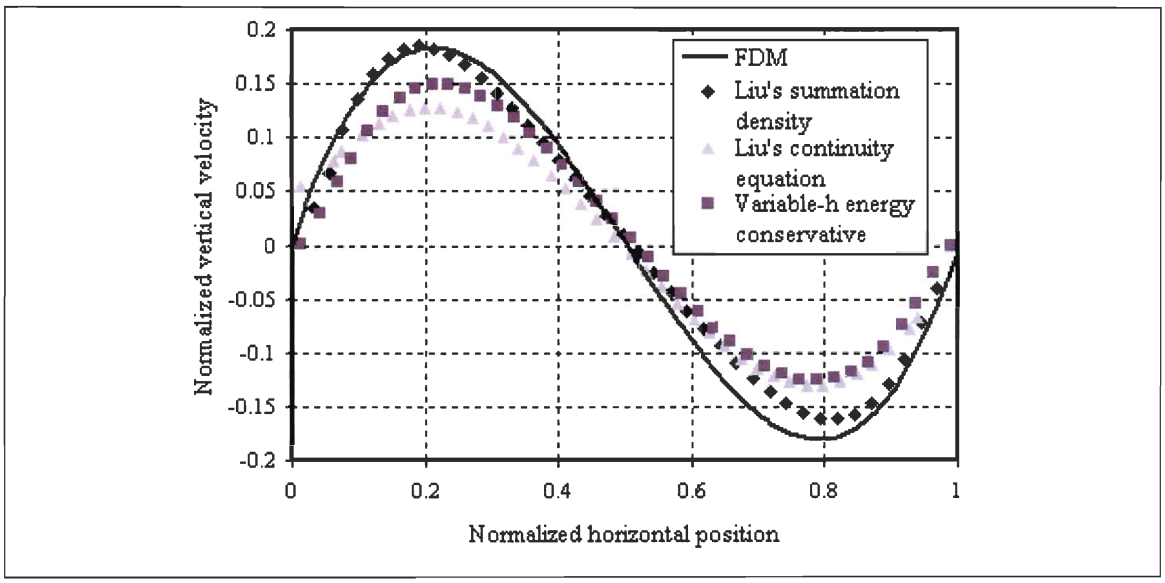

Figure 3.5 Non-dimensional vertical velocity along the horizontal centerline

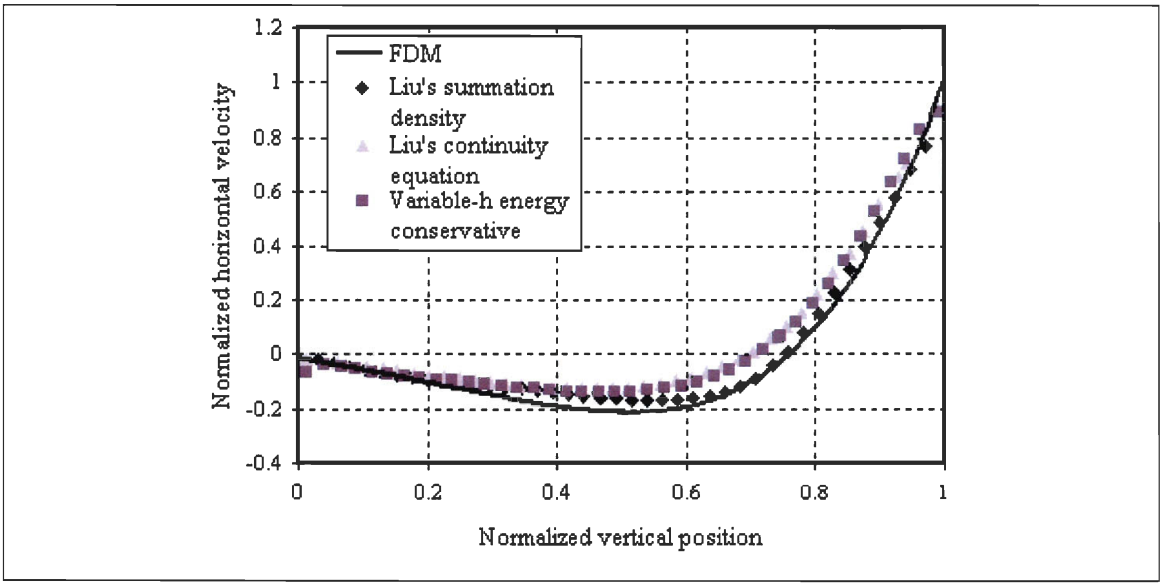

Figure 3.6 Non-dimensional horizontal velocity along the vertical center line

Another avenue of validation is to look at the distribution of the particles at the end of the simulation. In this type of application, the singularity at the corner where the velocity is discontinuous causes some problem [84]. Figure 3.7 shows that the difficulties are better handled by the variable-h energy conservative formulation than the previous continuity equation. Moreover, the particles are properly repulsed by the boundary, whereas for the continuity formulation, the boundary seems to attract the particles and the distribution of the particles is uneven.

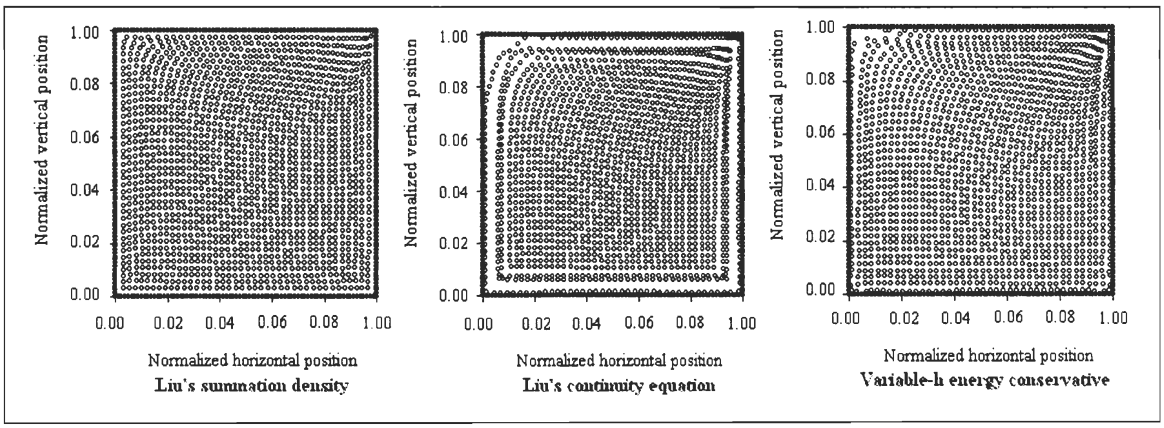

Figure 3.7 Particles' distribution at time 0.15 s with summation density

It is possible to demonstrate with the shear driven cavity example that the variable-h energy conservative approach is an improvement with respect to the solution obtained form the

standard continuity equation, which is mass conservative and should be preferred to the summation density.

3.6.2 Dam Collapse

An experimental study of the dam collapse example has been done in 1952 by Martin and Moyce [85]. It is highly interesting because it is simple to model and results are available. The problem is two-dimensional and consists of a column of water that is allowed to collapse by the instantaneous removal of the dam gate.

In the case studied, the column cross-section is a square of 0.05715 m side-dimension. It is modeled with 2500 SPH particles. The initial particle distribution is shown in Figure 3.8. The kinematics viscosity is set to $0.001\,\mathrm{N\cdot s/m^2}$ and there is no friction along the boundaries. Note that the solution time was comparable for the numerical formulations used with and without corrections such as the boundary correction and the normalization. Thus, the new variable-*h* formulation is as computationally effective as the standard formulation.

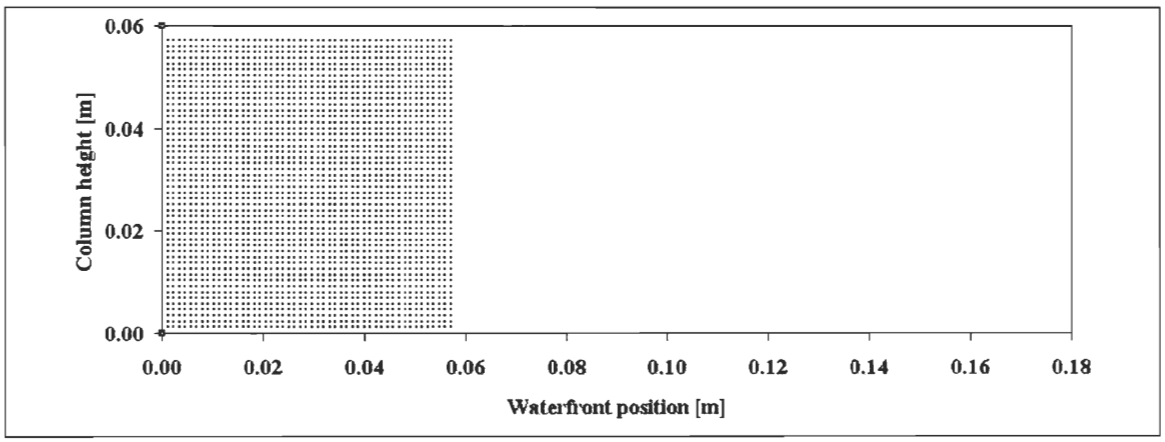

Figure 3.8 Initial particles distribution for dam collapse example

The results are evaluated by plotting the water front position and the column of water height against the experimental data available. Both data are plotted in Figure 3.9 and Figure 3.10 respectively. Agreement between the numerical simulations and the experimental data is good. The small amount of difference can be explained by the fact that the gate, which is quickly removed to initiate the experiment, is not numerically modeled. The slope of steady-state progression of the water front and column height, taken between

0.08 and 0.18 s, are calculated to see if the general movement of the water is the same for numerical and experimental model. The slopes are given in Table 3.1.

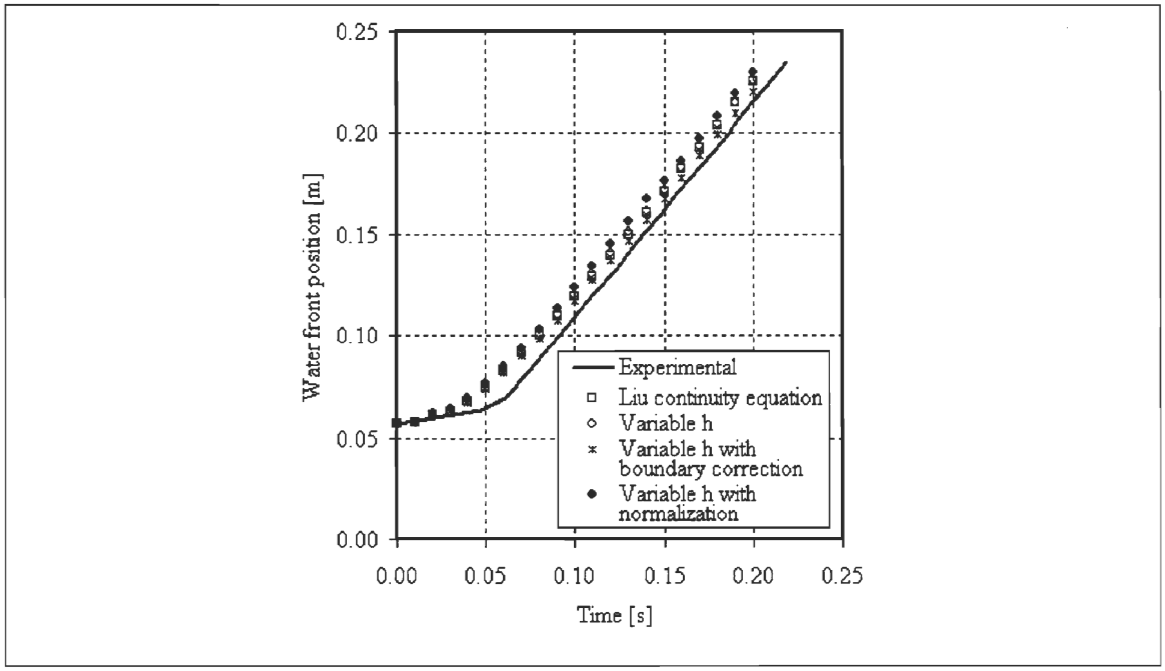

Figure 3.9 **Water front progression of the dam collapse**

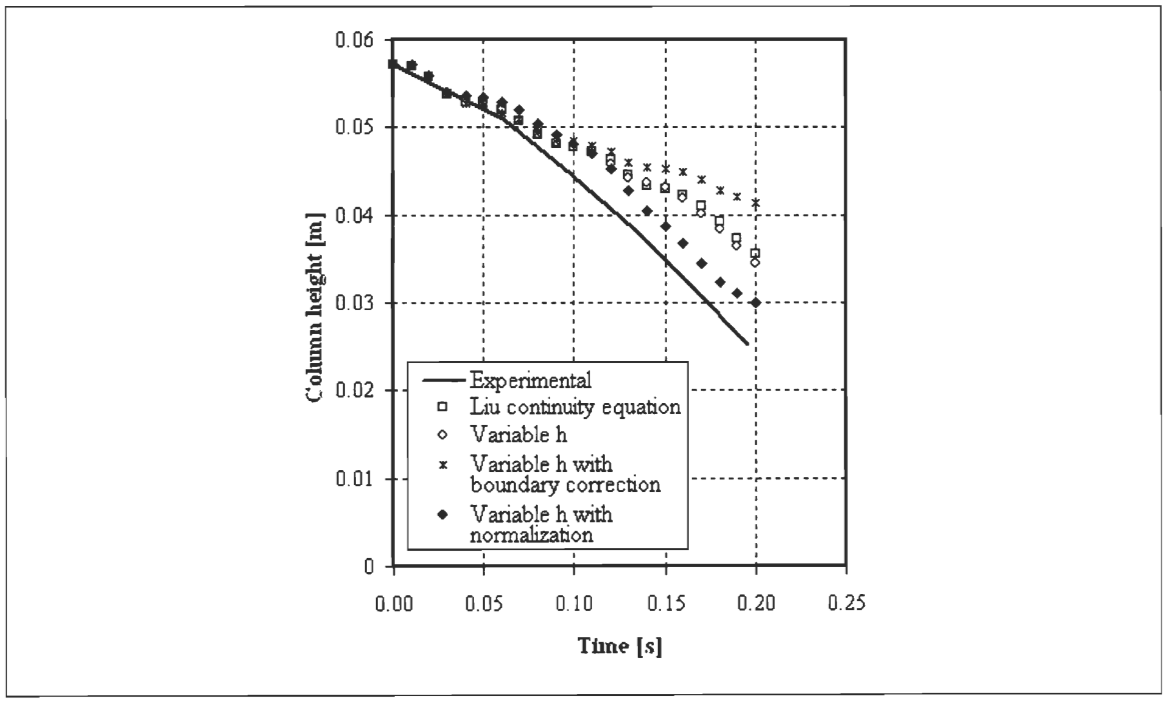

Figure 3.10 **Column height progression of the dam collapse**

Table 3.1 **Slopes of the progression of the dam collapse**

	Slope of water front	Slope of column height
Experimental	**1.4117**	**-0.2657**
Liu continuity equation	1.4085	-0.1593
Variable *h*	1.401	-0.1452
Variable *h* with boundary correction	1.3608	-0.0889
Variable *h* with normalization	1.4114	-0.2456

According to Table 3.1, the best results are obtained when using the normalization combined with the variable *h* energy conservative approach. The boundary correction function doesn't seem to improve the results. There are two reasons for this. First, the external forces used to define the boundaries keep the particles away from the boundary so that the ratio of the particle's distance from the boundary versus the smoothing length is greater than unity, which means that the value of the correction function is very close to unity and hence has very little influence on the results. The second explanation resides in the fact that the boundary correction enhances the bond between the first layer of particles closest to the boundary but this is not uniform through all the particles, as opposed to the normalization of the gradient.

The collapse of the column of water for a time period 0.2 s is shown for this scenario in Figure 3.11. The flow shape is in agreement with the experimental result reported by Bonet [86] and Monaghan [87].

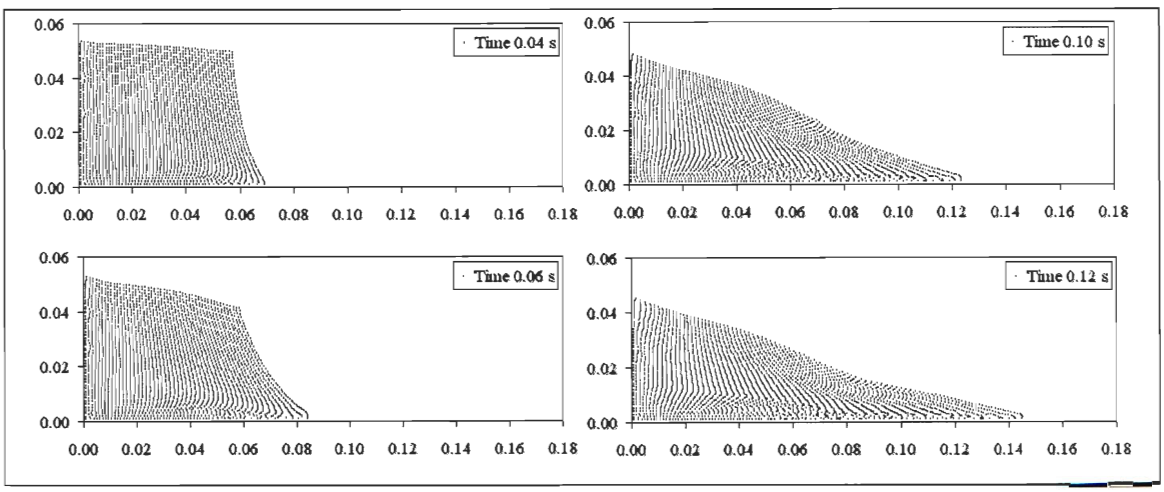

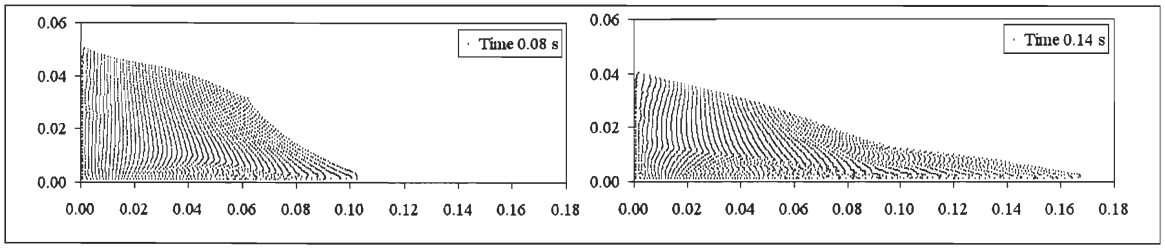

Figure 3.11 Dam collapse new variable-h formulation with normalization

The results from Liu's continuity equation and the variable *h* energy conservative approach with and without the boundary correction function all present a deficiency regarding the behaviour of the particles at the boundary. Because the external forces used to prevent penetration are not proportional to the magnitude and direction of the movement, they create adhesive forces which are well illustrated in Figure 3.13. Note that the behaviour of the variable *h* formulation with and without boundary correction is not represented in Figure 3.12 since it is very similar to the behaviour of Liu's continuity equation. On the left of Figure 3.12 the particles are seen to stick to the boundary more, and on the right, the particles remain attached to the boundary instead of following the flow.

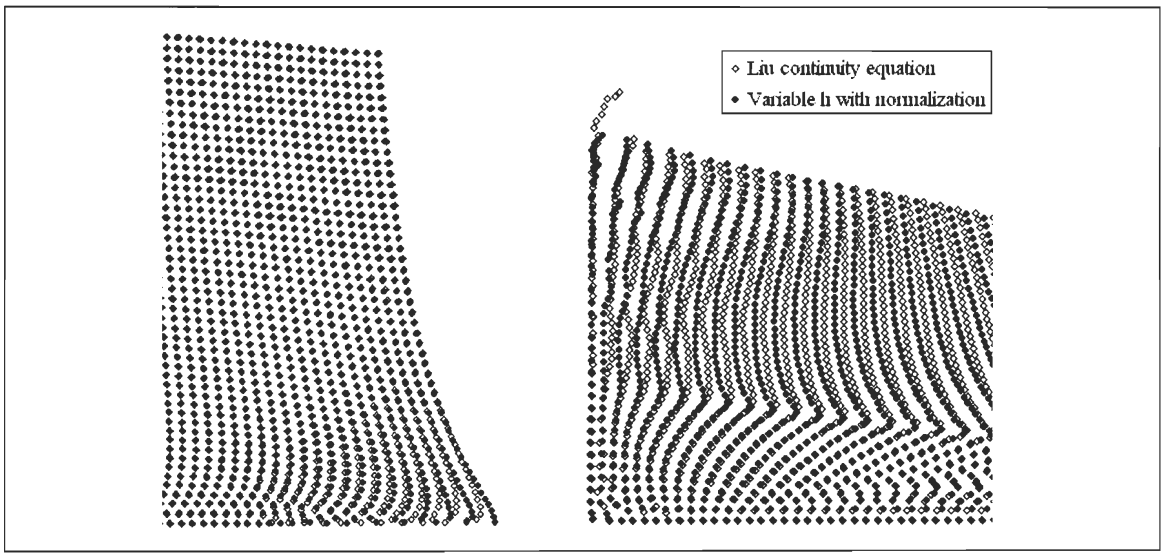

Figure 3.12 Water front progression, time 0.04 s (left) & column height, time 0.15 s (right)

The difficulties encountered at the boundary with by the Liu continuity are enhanced when using the boundary correction function instead of being diminished. It is possible to obtain valid results with the existing SPH formulation, i.e. variable *h* with normalization, but more options need to be investigated for the boundary interaction.

3.7 Conclusions

A new SPH formulation based on an energy conservative approach and where the smoothing length is consistently treated as a variable has been developed. This formulation has been successfully implemented in a mesh free program and is not more demanding from a computational point of view.

Two examples were developed. The shear cavity simulation demonstrated how the new formulation improves the results when compared to the results yielded when using a continuity density scheme. The dam collapse simulation showed the accuracy of the results by comparing with available experimental data and it showed that the normalization is more efficient than the boundary correction function to obtain accurate results. Both examples provide confidence in the formulation developed.

Future work will concentrate on implementing additional material model and developing fluid-structure interaction by using appropriate boundary forces.

4 Additional Material Models

4.1 Introduction

One assumption of the SPH method is that it can be applied to areas other than astrophysics. Developing the equations for gas and fluids was a challenge that Monaghan and Lucy met in the 1980's and this is demonstrated by the examples given in Chapter 3. More recently, the simplicity of the method has motivated many to expand its horizon, namely by applying it to solids. Difficulties arose in terms of numerical instabilities, and other meshless methods were developed to address them such as the element free Galerkin [56,59,88], moving least-squares interpolants [89], Hamiltonian particle hydrodynamics [90], and the boundary point interpolation method [91].

This chapter describes how four additional material models are implemented in the SPH algorithm. The original code has been modified so that a subroutine is always called to calculate the deviatoric stresses. Afterwards, each new material model was programmed as a subroutine and using it is simply a matter of specifying which material model to use in the analysis set-up.

It concludes with two examples: the Taylor impact test, to show that it is possible to use SPH to model solid under large deformations, and the bird impact, to show that the new algorithm can indeed be used to model a soft body impactor. The material models presented are elastic, elastic-plastic, Johnson-Cook, and elastic-plastic-hydrodynamic.

The advantage of having several material models is that the same algorithm can be used for fluids and solids, which later can allow the user to treat fluid-structure interaction problems.

4.2 Elastic Material Model

The elastic material model, as well as the perfectly plastic one, is developed based on the theory found in LS-DYNA [32] and has been cross-referenced with the work of Libersky [75,82].

Given the field of application of the SPH method, the constitutive model used for an elastic material undergoing large deformations is expressed in terms of stress, σ, as a function of pressure, p, and shear, τ. The mathematical relation is given by:

$$\sigma^{\alpha\beta} = -p\delta^{\alpha\beta} + \tau^{\alpha\beta} \tag{4.1}$$

where the volumetric strains are taken care of through the pressure using the Mie-Gruneisen equation of state given by:

$$\begin{aligned} p &= \frac{\rho_0 C^2 \mu\left[1+\left(1-\frac{\gamma_0}{2}\right)\mu-\frac{a}{2}\mu^2\right]}{\left[1-(S_1-1)\mu-S_2\frac{\mu^2}{\mu+1}-S_3\frac{\mu^3}{(\mu+1)^2}\right]^2}+(\gamma_0+a\mu)E, \text{ in compression} \\ &= \rho_0 C^2\mu+(\gamma_0+a\mu)E, \text{ in expansion} \end{aligned} \tag{4.2}$$

where C is the intercept of the $v_S - v_P$ curve, $S_1, S_2,$ and S_3 are the coefficients of the slope of the $v_S - v_P$ curve; γ_0 is the Gruneisen gamma; a is the first order volume correction to γ_0; and $\mu = \frac{\rho}{\rho_0} - 1$ [42].

The shear stresses are computed using the deviatoric strain, $\bar{\varepsilon}^{\alpha\beta}$, and the Jauman stress rate is defined as:

$$\frac{d\tau^{\alpha\beta}}{dt} = \tau^{\alpha\gamma}R^{\beta\gamma} + \tau^{\gamma\beta}R^{\alpha\gamma} + G\bar{\varepsilon}^{\alpha\beta} \tag{4.3}$$

so that the shear is updated for each time step t with:

$$\tau_{\alpha\beta}^{t+1} = \tau_{\alpha\beta}^{t} + \frac{d\tau^{\alpha\beta}}{dt}\times dt \tag{4.4}$$

The strain and rotation rate tensors are known with:

$$\varepsilon^{\alpha\beta} = \frac{1}{2}\left(\frac{\partial\vec{v}^{\alpha}}{\partial\vec{x}^{\beta}} + \frac{\partial\vec{v}^{\beta}}{\partial\vec{x}^{\alpha}}\right) \tag{4.5}$$

$$R^{\alpha\beta} = \frac{1}{2}\left(\frac{\partial\vec{v}^{\alpha}}{\partial\vec{x}^{\beta}} - \frac{\partial\vec{v}^{\beta}}{\partial\vec{x}^{\alpha}}\right) \tag{4.6}$$

$$\bar{\varepsilon}^{\alpha\beta} = \varepsilon^{\alpha\beta} - \tfrac{1}{3}\varepsilon^{\gamma\gamma}\delta^{\alpha\beta} \tag{4.7}$$

Each is evaluated in a manner similar to equation (3.70) and yield:

$$\varepsilon^{\alpha\beta} = \frac{1}{2}\frac{1}{\rho_i\gamma_i}\sum_j m_j\left(\vec{v}_{ji}^{\alpha}\frac{\partial W_{ij}}{\partial\vec{x}^{\beta}} + \vec{v}_{ji}^{\beta}\frac{\partial W_{ij}}{\partial\vec{x}^{\alpha}}\right) \tag{4.8}$$

$$R^{\alpha\beta} = \frac{1}{2}\frac{1}{\rho_i \gamma_i}\sum_j m_j \left(\vec{v}_{ji}^{\,\alpha} \frac{\partial W_{ij}}{\partial \vec{x}^{\,\beta}} - \vec{v}_{ji}^{\,\beta} \frac{\partial W_{ij}}{\partial \vec{x}^{\,\alpha}} \right) \tag{4.9}$$

Given the information provided in equations (4.3) to (4.9), it is possible to evaluate the shear for the SPH formulation of an elastic material sustaining large deformations.

$$\frac{d\tau_i^{\alpha\beta}}{dt} = \frac{1}{\rho_i \gamma_i}\left[\begin{array}{r} \tau_i^{\alpha\gamma}\frac{1}{2}\sum_j m_j \left(\vec{v}_{ji}^{\,\beta} \frac{\partial W_{ij}}{\partial \vec{x}^{\,\gamma}} - \vec{v}_{ji}^{\,\gamma} \frac{\partial W_{ij}}{\partial \vec{x}^{\,\beta}} \right) + \tau^{\gamma\beta}\frac{1}{2}\sum_j m_j \left(\vec{v}_{ji}^{\,\alpha} \frac{\partial W_{ij}}{\partial \vec{x}^{\,\gamma}} - \vec{v}_{ji}^{\,\gamma} \frac{\partial W_{ij}}{\partial \vec{x}^{\,\alpha}} \right) \\ + G\sum_j m_j \left(\vec{v}_{ji}^{\,\alpha} \frac{\partial W_{ij}}{\partial \vec{x}^{\,\beta}} + \vec{v}_{ji}^{\,\beta} \frac{\partial W_{ij}}{\partial \vec{x}^{\,\alpha}} - \frac{1}{3}\vec{v}_{ji} \cdot \nabla_i W_{ij} \delta^{\alpha\beta} \right) \end{array} \right] \tag{4.10}$$

Using the new definition for the shear, the dissipative component of the acceleration in the momentum conservation is still given by equation (3.71) and the deviatoric stresses are computed using equation (4.4) and (4.10).

4.3 Elastic-Plastic Material Model

The elastic plastic material model with isotropic and kinematic hardening is developed here [32].

The deviatoric stresses computed with equations (4.4) and (4.10) are now considered *trial* stresses and denoted $\tau^{*\alpha\beta}$. In order to know if plastic deformations occur, the stress invariant, J, is required:

$$J^2 = \tfrac{3}{2}\xi^{*\alpha\beta}\xi^{*\alpha\beta} \tag{4.11}$$

where $\xi^{*\alpha\beta} = \tau^{*\alpha\beta} - \alpha^{\alpha\beta}$

$\alpha^{\alpha\beta}$ being the center of the yield surface. In the isotropic hardening case, $\alpha^{\alpha\beta}$ is constant and equal to zero, in the kinematic hardening case, $\alpha^{\alpha\beta}$ is updated at each time step by:

$$\alpha^{\alpha\beta\,n+1} = \alpha^{\alpha\beta\,n} + \frac{(1-\beta)E_p \Delta\varepsilon_{eff}^{p}}{J}\xi^{*\alpha\beta} \tag{4.12}$$

β hardening parameter (1:isotropic, 0:kinematic)

E_p plastic hardening modulus, depends on the elastic and tangent modulus

$$E_p = \frac{E_t E}{E - E_t} \tag{4.13}$$

$\Delta\varepsilon_{eff}^{p}$ increment of the effective plastic strain

$$\Delta\varepsilon_{eff}^{p} = \frac{J - \sigma_y}{3G + E_p} \tag{4.14}$$

σ_y yield stress, which needs to be updated, unless the isotropic hardening is used, according to:

$$\sigma_y^{n+1} = \sigma_y + \beta E_p \varepsilon_{eff}^{p\ n} \tag{4.15}$$

Plastic deformations occur when the yield function, ϕ, is greater than zero. The Von-Mises yield function is used here and given by:

$$\phi = J^2 - \sigma_y^2 \tag{4.16}$$

When that is the case, the deviatoric stresses are scaled back to the yield surface using:

$$\tau^{\alpha\beta\, n+1} = \tau^{*\alpha\beta\, n} - \frac{3G\Delta\varepsilon_{eff}^{p}}{J}\xi^{*\alpha\beta} \tag{4.17}$$

The algorithm required to evaluate the deviatoric stresses at a particle *i* for one time step can be summarized as follow:

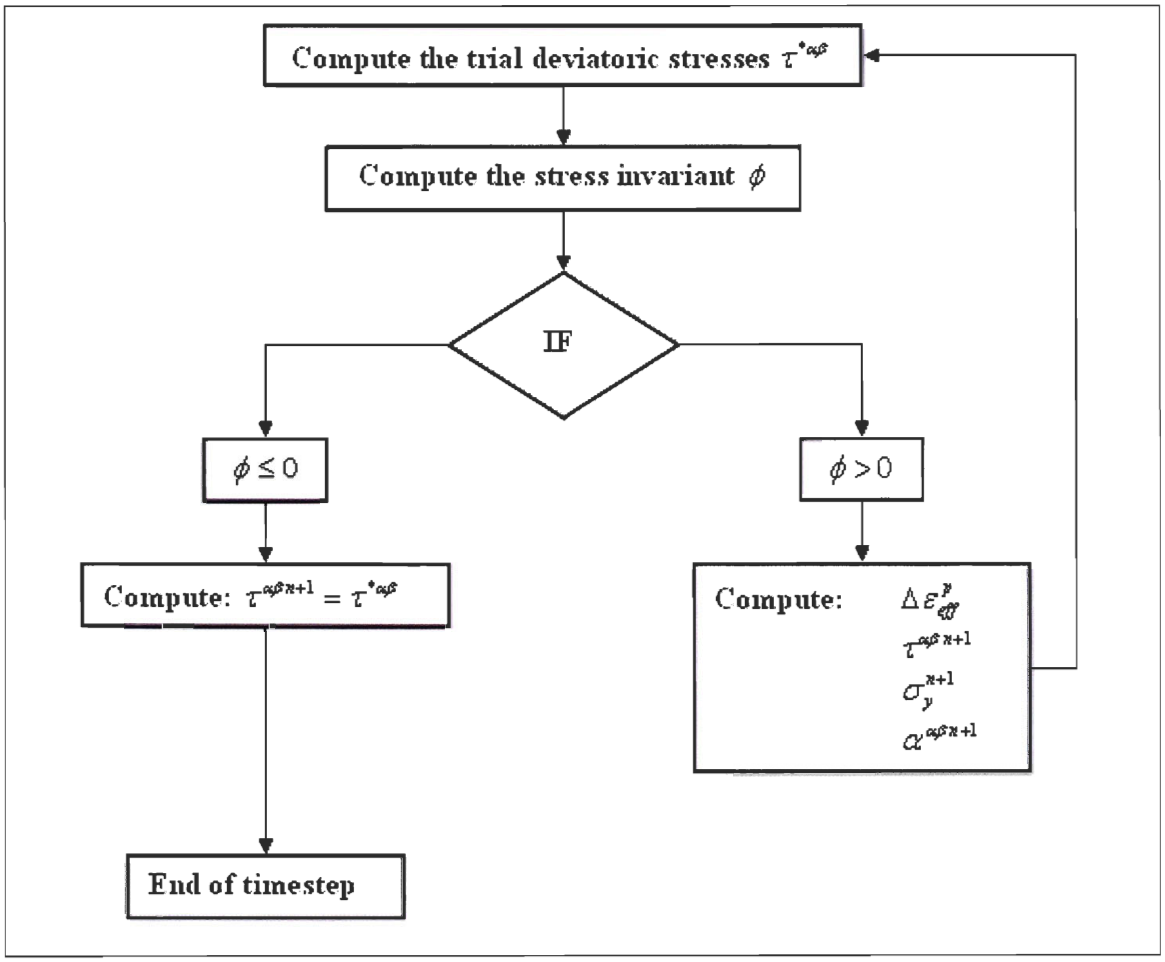

Figure 4.1 Algorithm for plastic material model with hardening

The deviatoric stresses are then returned to the main program. Note that the SPH approximation is used to evaluate the trial stresses, but it is not used to calculate the plastic strain or to scale the deviaoric stresses when plastic hardening occurs.

4.4 Johnson-Cook Material Model

In the Johnson-Cook material model, the yield stress is updated using the following equation instead of equation (4.15) for the elastic-plastic material model:

$$\sigma_y = \left(A + B\bar{\varepsilon}^{p^n}\right)\left(1 + C\ln\dot{\varepsilon}^*\right)\left(1 - T^{*m}\right) \tag{4.18}$$

where A, B, C, n, and m are material constants and:

$\bar{\varepsilon}^p$: effective plastic strain

$\dot{\varepsilon}^* = \dfrac{\dot{\bar{\varepsilon}}^p}{\dot{\varepsilon}_0}$ effective plastic strain rate for $\dot{\varepsilon}_0 = 1\,\mathrm{s}^{-1}$

$$T^* = \frac{T - T_{\text{room}}}{T_{\text{melt}} - T_{\text{room}}}$$

Otherwise, the algorithm of Figure 4.1 can be used to solve the Johnson-Cook material model. Some of the constants can be found in Johnson [92] for ARMCO iron and copper.

4.5 Elastic-Plastic-Hydrodynamic Material Model

The elastic-plastic hydrodynamic material model also follows the algorithm presented in Figure 4.1 for the elastic-plastic material model, except that the deviatoric stresses are now evaluated with:

$$\tau^{\alpha\beta\,n+1} = \frac{\sigma_y}{J}\tau^{*\alpha\beta\,n+1} \tag{4.19}$$

where each unknown can be calculated according to the equations found in Section 4.3.

Note that it is no longer required to consider the hardening phenomenon or to update the center of the yield surface and that the pressure component continues to be evaluated with the equation of state chosen such as the Mie-Gruneisen or polynomial equation of state. The parameters of the equation of state will allow for the material to behave as a solid at low stresses, and as a fluid at high stresses, such as for the bird impact simulation. If desired, a cut-off pressure can be used so that the material works in compression and not in tension. This is accomplished by re-setting the pressure from the EOS to zero if it becomes negative. In cases where the cut-off pressure is used, then the algorithm should evaluate the

stresses with the equations for a fluid when the pressure drops below zero since it will signifies that the material model is acting in the hydrodynamic range.

4.6 Examples of Application

Below are given two examples that demonstrate that it is possible to obtain plausible results even if a solid material is use with the SPH method. The first example is the Taylor impact and is compared with available experimental results. The second example is the bird impact, and the deformations and deceleration are compared with the experimental results.

4.6.1 Application to Taylor Impact

The Taylor impact, also called the rod impact, is a two-dimensional sample problem where a cylinder of dimension 25.4 mm×7.6 mm impacts on a rigid surface at a velocity of 221 m/s. The cylinder is made of iron and sustains plastic deformations. It is thus well suited example to evaluate the elastic-plastic and Johnson-Cook material models in the developed in-house SPH code. Johnson [92] provides experimental data to validate the results.

The numerical simulation uses 1380 SPH particles and 270 boundary particles. The kinematic hardening scheme is used with a Mie-Gruneisen equation of state and the simulation is allowed to run for 50 μs. The initial particle distribution is illustrated in Figure 4.2 and the material properties used for the material models and equation of state of iron are given in Table 4.1.

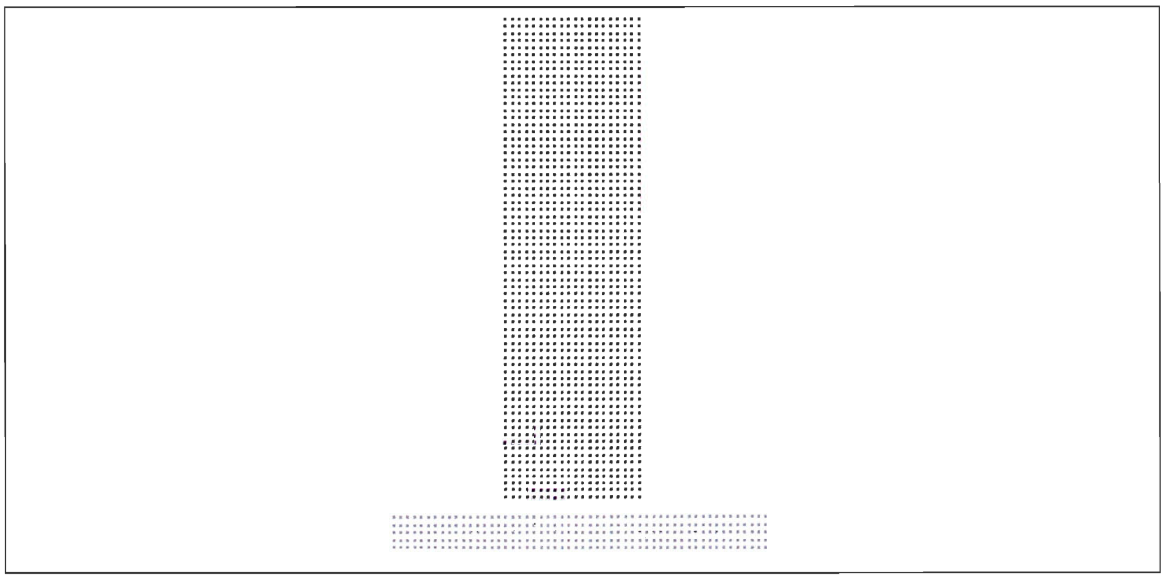

Figure 4.2 Initial distribution of particles for the Taylor impact

Table 4.1 Material's properties of ARMCO iron

Physical properties		**Johnson-Cook parameters**		**Mie-Gruneisen constants**	
Young modulus	210 GPa	A	175 MPa	Sound speed	3600 m/s
Poisson's ratio	0.30	B	380 MPa	Gruneisen coefficient	1.81
Yield strength	500 MPa	N	0.32	Volume correction coefficient	0.00
Hardening modulus	0.10 GPa	C	0.060	S_1	1.80
Density	7850 kg/m^3	m	--	S_2	0.00
				S_3	0.00

The three solid material models presented earlier in the chapter are used with the iron material and the results are compared in Figure 4.3 at three different times in the analysis. The times are 12.5, 25.0, and 37.5 μs representing 25%, 50%, and 75% of the total duration of the simulation.

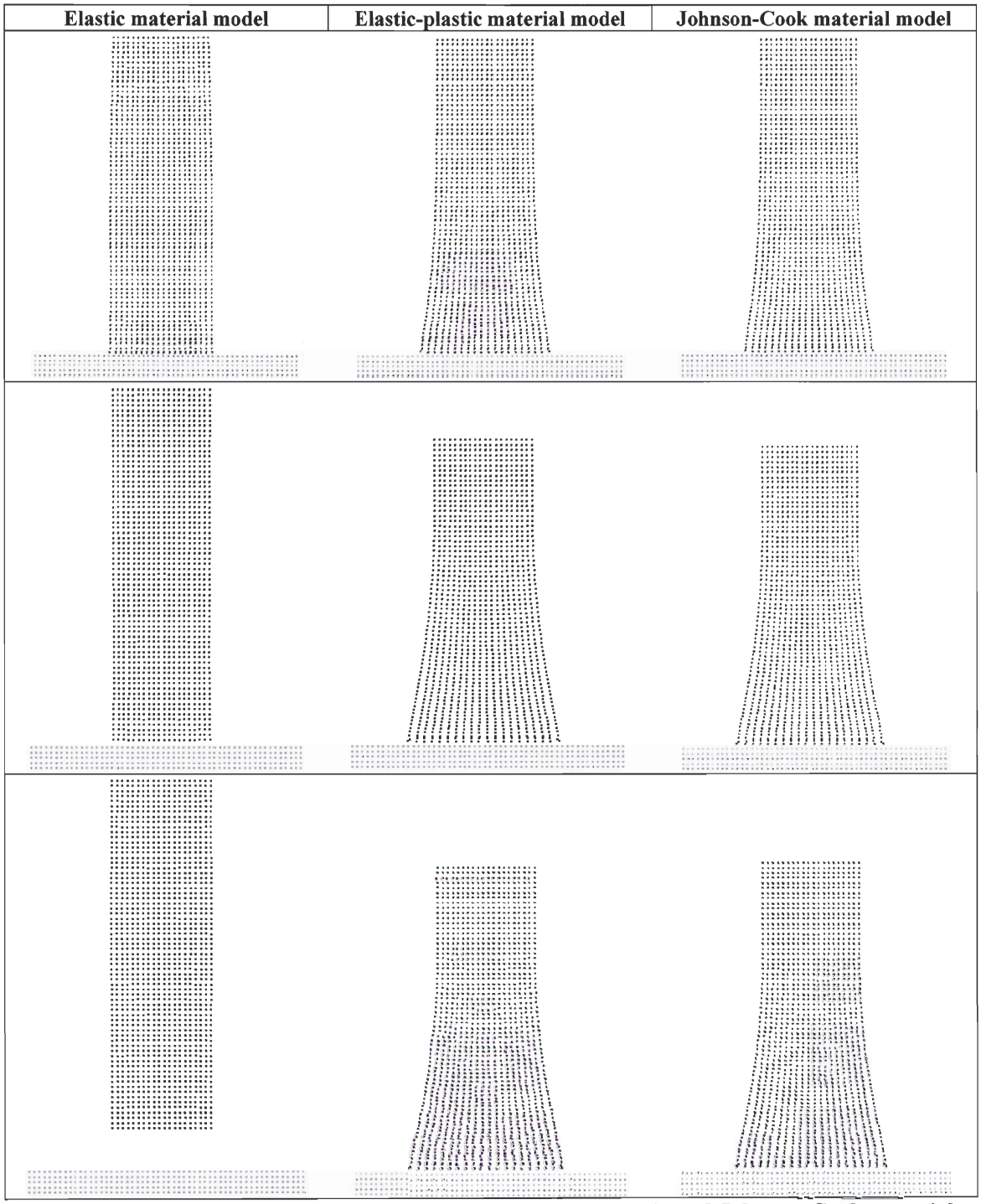

Figure 4.3 **Taylor impact example with elastic, elastic-plastic and Johnson-Cook material models**

As expected, the energy of the elastic material model is fully restored and there are no permanent deformations.

The results for the elastic-plastic and Johnson-Cook material models are very similar visually. Thus, it is easier to evaluate the results of the different solutions by computing the error, Δ:

$$\Delta = \frac{1}{3}\left(\frac{|\Delta L|}{L_{test}} + \frac{|\Delta D|}{D_{test}} + \frac{|\Delta W|}{W_{test}}\right) \tag{4.20}$$

where W is the width of the rod measured from the base at 20% of the initial height. The measurements are illustrated in Figure 4.4.

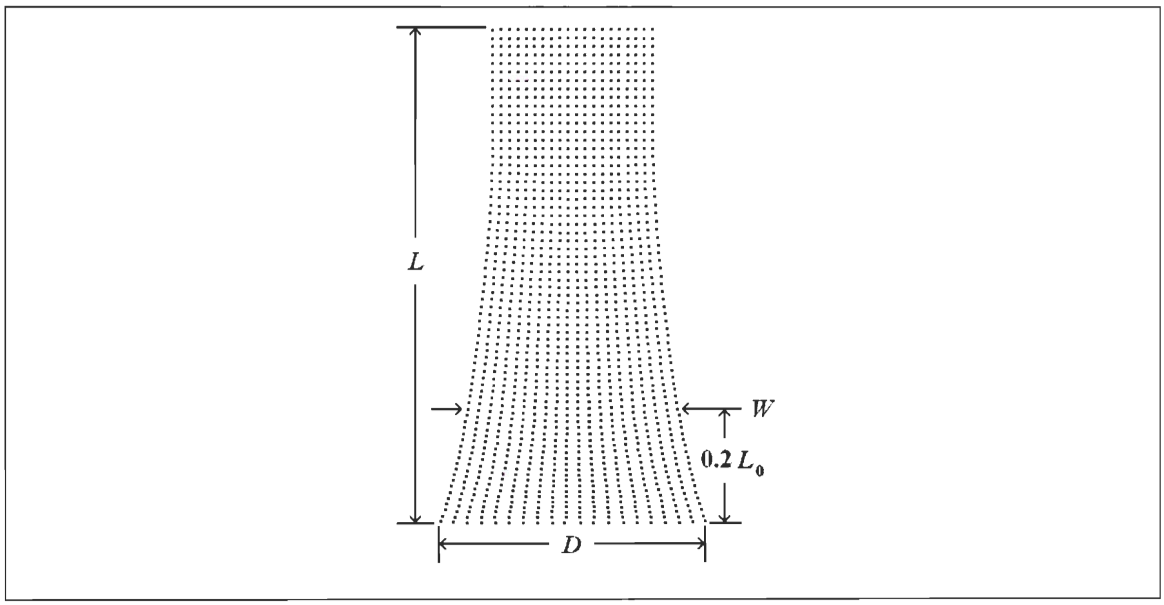

Figure 4.4 Final deformations for the Taylor impact with ARMCO iron

The error is computed for the elastic-plastic and Johnson-Cook material models in Table 4.2 and the results using the normalization and boundary correction scheme are also computed. The best results are illustrated in Figure 4.4 above and obtained when the normalization is applied to the Johnson-Cook material model.

Table 4.2 Results' summary for the Taylor impact with iron

	Length [mm]	Diameter [mm]	Width [mm]	Δ
Test [92]	19.8	13.7	8.8	--
Elastic-plastic	22.0	11.2	9.4	12.0%
Elastic-plastic with boundary correction	22.2	10.7	9.3	13.3%
Elastic-plastic with normalization	22.0	11.7	9.3	10.3%
Johnson-Cook	22.4	11.3	9.5	12.8%
Johnson-Cook with boundary correction	21.8	10.7	9.5	13.1%
Johnson-Cook with normalization	21.6	11.8	9.4	10.0%

The error between the SPH approximation and the tests results varies between 10 to 13%. The normalization correction is efficient in reducing the error because it helps keeping the particles distribution even. On the other hand, the boundary correction function tends to increase the error because, although it has a small influence as explained in Section 3.6.2 for the dam collapse example, the repulsive forces preventing the rod to slide sideways are amplified. Moreover, using the boundary correction equation given by Kulasegaram [79] did not affect the results, so the equation itself is not the issue, but rather the overall effect benefit of the correction is very small. More details will be given regarding that aspect in Chapter 5 when additional boundary interaction schemes will be discussed.

The difference between using the regular algorithm and applying the normalization is illustrated for the elastic-plastic material model in Figure 4.5. The particles distribution is also smoother when the normalization is used.

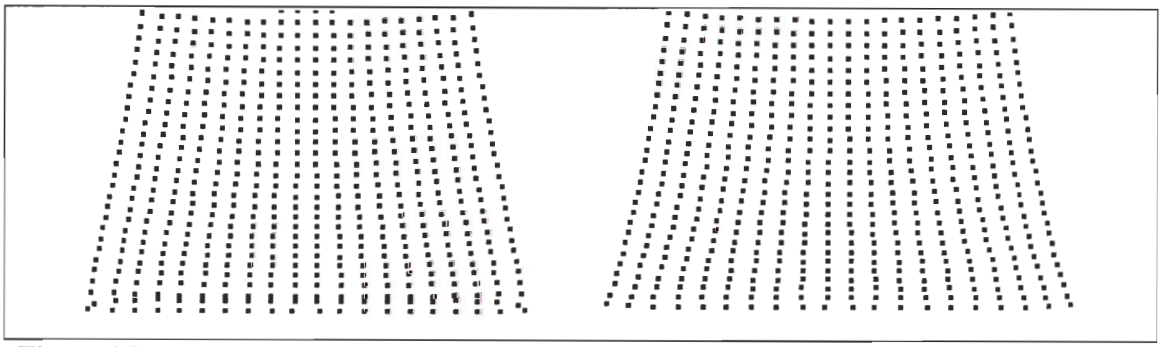

Figure 4.5 Particles' distribution without (left) and with (right) normalization

Although there is room for improvement, the results are now acceptable and within the range of the experimental results. Moreover, the contact used to regulate the interaction between the projectile and target has much influence on the accuracy of the results, which will be demonstrated in the next chapter.

4.6.2 Bird Impact

The bird impact uses the same geometry as the bird described in Section 1.4.3. Approximately 4,500 particles are used to represent the bird, and 3,500 particles represent the rigid wall. For the time being, the modelling of the target is kept simple and the ledge is not modelled. The bird impacts the target at a velocity of 95 m/s, so that the deceleration of the end of the bird and its spread on the target can be compared with the experimental results. The in-house SPH algorithm uses the normalization scheme and the artificial viscosity with the polynomial equation of state.

At this point, it is not possible to retrieve the pressure applied by the bird onto the target, so the results are analyzed in terms of deformations. The deformations sustained by the bird through the impact are shown in Figure 4.6 and are compared with the results from the numerical simulations. What is observed is consistent with previous SPH simulations in LS-DYNA, the main difference resides in how the bird seems to decelerate faster in the in-house code. This observation can also be made when looking at Figure 4.7 and Figure 4.8 where the deceleration happens earlier in the simulation and the diameter increase is more important. The results for the three experimental tests are used in Figure 4.7 and Figure 4.8.

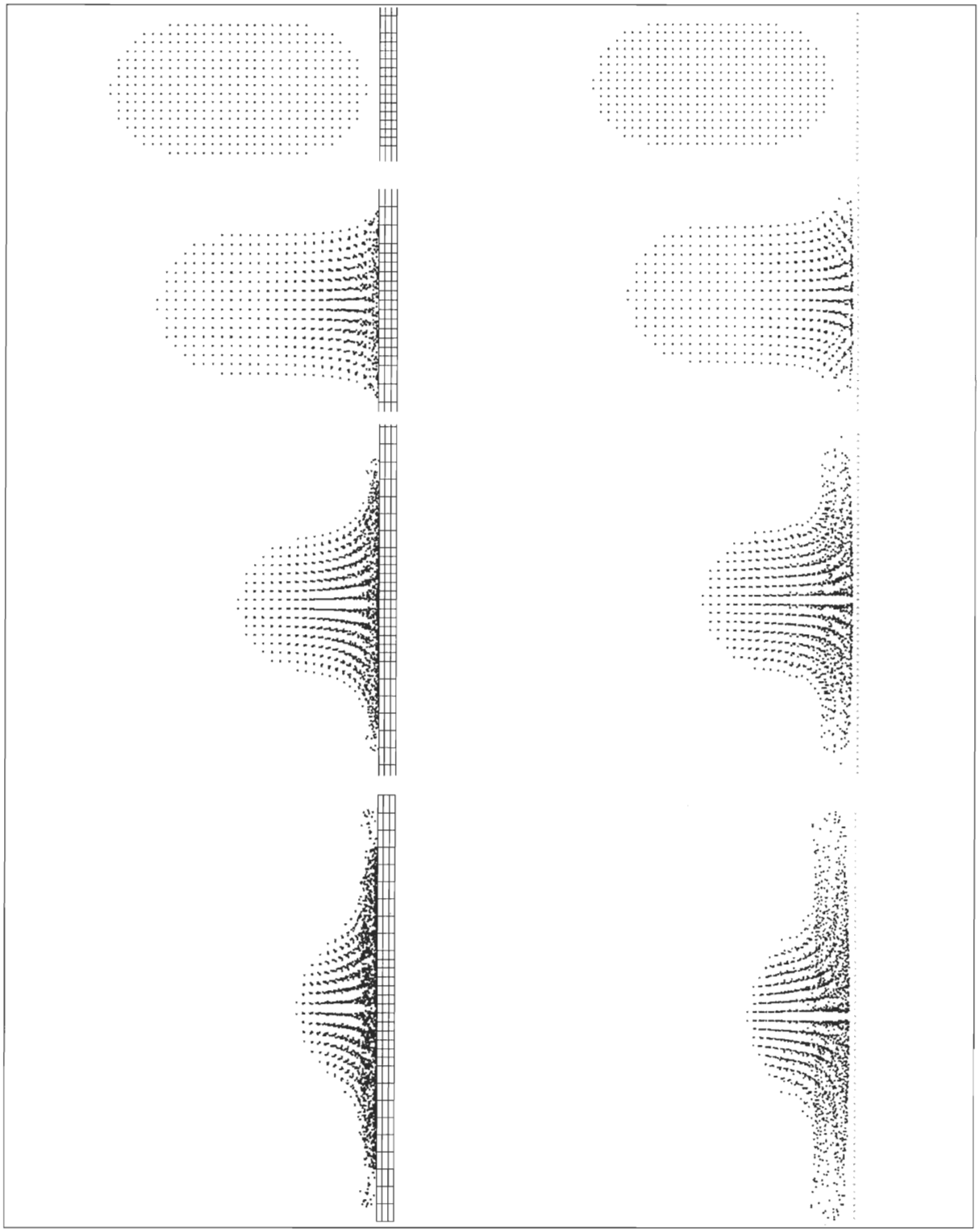

Figure 4.6 **Bird deformations at 0.0000, 0.0005, 0.0010, and 0.0015 s for LS-DYNA (left) vs. in-house code (right)**

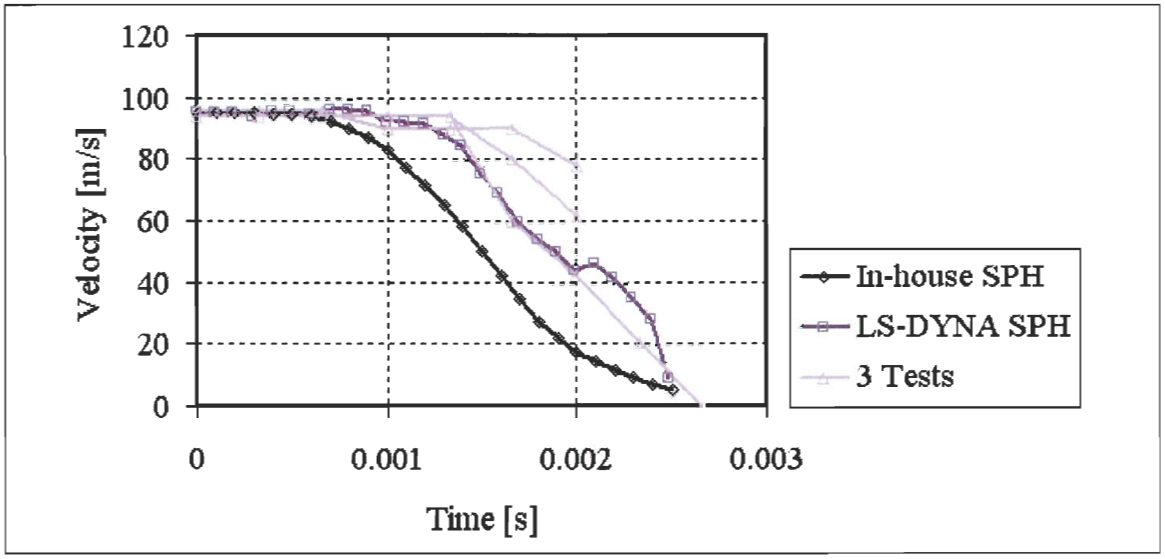

Figure 4.7 Deceleration of the bird

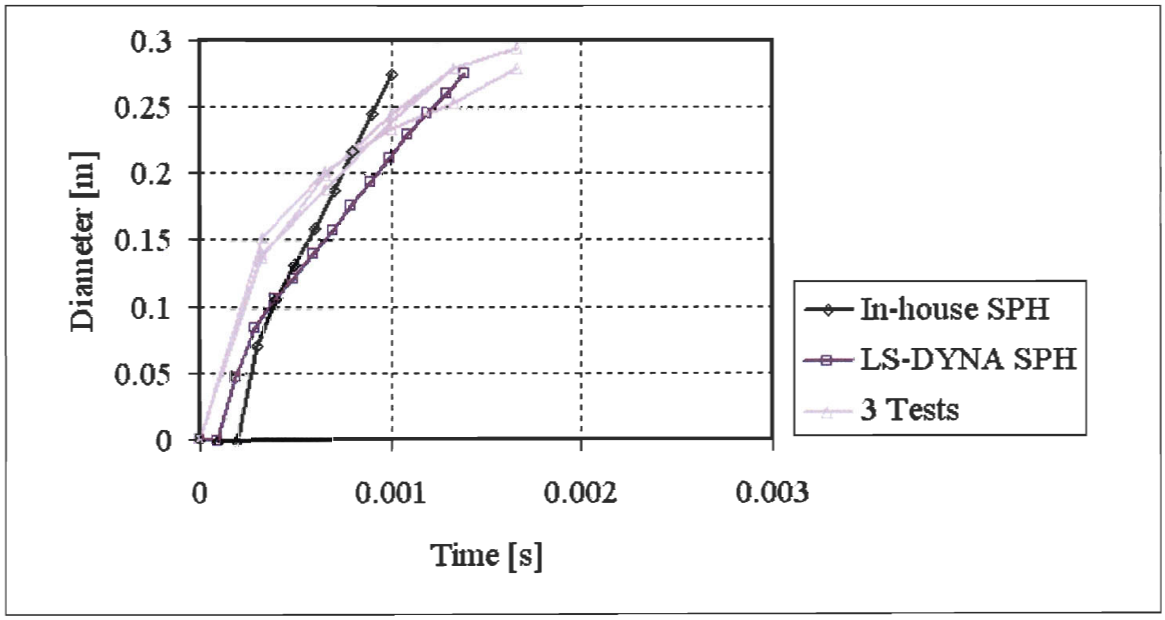

Figure 4.8 Increase of the diameter of the bird

At present, the explanation proposed for those differences is two fold. First, the external forces are used to repel the particles from the target. As mentioned and demonstrated in the following chapter, the repulsive forces are not proportional to the magnitude of the impact. However, because the amount of particles required to solve the example using a different boundary interaction would almost double and make the analysis very heavy to run, it was decided that for the time being the external forces would be sufficient. Another explanation

is the inconsistency in the domain near the boundary. The normalization scheme addresses that problem, but may not be able to entirely resolve it when the particle distribution is uneven and changes quickly in time. Thus there can be a loss of velocity near the boundary.

For the time being, it is satisfying to know that the SPH algorithm developed is able to treat a problem using a soft body material. Further investigation of the options used and boundary interaction scheme would likely improve the results.

4.7 Conclusions

Four additional material models have been implemented in this chapter. They are the elastic, the elastic-plastic, the Johnson-Cook and the elastic-plastic hydrodynamic models. The evaluation of the implemented materials models indicates that they are computationally stable and accurate.

In the Taylor impact example, both material model that can simulate plastic deformations work well and yield similar results. The normalization scheme allowed decreasing the error with respect to the experimental results to 10%. The boundary correction function was not successful in improving the results. It is possible that the example would yield better results if it was developed in three dimensions since the axisymmetry would be preserved. Thoughts have been given to that approach, but the two dimensional approach is less expensive to run from a computational point of view which makes it easier to compare the results using different options.

The fourth material model presented, the elastic-plastic hydrodynamic, was used to solve the bird impact problem. The in-house program was able to solve the example easily with no instability. The results are slightly different than the experimental values found in Chapter 2, but then again not all the features of the target were modeled and the external forces were used. It is important to note that the algorithm itself worked well.

The examples given in this chapter show that the SPH formulation developed so far is stable enough to be applied to problems other than fluids. Since most engineering applications involve solids, this represents an advantage in promoting the use of SPH.

5 Boundary Interaction

5.1 Introduction

Another important feature of SPH that has often been neglected is the treatment of boundary conditions. Some approaches used were briefly discussed in Chapter 3 and the current chapter implements two additional approaches that are of interest. When using finite elements method, the interaction between bodies is controlled through a contact algorithm selected to suit the application. On the other hand, meshless methods are often used in applications where the boundary conditions can be neglected. However, since meshless methods are now being used in applications where the boundary conditions and the interaction with other bodies are important, the approach to model the fluid and structure interaction is becoming of interest.

Liu [42] provides two ways of controlling the interaction: symmetry, and the use of external forces, which prevent penetration of distinct bodies. The first option is limited to simple two-dimensional problems and the parameters used by the external forces are set arbitrarily and the forces generated, although sufficient to prevent penetration, are not proportional to the magnitude and direction of the relative velocity of the interacting particles.

In order to extend the possibilities of meshless methods, Vuyst [93] has done work with coupling of meshless and finite element methods. The equation presented is also defined by arbitrary parameters, but it allows a repulsive force between the SPH particles and the virtual particles attached to the nodes of the structure meshed with finite elements. Both interacting bodies can be deformable but once again, the magnitude of the force is not proportional to the magnitude of the velocity. Moreover, one can chose to represent both interacting bodies with particles.

Finally, Seo [94] has proposed a node to node contact for meshless method. This approach uses the magnitude and direction of the relative velocity of the interacting particles and the parameters used are determined based on the physical properties of the materials. Friction,

based on Li [95], has been added to the contact but the no-penetration condition is not enforced.

Other approaches such as attaching SPH particles to the finite element mesh's nodes [78] or the use of virtual particles [59,75-77] are not of interest since the purpose here is to mesh both bodies with real SPH particles. The three first ways of monitoring the interaction between bodies discussed above are of interest and have been implemented in the SPH in-house code. The implementation consists of creating additional routines to replace the current routine used to compute the external forces. The mathematical development of each is given below in Sections 5.2, 5.3, 5.4 and are followed by a few examples in Section 5.5.

5.2 External Forces

The equations for the external forces have already been given in Section 3.5.2 but are recalled here with more details. They are computed with an equation which creates repulsion from the boundary interface. The force is not a physical value, i.e. it is not related to the magnitude or direction of the velocity of the particles, but it can prevent penetration through a boundary. The equation used is the Lenard-Jones type repulsive force [42]:

$$B_i = \begin{cases} D\left[\left(\frac{r_0}{r_{ij}}\right)^{n1} - \left(\frac{r_0}{r_{ij}}\right)^{n2}\right]\frac{1}{r_{ij}^2} & \left(\frac{r_0}{r_{ij}}\right) \le 1 \\ 0 & \left(\frac{r_0}{r_{ij}}\right) > 1 \end{cases} \qquad (5.1)$$

where D, r_0, $n1$, $n2$ are arbitrary parameters determined through experience, B_i is the acceleration component to add to the particle i, and r_{ij} is the distance between particle i and the boundary j. Liu [42] gives the following guideline to determine what values can be used for the arbitrary parameters:

- n_1, n_2 are equal to 12 and 4, respectively
- D same magnitude as the square of the largest velocity
- r_0 cut off distance, close to initial particle spacing

The acceleration resulting from the boundary force is given by:

$$\frac{dv^{\alpha}_{ext\,f\,i}}{dt} = \sum_{j}^{bn} B_j x^{\alpha}_{ij} \qquad (5.2)$$

with *bn* the boundary neighbours.

The forces generated are in the direction of the $\vec{x}_{ij}$ vector, which is the vector that goes from the particle i to the particle j. Hence, the direction of the acceleration is not automatically consistent with the surfaces' relative movement.

This is illustrated in Figure 5.1 where the particles j represent a rigid boundary. Even if the particle is not approaching the boundary (v_x=0), repulsive forces in the x direction are generated.

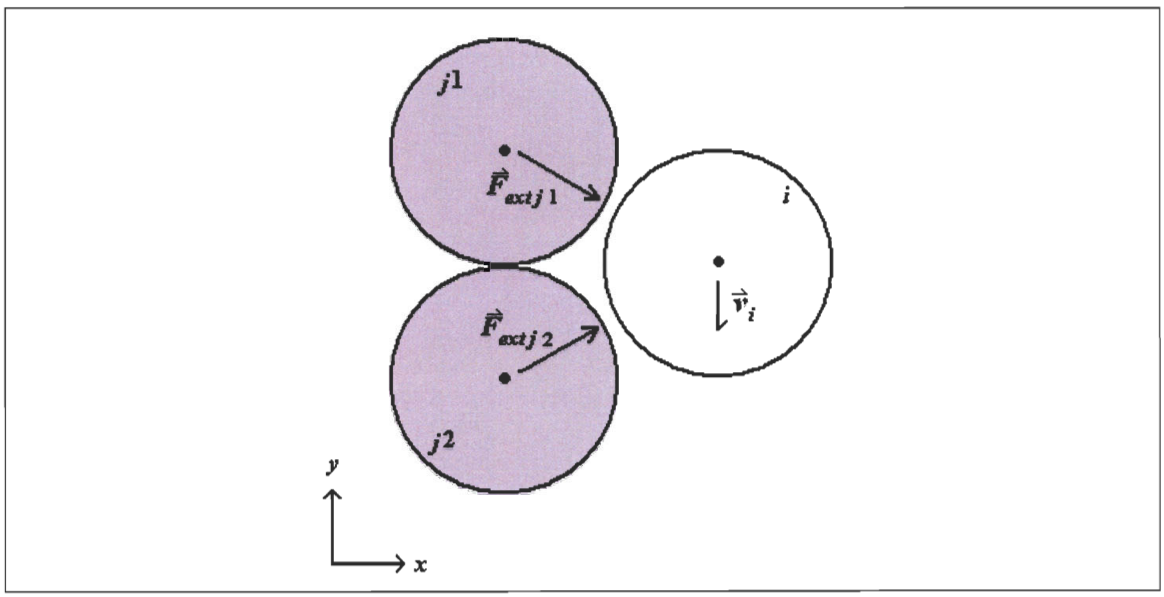

Figure 5.1 Direction of the forces generated when using the external forces

5.3 Contact Potential

The contact force is computed based on a contact potential presented by Vuyst *et al* [93]. The resulting contact force is given by:

$$f^{\alpha}_{cp\,i} = \sum_{j}^{nb} \frac{m_j}{\rho_j}\frac{m_i}{\rho_i} Kn \frac{\left(W\left(\vec{x}_{ij}\right)\right)^{n-1}}{\left(W\left(h_{ij}\right)\right)^{n}} \nabla W\left(x_{ij}\right) \qquad (5.3)$$

with K and n, user defined parameters. Given that $f = ma$, the resulting acceleration is simply:

$$\frac{dv_{cpi}^{\alpha}}{dt} = \frac{f_{cpi}^{\alpha}}{m_i} = \sum_{j}^{nb} \frac{m_j}{\rho_j} \frac{1}{\rho_i} Kn \frac{\left(W\left(x_{ij}\right)\right)^{n-1}}{\left(W\left(h_{ij}\right)\right)^{n}} \nabla W\left(x_{ij}\right) \tag{5.4}$$

The contact force is the gradient of the contact potential evaluated with the SPH approximation but overall, it is very similar to the external force. This time, the direction of the force is given by the gradient of the kernel evaluated for the two particles and when observing equation (3.30) for the gradient, the resulting force is again in the same direction as the vector $\vec{x}_{ij}$, illustrated in Figure 5.1. The general magnitude of the force created with the contact potential ends up to be similar to that for the external forces, which is logical since it has to be sufficient to prevent penetration.

5.4 Node to node contact

In order to accurately handle contact problem within an SPH algorithm, several approaches have been proposed, but the node to node contact algorithm seems one of the most efficient in this context. Seo et Min[94] has defined a node to node contact. The normal force generated can be computed as:

$$f_{ntmci}^{\alpha} = \sum_{j}^{nb} \frac{m_j}{\rho_j} \left(\lambda_1 \dot{p}_{nav} + \lambda_2 p_{nav}\right) \vec{n}_{av} W_{ij} A_i \tag{5.5}$$

where f_{ntmc} is the friction for the node to node contact

λ_1, λ_2 are physical parameters

$p_{nav}, \dot{p}_{nav}$ are the penetration and penetration rate, respectively

$\vec{n}_{av}$ is the average of the normal of both surfaces

A_i is the area in contact (in 3D, length in 2D)

The parameters are computed according to:

$$p_{nav} = \left(R_i + R_j - \left|\vec{r}_{ij} \cdot \vec{n}_{av}\right|\right) \tag{5.6}$$

$$\dot{p}_{nav} = \vec{v}_{ij} \cdot \vec{n}_{av} \tag{5.7}$$

$$\lambda_1 = \frac{\rho_j c_j \rho_i c_i}{\rho_j c_j + \rho_i c_i} \tag{5.8}$$

$$\lambda_2 = \frac{E_j E_i}{(E_j + E_i)(R_j + R_i)} \tag{5.9}$$

where R_i is the radius of the particle

$\vec{v}_{ij}$ is the relative velocity between the particles

c_i is the sound velocity in the medium

E_i is the elasticity modulus of the material

Seo et Min [93] suggests setting $E, c \to \infty$ for the case with a rigid boundary. In the formulation used, it was found that it is simpler to let the particles interact, but to set the resulting acceleration of the rigid body to zero.

To calculate the average normal between the particles, the normal of each particle is needed. The boundary is first identified by using a trial function, say ψ, and evaluating it over the domain, i.e:

$$\psi_i \neq \sum_{j=1}^{n} \psi_j \frac{m_j}{\rho_j} W_{ij} \tag{5.10}$$

If the difference between the known value of ψ and its approximation is greater than10-15% [94], then the particle i is a boundary particle. For those particles that have been identified as a boundary, the normal is found by calculating the gradient of the trial function and kernelling only for the same material:

$$\vec{n}_i = \pm \left(\frac{\nabla \psi}{|\nabla \psi|} \right)_i =, \ (\nabla \psi)_i = -\sum_{j}^{n} \psi_j \frac{m_j}{\rho_j} \nabla W_{ij} \tag{5.11}$$

Now that the boundaries can be identified, two boundary particles are said to interact if the distance $\vec{r}_{ij}$ between them is less than:

$$\left| \vec{r}_{ij} \right| \leq \sqrt{\max(R_i, R_j)^2 + (R_i + R_j)^2} \tag{5.12}$$

The criterion given takes into account lateral offsets and unequal radii of approaching particles.

If contact between two particles occurs, then the average normal vector is calculated according to the algorithm of Figure 5.2 where θ denotes angle formed with the normal vector of particle i and that of particle j.

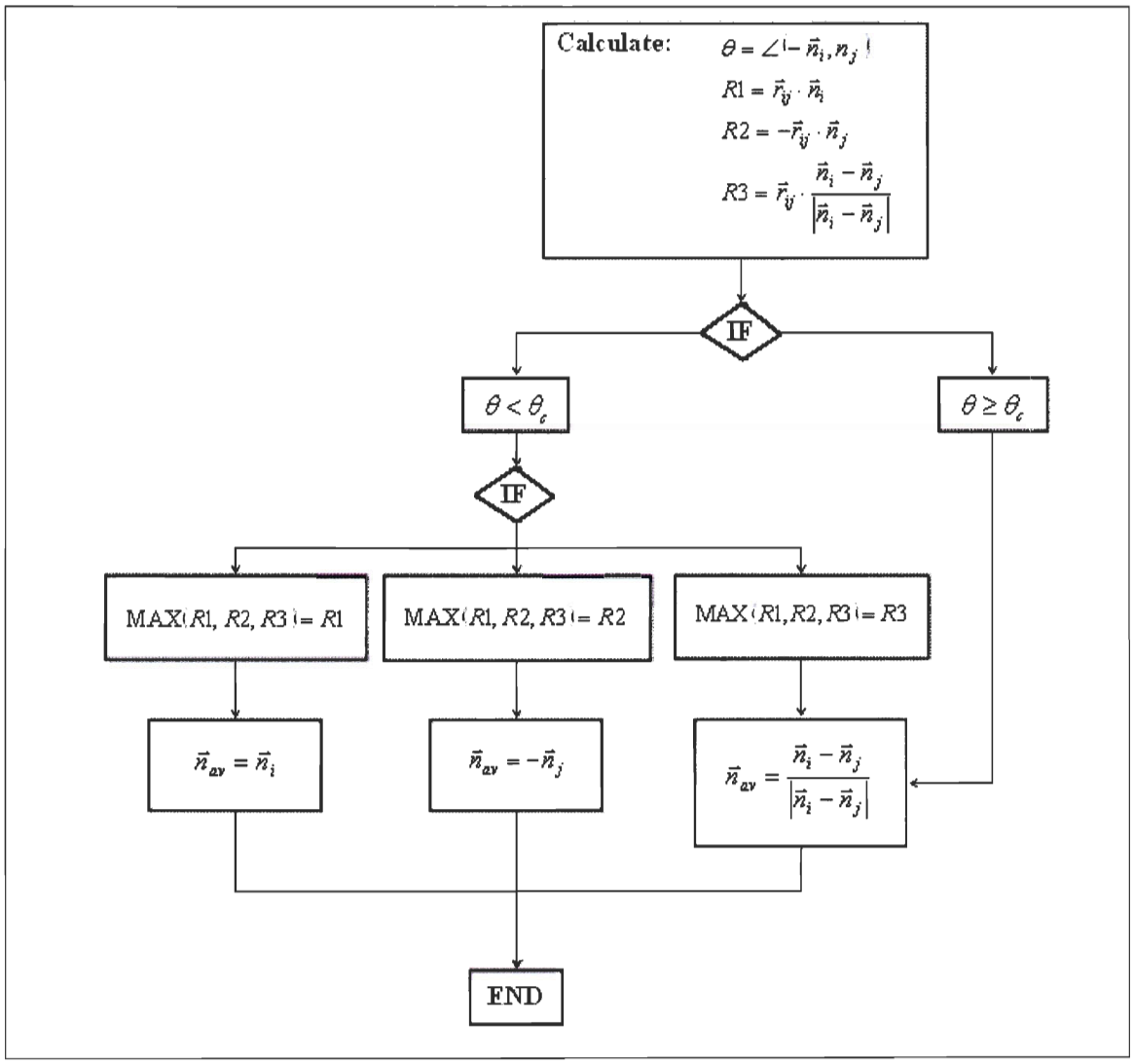

Figure 5.2 Flowchart of the algorithm to calculate the boundary's normal

Now, friction can be added to the contact force. In this instance, the Coulomb formulation with sliding is chosen. It is a common formulation found in literature and available in commercial finite elements software [32,33,95]. The algorithm of Figure 5.3 is applied.

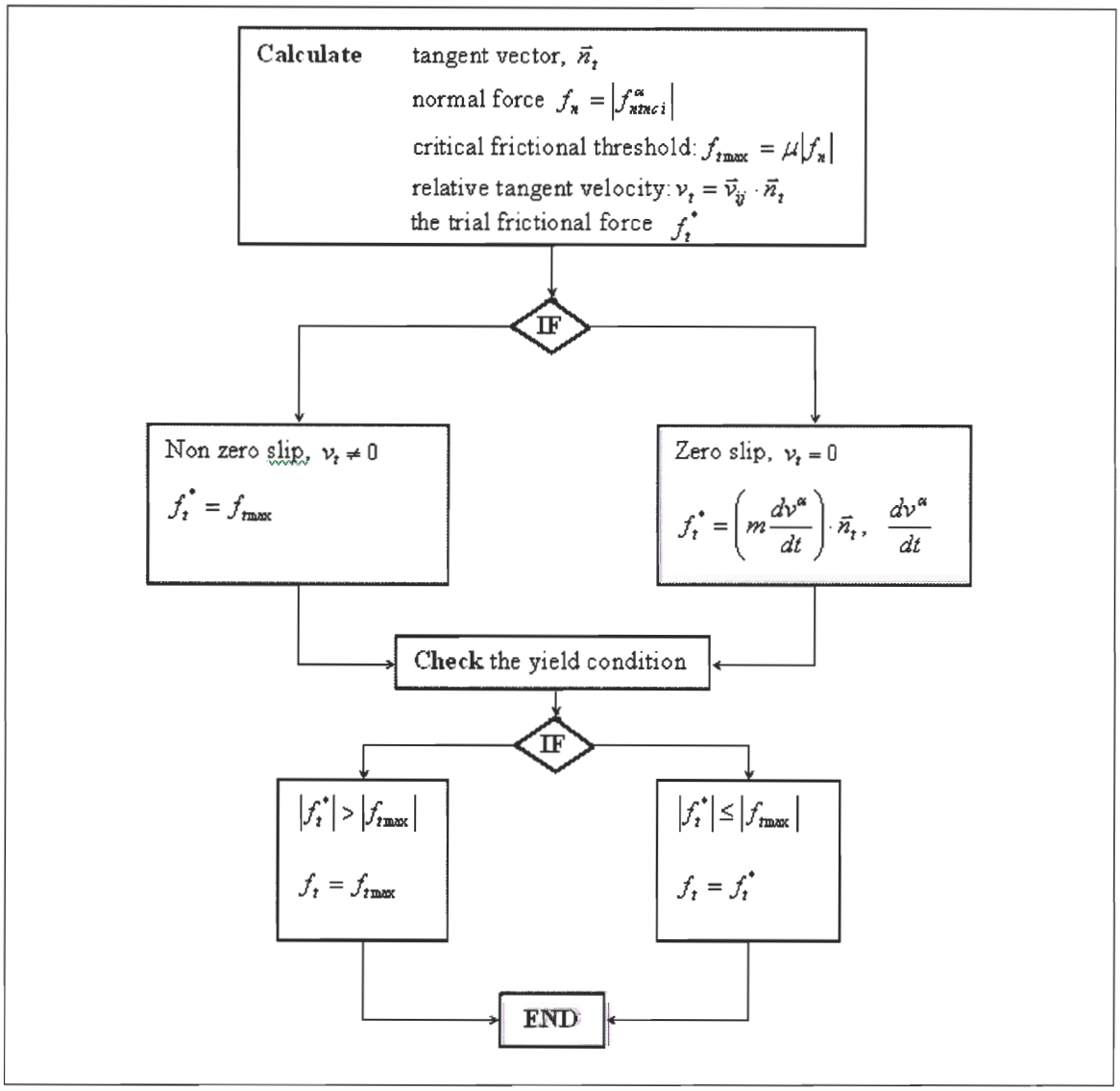

Figure 5.3 Friction algorithm

The total acceleration due to the contact is given by:

$$\frac{dv_i^{\alpha}}{dt} = \frac{f_{total\,i}}{m_i} = \frac{1}{m_i}\left(f_{ntnci} + f_{ti}\right) \tag{5.13}$$

where f_t is the frictional contact force

The forces generated with the node to node algorithm are an improvement because the normals and velocities of both interacting bodies are taken into account. For instance, if the

node to node contact was applied to the situation illustrated in Figure 5.1, there would be no forces generated.

5.5 Examples of Application

Two of the examples given in Chapter 3 and 4 are revisited to investigate the influence of the boundary interaction approach selected. The first example is the dam collapse of Section 3.6.2 where it is easy to observe how the boundary forces interact with the column of fluid. In the second example, the contact options are all used with the best case scenario of the Taylor impact described in Section 4.6.1 to see if the results can be improved.

5.5.1 Dam Collapse

The details of the dam collapse example were given in Section 3.6.2. The example is used here to illustrate how each described boundary force works in relation with Figure 5.1. This provides a better understanding of how the boundary forces are generated for each of the three boundary interaction.

As the column of water collapse under the effect of gravity, the particles' velocity in the vertical direction increases and the particles close to the vertical boundary should slide along the boundary, since there is no velocity component parallel to the boundary's normal. However, when observing the early stages of the simulation with the external forces or the contact potential, both methods create a repulsive force from the boundary. The parameters of the external forces are r_0= 1.2e-3, D = 1.0, n_1 = 12, and n_2 = 4 are sufficient to prevent the penetration of the column of fluid into the boundary. The constants for the contact potential are K = 1.0e+7, n = 5.0 which are necessary to prevent penetration into the boundary. In Figure 5.4 it can be observed that the column of fluid is repelled by the boundary early in the simulation, at time 0.01 sec.

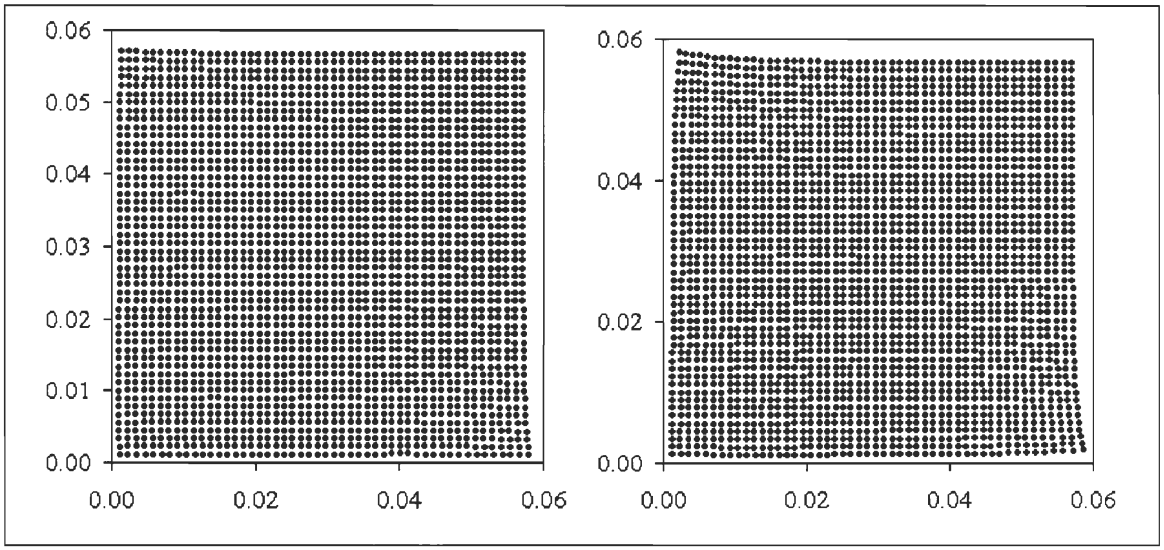

Figure 5.4 **Particles' distribution with the external forces (left) and the contact potential (right) at time 0.01 sec**

On the other hand, that problem is not observed when the node to node contact is activated. This can be observed by comparing with Figure 5.5 where the nodes remain close to the boundary.

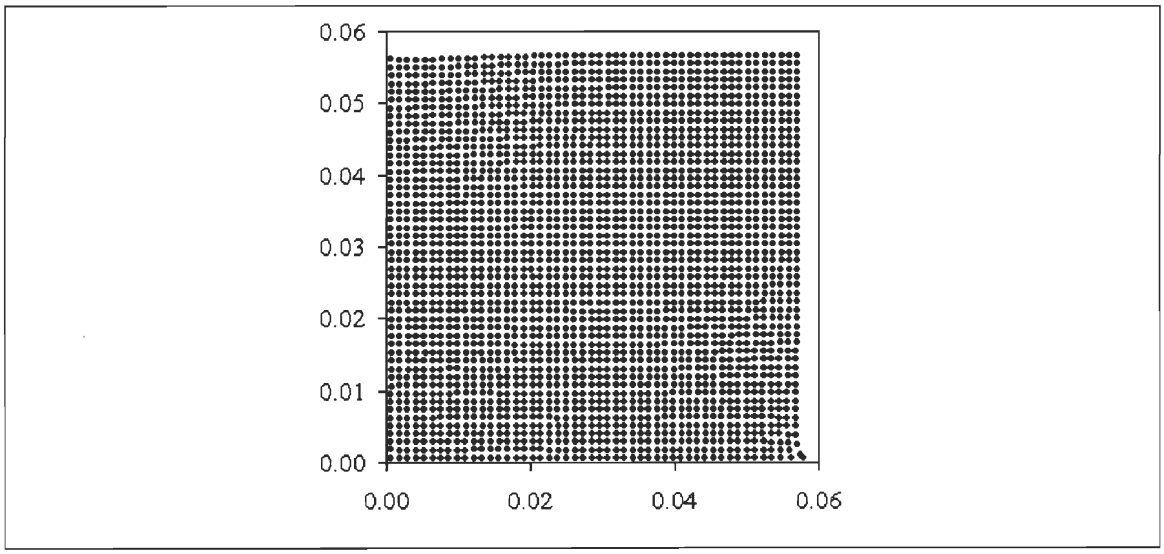

Figure 5.5 **Particles' distribution with the node to node contact at time 0.01 sec**

It was however impossible to compare the final results for the different boundary interaction schemes. This is mainly attributed to the fact that the particles' movement make it difficult to identify the boundary of the column of water using the algorithm presented in

Figure 5.2. Thus, especially for situation with fluids, the external force approach might be better suited, at least until a different scheme is used to identify the boundary.

5.5.2 Taylor Impact

The different boundary interaction schemes have been applied to the best solution of the Taylor impact presented in Chapter 4. That solution was obtained with using the Johnson-Cook material model in conjunction with the normalization scheme. The parameters for the external force were of r_0= 1.0e-3, D = 1.0, n_1 = 12, n_2 = 4.

When the contact potential is used, K and n are set to 1.0e+16 and 2.0, respectively, for the interaction to properly occur and prevent penetration. The final deformations obtained are very similar to the external forces and although the contact potential offers more possibilities, it does not represent a major improvement for this application.

As for the node to node contact algorithm, the only parameter to input is the friction coefficient. Without friction, the error decreases to 6.4%. Friction limits the amount of sideway sliding of the rod on the target. The physical value for the iron to iron static friction coefficient is of 0.16 if the contact is lubricated [96]. It is safe to assume that the dynamic coefficient for well lubricated surface with a smooth finish is lower than that value for the static coefficient, so a value of 0.02 was selected in the simulation efforts with taking into account the friction. The difference in the results was less than 0.5%.

The final deformations for the three scenarios, external forces, contact potential and frictionless node to node contact, at time 0.5 ms are illustrated in Figure 5.6. The error is computed in Table 5.1 with the help of equation (4.19).

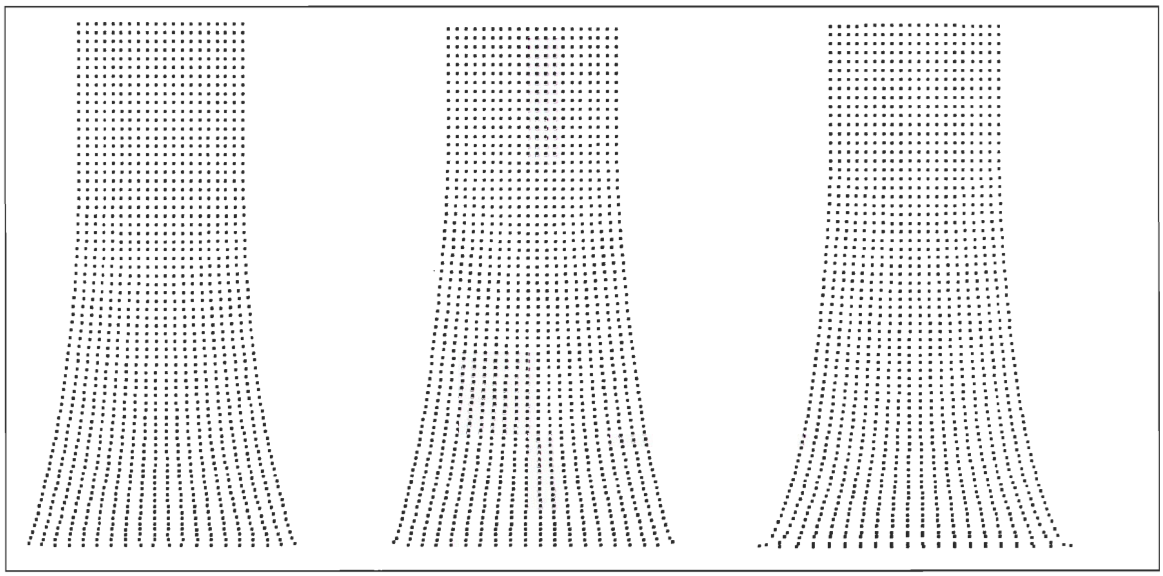

Figure 5.6 **From left to right: final deformations with external forces, contact potential, and frictionless node to node contact**

Table 5.1 **Results obtained for the Taylor impact with iron and different contact**

	Length [mm]	Diameter [mm]	Width [mm]	Δ (error)
Test [92]	19.8	13.7	8.8	--
External forces	21.6	11.8	9.4	10.0%
Contact potential	21.5	11.9	9.5	10.0%
Frictionless node to node contact	21.5	13.1	9.4	6.4%
Node to node contact with friction	21.5	12.7	9.2	6.9%

The Taylor impact was then applied to the same example but using copper instead of ARMCO iron. All the parameters remain the same, except for the physical properties of the material which are listed in Table 5.2. In this case the use of friction did not have a significant impact on the results.

Table 5.2 Material properties of copper

Physical properties		**Johnson-Cook parameters**		**Mie-Gruneisen constants**	
Young modulus	117 GPa	A	90 MPa	Sound speed	3900 m/s
Poisson's ratio	0.35	B	292 MPa	Gruneisen coefficient	2.00
Yield strength	400 MPa	N	0.31	Volume correction coefficient	0.00
Hardening modulus	0.10 GPa	C	0.025	S_1	1.50
Density	8930 kg/m^3	m	--	S_2	0.00
				S_3	0.00

Similar results are obtained when using copper instead of iron for the Taylor impact. The experimental values for the height, diameter and width are respectively of 18.2, 13.5, and 10.0 mm [92]. The minimal error is of 5.5%, and is obtained when using the normalization scheme with the Johnson-Cook material model where the height, diameter and width measured are of 19.9, 13.9, and 10.5 mm respectively. The final deformations for the best case scenario are shown in Figure 5.7.

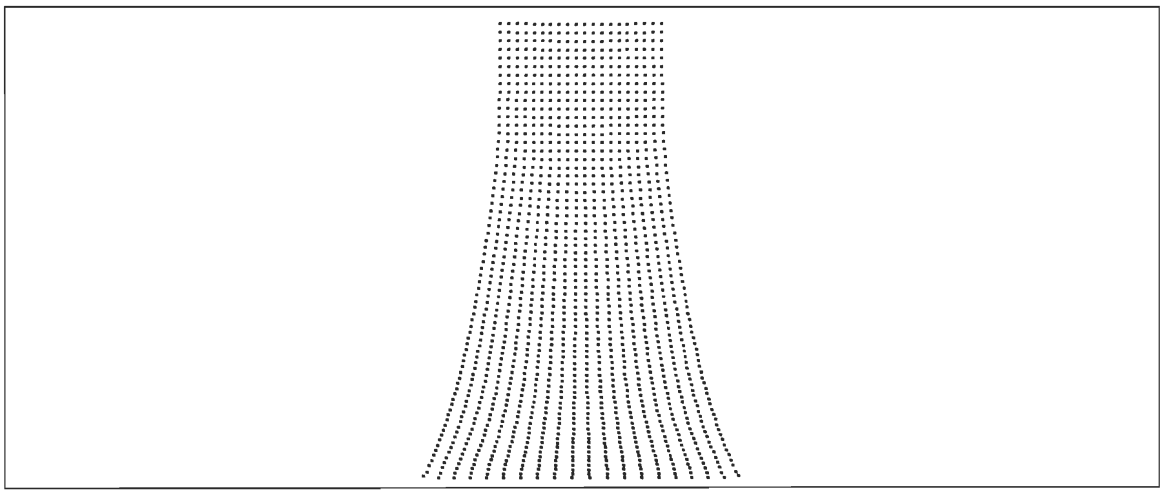

Figure 5.7 Final deformations for the Taylor impact when using copper

Finally, although there is no experimental data to compare it with, the ARMCO iron rod was impacted against a deformable target. The final deformations given in Figure 5.8 show

that the algorithm is able to handle problems where both bodies are deformable. The node to node contact was used here and the target has the same material properties as the impacting rod.

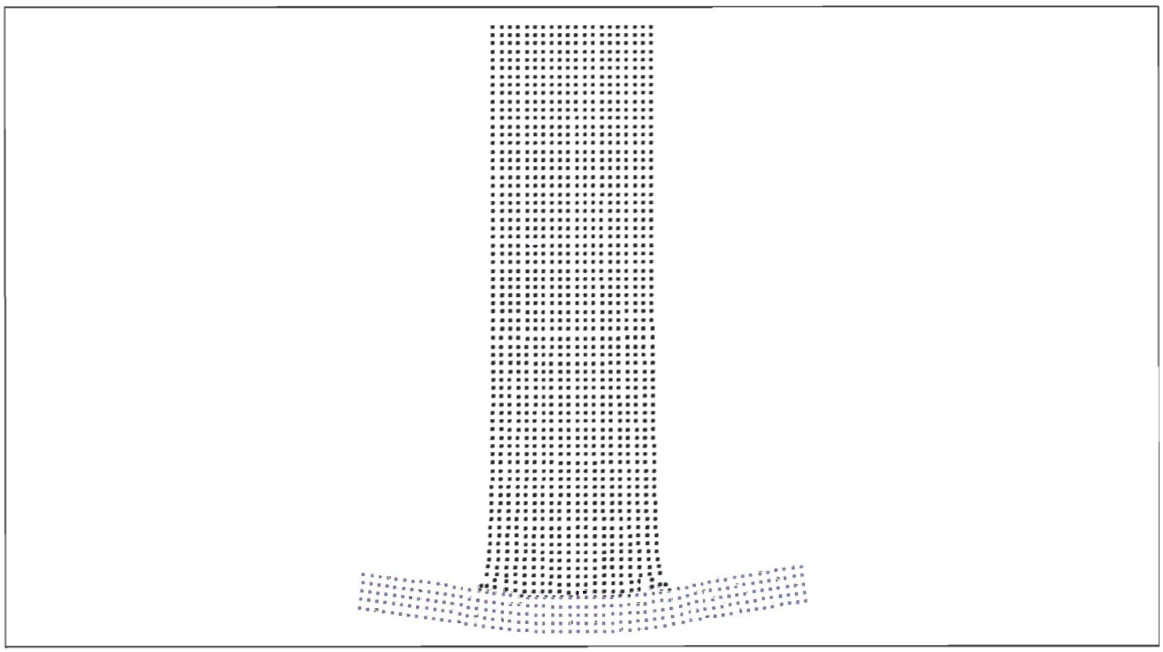

Figure 5.8 Deformations obtained with a flexible target

5.6 Conclusions

The treatment of boundary conditions has been described in this chapter. Three approaches have been investigated: the external forces, the contact potential, and the node to node contact.

The use of contact potential and of the node to node contact algorithm is an improvement with respect to the external forces because forces can be exchanged between two bodies. The choice of the boundary interaction scheme may depend on the application at hand. Still, the dam example shows how there are no repulsive forces generated unless it is required, i.e. the particles are approaching the boundary for the node to node contact. In the Taylor impact example, the node to node contact reduces the observed error.

The above examples have shown that by understanding how each boundary interaction approach works, one can make a better decision when it comes to using one of them.

Moreover, although for the considered example, the friction in the node to node contact did not play a crucial role as far as accuracy went, it can be very useful in other applications.

Future works would be to develop examples where both bodies are deformable and compare the results to available experimental results. The considered solid mechanics examples involve moderate large deformation and use of Eulerian kernels. However recent works [55] indicate that in order to correctly simulate very large deformations, use of Lagrangian kernels either in total or updated lagrangian formulation is required. This has to be introduced in our in-house SPH software as a future development for more flexibility in the range of problems that can be handled in practice.

6 General Conclusions

In the first part of the thesis, the numerical bird modeling methods have been compared against each other with respect to theoretical and experimental values. The ALE and SPH models came out as the strongest numerical methods as opposed to the traditional Lagrangian approach. They also compared well with the theoretical predictions. The presented paper gives an updated and reliable literature review of bird modeling techniques in use up to this day. It also provides guidelines to evaluate bird modeling based on six criteria which relate to the pressure applied to the structure and the deformations of the projectile.

Since it was obvious from the bird impact modeling literature review that new tests data were required, tests took place which led to the development of a recipe for developing the gelatine bird substitute. The recipe is easy to make and will hopefully encourage others to share theirs so that the certification procedure includes clear guidelines as to the projectile to use, other than a real bird.

As for the results, the deformations of the bird substitute were well captured by the video camera, and the numerical simulations compared very well with those results. The pressure results proved more difficult to analyse. The trend of the pressure read was in agreement with the theory, but the magnitude was much higher. A calculation of the amount of energy involved in the event versus the initial kinetic energy of the projectile proved that the experimental data were not valid. Thus, numerical simulations will still rely on the theoretical knowledge as far as analysing the pressure transmitted to the target and great care should be taken for any future tests to measure the pressure and make sure that the instrumentation works properly. It is possible that the use of carbon gages is not indicated for this type of application after all. An article is being prepared so that the recent experimental data can be available to the public in the future to complete the already available data.

The depth of understanding gained for bird impact simulation so far gives confidence that the ALE and SPH numerical models can be used on complex structures made of orthotropic

materials such as composites. Future work for the bird calibration would involve more tests where the pressure would be measured properly so that the amount of energy transferred form the projectile to the target is known and can be compared with the numerical simulation.

As for the SPH formulation, a new formulation was developed form the energy conservation equations. The equations obtained are similar to the standard SPH to which a symmetrization has been applied, but it makes room for a variable smoothing length to be thoroughly used and for the use of a boundary correction function. As it turned out, the normalization scheme, which is a kernel and kernel derivative correction, worked better than the boundary correction scheme for the examples developed, which is a type of normalization but applied only to the boundary particles.

Material models were added to the SPH algorithm, and the algorithm was robust enough to treat the example studied without instabilities and within 10 % of the experimental data for the Taylor impact with the iron material. The normalization scheme yielded better results. Part of the explanation resides in the fact that the boundary correction has a value of 0.97 when a particle is at a distance h from the boundary, which is also the minimal distance allowed by the external force. This means that in general, the particles do not get close enough to the boundary for the boundary correction function to have a significant influence. In order to see the full effect of the boundary correction, the particles would need to be much closer to the boundary, which is in opposition with the boundary interaction schemes whose purpose is to prevent penetration.

The error with respect to the experimental results for the Taylor impact was further decreased to 6.4% by using the node to node contact. In a solid-solid impact modelled with SPH, the node to node contact proved to yield better and more realistic results than the external force or contact potential options. Friction was also added to the node to node contact. Although several research works have been made toward a better understanding of contact problems, contact mechanics is however still a complex feature of numerical simulations and being able to model it properly with SPH is an important step of increasing the use of SPH. The Taylor impact example was also solved using copper instead of ARMCO iron and yielded an error of 5.5% which is even better and proved that the

algorithm is versatile. And although there are no experimental results available, the Taylor example was solved one last time using ARMCO iron with the target made deformable and of the same material and was used to show that the node to node contact also worked in that situation.

Finally, SPH was applied to the bird strike problem and gave satisfying results, demonstrating that the algorithm can be used for a variety of material models.

The next step of SPH is to demonstrate what the developed in-house algorithm is capable of with respect to existing commercial software and to implement such feature in such software so as to update their SPH feature. The purpose is to make it possible to couple SPH projectile with complex finite element structures such as aircrafts.

References

1 James S. Wilbeck, *Impact Behavior of Low Strength Projectiles*, Air Force Materials Laboratory, Technical Report AFML-TR-77-134, 1977

2 Sandra E. Wright, Richard A. Dolbeer, *Percentage of Wildlife Strikes Reported and Species Identified under a Voluntary Report System*, 7th combined meeting of Bird Strike Committee USA and Bird Strike Committee Canada, Vancouver, Canada, August 15-18 2005

3 Policy Statement Number ANE-2001-35.13-R0, *Policy for Bird Strike*, Federal Aviation Administration, U.S. Department of Transportation, April 2002

4 M.A. McCarthy, J.R. Xiao, C.T. McCarthy, A. Kamoulakos, J. Ramos, J.P. Gallard, V. Melito, *Modeling of Bird Strike on an Aircraft Wing Leading Edge Made from Fibre Metal Laminates – Part 2: Modeling of Impact with SPH Bird Model*, Applied Composite Materials, **11**, 2004, 317-340

5 L. Iannucci, *Bird-strike impact modeling*, Seminar Foreign Object Impact and Energy Absorbing Structure, London, England, 1998

6 E. Niering, *Simulation of Bird Strikes on Turbine Engines*, Journal of engineering for gas Turbine and Power, **112**, 1990, 572-578

7 B. Langrand, A.-S. Bayart, Y. Chaveau, E. Deletombe, *Assessment of Multi-Physics FE Methods for Bird Strike Modeling – Application to a Metallic Riveted Airframe*, International Journal of Crashworthiness, 7, 2002, 415-428

8 Alan Dobyns, *Bird Strike Analysis of S-92 Vertical Tail Cover Using DYTRAN*, AHS Afordable Composite Structures Conference, Bridgeport, CT, October 7-8 1998

9 Alan Dobyns, Frank Frederici, Rober Young, *Bird Strike Analysis and Test of a Spinning S-92 Tail Rotor*, American Helicopter Society 57th Annual Forum, Washington, DC, May 9-11 2001

10 A. Airoldi, B. Cacchione, *Modeling of Impact Forces and Pressures in Lagrangian Bird Strike Analyses*, International Journal of Impact Engineering, **32**, 2006, 1651-1677

11 Erkan Kirtil, Dieter Pestal, Alexander Kollofrath, Nils Gänsicke, Josef Mendler, *Simulating the Impact Behaviour of Composite Aircraft Structures*, ABAQUS Users' Conference, Austria 2003

12 Frederick Stoll, Robert A. Brockman, *Finite Element Simulation of High-Speed Soft-Body Impacts*, American Institute of Aeronautics and Astronautics, 1997, 334-344

13 A.G. Hanssen, Y. Girard, L. Olovsson, T. Berstad, M. Langseth, *A numerical model for bird strike of aluminium foam-based sandwich panels*, International Journal of Impact Engineering, **32**, 2006, 1127-1144

14 Stuart Kari, Jon Gabrys, David Lincks, *Birdstrike Analysis of Radome and Wing Leading Edge Using LS-DYNA*, 5th International LS-DYNA Users Conference, Southfield, MI, September 21-22 1998

15 S. C. McCallum, C. Constantinou, *The influence of bird-shape in bird-strike analysis*, 5th European LS-DYNA Users Conference, May 2005

16 TH. Kermanidis, G. Labeas, M. Sunaric, L. Ubels, *Development and Validation of a Novel Bird Strike Resistant Composite Leading Edge Structure*, Applied Composite Materials, **12**, 2005, 327-353

17 Alastair F. Johnson, Martin Holzapfel, *Modeling Soft Body Impact on Composite Structures*, Composite Structures, **61**, 2003, 103-113

18 N. F. Martin Jr., *Nonlinear Finite-Element Analysis to Predict Fan-Blade Damage Due to Soft-Body Impact*, Journal of Propulsion, **6**, 1990, 445-450

19 D. Chevrolet, S. Audic, J. Bonini, *Bird Impact Analysis on a Bladed Disk*, Reduction of Military Vehicle Acquisition Time and Cost through Advanced Modeling and Virtual Simulation, Paris, France, April 22-25 2002

20 M. A. McCarthy, R. J. Xiao, C. T. McCarthy, A. Kamoulakos, J. Ramos, J. P. Gallard, V. Melito, *Modeling Bird Impacts on an Aircraft Wng- Part 2 Modeling the impact with and SPH bird model*, International Journal of Crashworthiness, **10**, 2005, 51-59

21 Th. Kermanidis, G. Labeas, M. Sunaric, A. F. Johnson, M. Holzapfel, *Bird Strike Simulation on a Novel Composite Leading Edge Design*, International Journal of Crashworthiness, **11**, 2006, 189-201

22 James S. Wilbeck, James L. Rand, *The Development of a Substitute Bird Model*, Journal of Engineering for Power, 81-GT-23, 1981

23 Tim Moffat, *Numerical Calibration of Bird Impact Pressures and Damage Using MSC/DYTRAN*, Project Report, University of Toronto, Graduate Department of Mechanical and Industrial Engineering, 1999, 62 pages

24 Vijay K. Goyal, Carlos A. Huertas, Tomás R. Leutwiler, José R. Borrero, *Robust Bird-Strike Modeling Based on SPH Formulation Using LS-DYNA*, 47th AIAA/ASME/ASCE/AHS/ASC Structures, Structural Dynamics, and Materials Conference, Newport, Rhode Island, May 1-4 2006

25 Marco Anghileri, Giuseppe Sala, *Theoretical Assessment, Numerical Simulation and Comparison with Tests of Birdstrike on Deformable Structures*, ICAS 20th Congress, Naples, Italy, Sept 8-13 1996

26 Joris Degrieck, Patricia Verleysen, Wim De Waele, *Optical Measurement of Target Displacement and Velocity in Bird Strike Simulation Experiments*, Measurement Science and Technology, **14**, 2003, 1-6

27 M. Hörmann, U. Stelzmann, M.A. McCarthy, J.R. Xiao, *Horizontal Tailplane Subjected to Impact Loading*, 8th International LS-DYNA Users Conference, Dearborn, Michigan, May 2-4 2004

28 Ashish K. Sareen, Michael R. Smith, B. Robert Mullins, *Applications of a Nonlinear Dynamics Tool to Rotorcraft Design Problems at Bell Helicopter Textron Inc.*, 27th European Rotorcraft Conference, Moscow, Russia, September 11-14 2001

29 Luigi-M. L. Castelletti, Marco Anghileri, *Multiple Birdstrike Analysis – A survey of feasible techniques*, 30th European Rotorcraft Forum, Marseilles, Frances, September 14-16 2003

30 Richard Budgey, *The Development of a Substitute Artificial Bird by the International Birdstrike Research Group for use in Aircraft Component Testing*, International Bird Strike Committee, Amsterdam, April 17-21 2000

31 C. H. Edge, *Derivation of a Dummy Bird for Analysis and Test of Airframe Structures*, Bird Strike Committee USA and Bird Strike Committee Canada, Richmond, British Columbia, May 9-13, 1999

32 J.O. Hallquist, *LS-DYNA Theorical Manual*, Version 970, Livermore Software Technology Corporation, Livermore, 2001, 498 pages

33 *ABAQUS User's Manual*, Version 6.3, Hibbit, Karlson and Sorenson, Inc. 1999-2002

34 M. Souli, J. Wang, I. Do, C. Hao, *ALE and Fluid Structure Interaction in LS-DYNA*, 8th International LS-DYNA Users Conference, Dearborn, Michigan, May 2-4 2004

35 J.J. Monaghan, *Smoothed Particle Hydrodynamics*, Annual Review of Astronomic and Astrophysics, **30**, 1992, 543-574

36 V. Centonze, N. M. Schmoeker, *Bird Impact Testing at AEDC's Range S-3*, AIAA/ AHS/ CASI/ DGLR/ IES/ ISA/ ITEA/ SETP/ SFTE, 3rd Flight Testing Conference, Las Vegas, Nevada, April 2-4, 1986

37 M-A Lavoie, A. Gakwaya , M. Nejad Ensan and D.G. Zimcik, *Validation of Available Approaches for Numerical Bird Strike Modeling Tools*, International Review of Mechanical Engineering, 2007, *accepted for publication*

38 Jacques Charest, Ph.D.
Dynasen Inc.
20 Arnold Pl. Goleta, CA. U.S.A. 93117
Phone: (805) 964-4410, Fax: (805) 967-2824

39 M. Souli, A. Ouahsine, L. Lewin, *ALE and fluid–structure interaction problems*, Computer Methods Applied Mechanics Engineering, **190**, 2000, 659–675.

40 L. B. Lucy, *A Numerical Approach to the Testing of the Fission Hypothesis*, The Astronomical Journal, **82**, 1977, 1013-1024

41 J. J. Monaghan & R. A. Gingold, *Shock Simulation by the Particle Method SPH*, Journal of Computational Physics, **52**, 1983, 374-389

42 G. R. Liu & M. B. Liu, Smoothed Particle Hydrodynamics – a meshfree particle method, World Scientific, New Jersey, 2003, 449 pages

43 Chad E. Sparks, Ronald L. Hinrichsen, David Friedmann, Co*mparison and validation of smooth particle hydrodynamic (SPH) and coupled Euler Lagrange (CEL) techniques for modeling hydrodynamic ram*, 13th AIAA/ASME/AHS Adaptive Structures Conference, April 18-21, 2005, Austin, Texas

44 Liang Xue, *Breaking dam flood using smooth particle hydrodynamics method*, 10th International Symposium on Interaction of the Effects of Munitions with Structures, May 7-11, 2001, San Diego, California

45 M. B. Liu, G. R. Liu, K. Y. Lam, Z. Zong, *Smoothed particle hydrodynamics for numerical simulation of underwater explosion*, Computational Mechanics, **30**, 2003, 106-118

46 J. Bonet & S. Kulasegaram, *Correction and stabilization of smooth particle hydrodynamics methods with applications in metal forming simulations*, International Journal for Numerical Methods in Engineering, **47**,2000, 1189-1214

47 James Campbell, Rade Vignjevic, Séverine Lepage, *Numerical simulation of high velocity impacts on thin metallic targets II*, Dynamics & Control of Systems & Structures in Space (DCSSS), 6th Conference, July 2004, Riomaggiore, Italy

48 Rade Vignjevic, James Campbell, Séverine Lepage, *Numerical simulation of high velocity impacts on thin metallic targets I*, Dynamics & Control of Systems & Structures in Space (DCSSS), 6th Conference, July 2004, Riomaggiore, Italy

49 T. Rabczud & J. Eibl, *Simulation of high velocity concrete fragmentation using SPH/MLSPH*, International Journal for Numerical Methods in Engineering, **56**, 2003, 1421-1444

50 M. X. Rodriguez-Paz, J. Bonet, *A corrected smooth particle hydrodynamics method for the simulations of debris flows*, Numerical Method for Partial Differential Equations, **20**, 2004, 140-163

51 Rade Vignjevic, *Review of development of the smooth particle hydrodynamics (SPH) method*, Dynamics & Control of Systems & Structures in Space (DCSSS), 6th Conference, July 2004, Riomaggiore, Italy

52 Shaofan Li, Wing Kam Liu, *Meshfree particle methods and their applications*, Applied Mechanics Review, **55**, 2002, 1-34

53 Joseph Peter Morris, *A study of the stability properties of smooth particle hydrodynamics*, Published for the Astronomical Society of Australia, **13**, 1996, 97-102

54 J. J. Monaghan, *Smoothed Particle Hydrodynamics*, Institute of Physics Publishing, **68**, 2005, 1703-1759

55 T. Rabczuk, T. Belytschko, S. P. Xiao, *Stable particle methods based on Lagrangian kernels*, Computer Methods in Applied Mechanics and Engineering, **193**, 2004, 1035-1063

56 Ted Belytschko, Yong Guo, Wing Kam Liu & Shao Ping Xiao, *A unified stability analysis of meshless particle methods*, International Journal for Numerical Methods in Engineering, **48**, 2000, 1359-1400

57 H. Huang, C. T. Dyka, S. Saigal, *Hybrid particle methods in frictionless impact-contact problems*, International Journal for Numerical Methods in Engineering, **61**, 2004, 2250-2272

58 R. Vignjevic, J. Campbell, L. Libersky, *A treatment of zero-energy modes in the smoothed particle hydrodynamics method*, Computer Methods in Applied Mechanics and Engineering, **184**, 2000, 67-85

59 L. Cueto-Felgueroso, I. Colominas, G. Mosqueira, F. Navarrina & M. Castelreiro, *On the Galerkin formulation of the smoothed particle hydrodynamics method*, International Journal for Numerical Methods in Engineering, **60**, 2004, 1475-1512

60 J. Bonet, Miguel X. Rogríguez-Paz, *Hamiltonian formulation of the variable-h SPH equations*, Journal of Computational Physics, **209**, 2005, 541-558

61 W. K. Liu, J. Adee, S. Jun, *Reproducing kernel and wavelets particle methods for elastic and plastic problems*, Advanced Computational Methods for Material Modeling, **180**, 1993, 175-190

62 G. A. Dilts, *Moving least-square particle hydrodynamics I: Consistency and stability*, International Journal of Numerical Methods in Engineering, **44**, 1999, 1115-1155

63 G. A. Dilts, *Moving least-square particle hydrodynamics II: Conservation and boundaries*, International Journal of Numerical Methods in Engineering, **48**, 2000, 1503-1524

64 Lynyrd de Wit, Smoothed Particle Hydrodynamics – A study of the possibilities of SPH in hydraulic engineering, Delft University of Technology, The Netherlands, 2006, 96 pages

65 G. R. Johnson, S. R. Beissel, *Normalized smoothing functions for SPH impact computations*, International Journal for Numerical Methods in Engineering, **39**, 1996, 2725-2741

66 Y. Krongauz, T. Belytschko, *Consistent pseudo-derivatives in meshless methods*, Computer Methods in Applied Mechanics and Engineering, **146**, 1997, 371-386

67 J. K. Chen, J. E. Beraun, C. J. Jih, *An improvement for tensile instability in smoothed particle hydrodynamics*, Computational Mechanics, **23**, 1999, 279-287

68 J. K. Chen, J. E. Beraun, C. J. Jih, *A corrected smoothed particle method for transient elastoplastic dnamics*, Computational Mechanics, **27**, 2001, 177-187

69 J. K. Chen, J. E. Beraun, C. J. Jih, *Completeness of corrective smoothed particle method for linear elastodynamics*, Computational Mechanics, **24**, 1999, 273-285

70 J. Bonet, S. Kulasegaram, M. X. Rodriguez-Paz, M. Profit, *Variational Formulation for the Smooth PArticle Hydrodynamics (SPH) Simulation of Fluid and Solid Problems*, Computer Methods in Applied Mechanics and Engineering, **193**, 2004, 1245-1256

71 M. B. Liu, G. R. Liu, K. Y. Lam, *Constructing smoothing functions in smoothed particle hydrodynamics with applications*, Journal of Computational and Applied Mathematics, **155**, 2003, 263-284

72 J. J. Monaghan, *Smoothed Particle Hydrodynamics*, Annual Review of Astronomic and Astrophysics, **30**, 1992, 543-574

73 J. J. Monaghan, *SPH without a tensile instability*, Journal of Computational Physics, **159**, 2000, 293-311

74 T. Belytschko, Y. Krongauz, J. Dolbow & C. Gerlach, *On the completeness of meshfree particle methods*, International Journal for Numerical Methods in Engineering, **43**, 1998, 785-819

75 P. W. Randles & L. D. Libersky, *Normalized SPH with stress points*, International Journal for Numerical Methods in Engineering, **48**, 2000, 1445-1462

76 M. B. Liu, G. R. Liu, *Restoring particle consistency in smoothed particle hydrodynamics*, Applied Numerical Mathematics, **56**, 2006, 19-36

77 Libor Lobovský, Application of SPH in Fluid Mechanics, University of West Bohemia in Pilsen, 2003, 80 pages
78 Matthias Müller, Simon Schirm, Matthias Teschner, Bruno Heidelberger, Markus Gross, *Interaction of fluids with deformable solids*, Computer Animation and Virtual Worlds, **15**, 2004, 159-171
79 S. Kulasegaram, J. Bonet, R. W. Lewis, M. Profit, *A Variational formulation based contact algorithm for rigid boundaries in two-dimensional SPH applications*, Computational Mechanics, **33**, 2004, 316-325
80 T. De Vuyst, R. Vignjevic, J. C. Campbell, *Coupling between meshless and finite element methods*, International Journal of Impact Engineering, **31**, 2005, 1054-1064
81 J. Campbell, R. Vignjevic, L. and Libersky, *A contact algorithm for smoothed particle hydrodynamics*, Computer Methods in Applied Mechanics and Engineering, **184**, 200, 49-65
82 Larry D. Libersky, Albert G. Petschek, Theodore C. Carney, Jim R. Hipp, Firooz A. Allahdadi, *High Strain Lagrangian Hydrodynamics – A Three-Dimensional SPH Code for Dynamic Material Response*, Journal of Computational Physics, **109**, 1993, 67-75
83 Songwon Seo, Oakkey Min, *Axisymmetric SPH simulation of elasto-plastic contact in the low velocity impact*, Computer Physics Communications, **175**, 2006, 583-603
84 O. Botella & R. Peyret, *Benchmark Spectral Results on the Lid-Driven Cavity Flow*, Computers & Fluids, **24**, 1998, 421-433
85 J. C. Martin & W. J. Moyce, *Part IV. An experimental study of the collapse of liquid columns on a rigid horizontal plane*, Phylosophical Transactions. Series A, **244**, 1952, 312-324
86 J. Bonet, T.-S.L. Lok, *Variational and momentum preservation aspects of Smooth Particle Hydrodynamic formulations*, Computer Methods in Applied Mechanics and Engineering, **180**, 1999, 97-115
87 J. J. Monaghan, *Simulating Free surface Flows with SPH*, Journal of Compuational Physics, **110**, 1994, 399-406
88 J. Dolbow and T. Belytschko, *An Introduction to Programming the Meshless Element Free Galerkin Method*, Archives of Computational Methods in Engineering, **5**, 1998, 207-241
89 Gary A. Dilts, *Moving least-squares particles hydrodynamics II: conservation and boundaries*, International Journal for Numerical Methods in Engineering, **48**, 2000, 1503-1524
90 F. P. Fahrenthold, J. C. Koo, *Hamiltonian particle hydrodynamics*, Computer Methods in Applied Mechanics and Engineering, **146**, 1997, 43-52
91 G. R. Liu, Y. T. Gu, *Boundary meshfree methods based on the boundary point interpolation methods*, Engineering Analysis with Boundary Elements, **28**, 2004, 475-487
92 Gordon R. Johnson, Tim. J. Holmquist, *Evaluation of cylinder-impact test data for constitutive model constants*, Journal of Applied Physics, **54**, 1988, 3901-3910
93 T. De Vuyst, R. Vignjevic, J.C. Campbell, *Coupling between meshless and finite element methods*, International journal of Impact Engineering, **31**, 2005, 1054-1064
94 Songwon Seo, Oakkey Min, *Axisymmetric SPH simulation of elasto-plastic contact in the low velocity impact*, Computer Physics Communication, **175**, 2006, 583-603
95 Guangyao Li, Ted Belytschko, *Element-free Galerkin method for contact problems in metal forming analysis*, Engineering Computations, **18,** 2001, 62-78
96 Erik Oberg, Farnklin D. Jones, Holbrook L. Horton, Henry H. Ryffell, 26th Machinery's Handbook, Industrial Press Inc., New York, 2000, 2630 pages